GRAVITY-FORCE RESISTING SYSTEM FLEXURAL STIFFNESS MODIFIERS FOR SEISMIC ANALYSIS OF TALL REINFORCED CONCRETE SHEAR WALL BUILDINGS

by

Camilo Sebastian Granda Valencia

B.Sc., Universidad San Francisco de Quito, 2018

A THESIS SUBMITTED IN PARTIAL FULFILLMENT OF

THE REQUIREMENTS FOR THE DEGREE OF

MASTER OF APPLIED SCIENCE

in

THE FACULTY OF GRADUATE AND POSTDOCTORAL STUDIES

(Civil Engineering)

THE UNIVERSITY OF BRITISH COLUMBIA

(Vancouver)

March 2022

The following individuals certify that they have read, and recommend to the Faculty of Graduate and Postdoctoral Studies for acceptance, a thesis entitled:

Gravity-force resisting system flexural stiffness modifiers for seismic analysis of tall reinforced concrete shear wall buildings

submitted by	Camilo Sebastian Granda Valencia in partial fulfillment of the requirements for
the degree of	Master of Applied Science
in	Civil Engineering

Examining Committee:

Carlos Molina Hutt, PhD, Dept. of Civil Engineering, The University of British Columbia
Supervisor

Jose Centeno, PhD, PEng, Glotman Simpson Consulting Engineers
Additional Examiner

Abstract

High-rise residential buildings are considered as one of the best solutions to the current lack of space in urban areas. In high-density cities in the Canadian Pacific Northwest, reinforced concrete shear wall structures are one of the main typologies used in tall buildings design. This type of building is composed of a seismic-force resisting system and a gravity-force resisting system. While the former system is designed to resist lateral loads, failure of the gravity-force system is recognized as one of the main causes of building collapse under earthquake demands. Accurate estimation of seismic demands in this system is critical to provide a safe design. The goal of this study is to obtain gravity system flexural stiffness modifiers to safely estimate their seismic demands following a linear-elastic analysis. The proposed flexural stiffness modifiers were derived from the moment-curvature analysis of members within a nonlinear 3D reinforced concrete shear wall structural analysis building model (with both seismic-force and gravity-force resisting systems modelled as nonlinear). These quantitative results for individual members are used to perform regression analyses to develop generalized equations to estimate the flexural stiffness modifiers in gravity-frame columns and slabs. Typical flexural stiffness modifiers range from 3-100% and 18-85%, for columns and slabs, respectively. In most of the cases, the results show that the gravity system bending moment demands of a linear-elastic analysis model with the proposed effective stiffness modifiers are consistent with the moment demands in an equivalent nonlinear model. The proposed recommendations provide appropriate estimates of seismic demands in the gravity-force system by means of realistic stiffness factors. Moreover, they support the implementation of the Simplified Analysis procedure for the gravity-system design of reinforced concrete shear wall buildings as outlined in the Canadian concrete standard (CSA A23.3-19 § 21.11.2.1) by practicing engineers.

Lay Summary

This thesis provides recommendations and tools for practicing structural engineers on how to estimate the effective stiffness of reinforced concrete columns and slabs that are not part of the seismic-force resisting system in modern tall residential reinforced concrete shear wall buildings. With this information, structural engineers can accurately estimate the seismic demands in these elements by means of a simplified linear-elastic analysis procedure. Past earthquakes have shown that failure of slabs and columns that are part of a building's gravity system can lead to building collapse. For this reason, accurate and realistic estimates of the earthquake forces induced in these elements is needed.

Preface

Camilo Granda Valencia was the responsible for the literature review, methodology, gravity-system modelling, computational analyses, validation, post-processing of data, results interpretation, statistical analysis, and development of proposed equations.

Alireza Eksir Monfared modelled and designed the seismic-force resisting system. Dr. Jose Centeno designed the gravity-force resisting system. Dr. Carlos Molina Hutt and Dr. Jose Centeno were involved in the conceptualization of the project and supervision. The author revised this based on the comments of Dr. Carlos Molina Hutt and Dr. Jose Centeno.

Table of Contents

List of Tables

List of Figures

List of Symbols

a/d = shear span-to-depth ratio.

A_g = cross-sectional gross area.

$A_{s,\min}$ = minimum area of longitudinal reinforcement required for bending moment demands.

A_{st} = area of longitudinal reinforcement required for bending moment demands.

b = column depth.

b_{eff} = effective width of slab that provides framing flexural action.

b_t = cross-section width under tension.

c_1 = depth of the column or wall framing into the slab.

d = depth of structural element.

d_B = longitudinal rebar diameter.

d_1 = distance from the mid-depth fibre to fibre one.

d_2 = distance from the mid-depth fibre to fibre two.

D = dead load.

EI_{eff} = effective flexural stiffness.

EI^{i}_{eff} = effective flexural stiffness at the current calibration step.

EI^{i-1}_{eff} = effective flexural stiffness at the previous calibration step.

EI_g = gross flexural stiffness.

E_{col} = concrete elasticity modulus for column elements.

E_{slab} = concrete elasticity modulus for slab elements.

E_c = concrete elasticity modulus.

E_s = steel rebar elasticity modulus.

f'_c = nominal concrete compressive strength.

f'_{cc} = confined concrete compressive strength.

f'_{ce} = expected concrete compressive strength.

f'_{cr} = rupture modulus.

f'_t = tensile concrete strength.

f_{ue} = expected ultimate steel rebar strength.

f_y = nominal yield strength for steel rebar.

f_{ye} = expected yield strength for steel rebar.

F_{GFRS} = final seismic demands in the GFRS following Beauchamp et al. (2017) method.

F_{GNS} = seismic demands in the GFRS with null stiffness (Beauchamp et al., 2017).

F_{sr} = factor equal to 10^{-2} to 10^{-3} to reduce the effective stiffness in the gravity-frame (Beauchamp et al., 2017).

h = storey height.

h_w = height of tower building above grade.

I_{col} = second moment of inertia for columns.

I_{slab} = second moment of inertia for slabs.

I_E = importance factor.

l = slab span.

l_1 = effective width slab span.

L = live load.

M_{cr} = cracking moment.

M_D = $M_n/f'_{ce}d^3$ = dimensionless moment

M_f = factored applied bending moment.

M_{LE} = bending moment demand in the linear-elastic model.

$M^{i-1}{}_{LE}$ = bending moment demand at the previous calibration step in the linear-elastic model.

M_n = nominal bending moment capacity accounting for gravity load.

M_{NL} = bending moment demand in the nonlinear model.

M_r = factored bending moment capacity.

M'_y = moment at first yield.

P = factored gravity load.

$P_{r,\max}$ = capped compressive resistance.

P_{ro} = compressive resistance.

s = tie spacing.

S_a = spectral acceleration.

R_d = seismic force modification factor accounting for ductility.

R_o = seismic forces modification factor accounting for overstrength.

R^2 = coefficient of determination.

t = slab thickness.

t_i = chronological time in nonlinear stage analysis.

u_i = lateral displacement in the GFRS elements after applying the Simplified Drift Profile; for columns it is the mid-height storey lateral displacement.

$u_{i,\max}$ = lateral displacement atop of the roof after applying the Simplified Analysis drift profile.

y = distance from the neutral axis to a specific cross-section fibre.

V_d = base design shear.

V_e = base elastic shear force.

α_1 = ratio of average stress in the rectangular compression block to the specified concrete strength.

δ_i = interstorey drift ratio.

ε = strain at a specific fibre.

ε_c = unconfined concrete strain at maximum strength.

ε_{cc} = confined concrete strain at maximum strength.

ε_{cr} = cracking concrete strain.

ε_{cu} = crushing concrete strain.

ε_{rup} = rupture tensile strain for steel rebar.

ε_{sh} = strain hardening for steel rebar.

ε_{sp} = spalling strain for concrete under compression.

ε_{ut} = ultimate strain for concrete under tension.

ε_y = yield strain for steel rebars.

ε_1 = strain at fibre one.

ε_2 = strain at fibre two.

λ = parameter that estimates the deformation mode in a wall-frame building system

ρ_l = ρ = longitudinal reinforcement ratio.

ϕ_c = material factor for concrete equal to 0.65.

ϕ_l = diameter of longitudinal steel rebar.

ϕ_s = material factor for steel rebar equal to 0.85.

ϕ_t = diameter of transverse reinforcement.

Δ = design displacement at roof top in a tower building.

Δ_y = displacement at roof top causing yield in the building system.

Δ_C = Unknown distance to solve for y in the compression case.

Δ_T = Unknown distance to solve for y in the tension case.

$\Delta_f R_d R_o$ = NBC 2015 design displacement obtained through a linear-dynamic analysis.

List of Abbreviations

1D: one dimension

2D: two dimensions

3D: three dimensions

ALR: axial load ratio

CSA: Canadian Standards Association

EBW: effective beam width

GFRS: gravity-force resisting system

LATBSDC: Los Angeles Tall Buildings Structural Design Council

LE: linear-elastic

NE: northeast

NL: nonlinear

NW: northwest

PNW: pacific northwest

RC: reinforced concrete

RCSW: reinforced concrete shear wall

RMSE: root mean squared error

SE: southeast

SFRS: seismic-force resisting system

SW: southwest

Glossary

Wallumn: a column designed to resist gravity force with a cross-section depth at least two times larger than its width. The strong axis moment of inertia can attract significant seismic demands that are not generally accounted for in design.

Acknowledgements

I would like to express my deepest appreciation to my research supervisor, Dr. Carlos Molina Hutt. After our first meeting more than two years ago, I left his office with two thoughts: 1) I will be working with an amazing researcher and 2) I do not understand half of my MASc. project. Now that I am leaving UBC those thoughts have evolved and I am left with two larger sentiments. First, I am happy to have met this wonderful researcher, but also and most importantly I am grateful I got the chance to work with an amazing human being. Secondly, I feel accomplished that what I once believed was impossible, turned into this finalized project thanks to his continuous guidance, support, and encouragement. I am sure that with his charisma and work ethic this young professor will make many positive contributions to our field.

In that same meeting I had the pleasure to meet Dr. Jose Centeno from Glotman Simpson Consulting Engineers. His input, comments, and challenging questions were greatly appreciated and improved the quality of my work. Most importantly, I am profoundly grateful for his kind words and positive attitude during times when I felt I had hit a dead-end. He believed in me and in this project when I was not believing in myself. I really appreciate the mentorship and advice given during crucial points of my project.

Additionally, I am grateful for my former supervisor, Dr. Eva Lantsoght from TU Delft/Universidad San Francisco de Quito. Her guidance and motivation were fundamental to be in the direction I am right now.

During the first year of my graduate studies, my project was funded by the generous financial support of Mr. Stephen W. Fan in representation of the Wendy Fan Memorial Scholarship. This support is greatly appreciated and recognised.

I would also like to thank my lab mates Pouria, Gerald, and Jenny for their help during this time. A special mention goes to my lab mate Preetish Kakoty, who I also have the honour to call my friend. His good-hearted personality and unique charm were critical in supporting myself overcoming adversity.

My family and friends deserve a special recognition for being the backbone in my life. I feel grateful to be surrounded by people who love and support me. Special thanks to my parents, Luz and Medardo; my grandmother, Luz Mary; and my girlfriend, Valerie.

I would like to acknowledge that this research project was carried out on the traditional, ancestral, and unceded territory of the Musqueam people.

To my parents and grandmother.

Chapter 1: Introduction

1.1 Background, Aim, and Objectives

Southwest British Columbia is Canada's most seismically active region. This area is exposed to a variety of seismic sources that can produce subduction, intraslab, and crustal earthquakes. Furthermore, this region holds one of the largest concentrations of population in Canada. Around 2.5 million people live in Metro Vancouver and it is expected that by 2050 this number will increase to 3.6 million (Metro Vancouver, 2018). This population rise calls for more household units. According to Metro Vancouver (2018), apartments will make 62% of the housing development in the next 30 years. Tall tower apartment buildings are a great solution to the scarcity of land in cities with a high-density population. In seismically active regions, reinforced concrete shear walls (RCSW) are the preferred seismic-force resisting system (SFRS) for tall tower buildings. The large stiffness of this system is effective in controlling the large drifts imposed by lateral seismic loads. The earthquake energy dissipation is allocated at the base of the core walls and by hinging of the coupling beams.

In addition to the SFRS, tall buildings have an additional structural system called gravity-force resisting system (GFRS). In contrast to the SFRS, this system is not designed to withstand earthquake forces. The GFRS is generally a frame structure composed by a combination of columns, slabs, and beams. These structural elements are intended to transfer the gravity forces, e.g., self-weight, superimposed dead load, live load, etc., to the foundation. Although they are detailed for gravity forces only, these elements will engage and take lateral seismic load if: 1) The frame system is stiff (in relation to the SFRS), or 2) the SFRS has yielded and therefore softened.

Moreover, the GFRS will need to accommodate the lateral displacement demands of the SFRS to achieve compatibility. These displacement demands could be significant because the SFRS is designed to be ductile and go into the nonlinear range. Observations from past earthquake events in Northridge, CA (1994) and Christchurch, New Zealand (2011) (Mitchell, et al., 1995; Elwood, 2013) demonstrate that one of the main reasons for building collapse is triggered by failure of elements not part of the SFRS. Some examples are the Pyne Gould Corporation building, Canterbury Television building, and the California State University parking. To address this problem, North American building codes for concrete design, CSA A23.3-19 (CSA, 2019) and ACI 318-19 (ACI, 2019), have developed prescriptive design clauses for structural engineers to evaluate the seismic demands in elements of the GFRS. The codes' objective is to check if the GFRS gravity design is able to withstand the seismic displacement demands. If this is not fulfilled, appropriate seismic detailing is required to withstand earthquake actions.

In Canada RCSW buildings are designed following the CSA A23.3-19 (CSA, 2019) and NBC 2015 (NRC, 2015) requirements. These codes allow practicing engineers to follow a linear-elastic prescriptive approach for the SFRS and GFRS design of tall buildings. There are two prescribed procedures, the General Analysis and Simplified Analysis, to estimate the GFRS seismic demands. Both methods are described in Sections § 21.11.2.1 and § 21.11.2.2 of the CSA A23.3-19 standard, respectively. These procedures provide the practicing engineers a method to assess the seismic demands experienced by the GFRS after it has been designed for gravity forces only. Within these procedures, the engineer is required to evaluate the structure and subject it to the design displacement accounting for foundation movements, nonlinearity in the RCSW plastic hinge zone, and cracking of concrete in elements belonging to the GFRS. CSA A23.3-19 specifies that the effective stiffness, should be an upper-bound value to safely estimate the demands (in this document, the effective stiffness represents the effective flexural stiffness). Larger values of effective stiffness attract more seismic loading resulting in a conservative estimation of seismic loads. It is common practice in structural design offices to assume a small value for the out-of-plane flexural effective stiffness (i.e., EI_{eff}) of slabs, usually 10-25% of their gross stiffness and $EI_{eff} = 0.70EI_g$ for columns (J. Centeno, personal communication, November 11, 2021). This has been adopted because the upper-bound stiffness modifiers are not explicitly defined in CSA A23.3-19. Failure of columns could cause loss stability and trigger collapse. For this reason, the intention of this assumption is to allocate high demands in critical elements through high estimates of effective stiffness. These assumptions result in gravity columns that resemble those in moment resisting frames, which are capable of dissipating seismic demands through nonlinear deformation without loss of gravity load bearing capacity. By contrast, elements like slabs and beams have smaller arbitrary values because they are expected to release energy through cracking and yielding.

This thesis aims to assess the flexural stiffness factors of the gravity-force system in RCSW shear wall buildings. The first objective is to obtain good agreement in the seismic demands between a full nonlinear RCSW 3D building model and a linear-elastic virtual twin building model with effective stiffness factors under same levels of displacement. A full nonlinear model was used because it is the best analysis tool to evaluate the performance of buildings. The results of this detailed nonlinear model are compared to a linear-elastic building since the latter is the most common analysis approach used by structural design engineers. Second, recommendations to estimate the GFRS stiffness modifiers according to the most influential design parameters are provided as a tool for practicing engineers to correctly assess and estimate the seismic demands in the GFRS following a linear-elastic prescribed procedure. It is intended that these recommendations will support the implementation of clauses § 21.11.2.1 and § 21.11.2.2 of the CSA A23.3-19.

1.2 Methodology

The main goal of this thesis is to provide realistic flexural stiffness factors in elements that are part of the gravity-force resisting system to support the implementation of clauses § 21.11.2.1 and § 21.11.2.2 of the Canadian concrete standard for practicing engineers. These flexural stiffness modifiers are intended to provide safe estimates of earthquake demands in members not part of the seismic-force system. The methodology adopted in this thesis is described in this section and shown in Figure 1.1.

First, a full nonlinear 3D building model was designed and modelled in LS-Dyna (LSTC, 2020). The building was designed following the prescriptive approach from the Canadian standard for concrete design and the Canadian building code (CSA, 2019; NRC, 2015). The building is representative of a typical Vancouver high-rise residential tower. Nonlinear modelling validation of the SFRS was carried out against laboratory results (Eksir Monfared A. , 2020) to ensure adequate structural performance. The core was modelled using multi-layer shells able to capture shear-flexure interaction and the coupling beams were modelled using a lumped plasticity beam element able to replicate the hysteretic nonlinear behaviour of reinforced concrete coupling beams. The slabs and columns part of the GFRS were modelled using fibre elements which capture the moment-axial force interaction. Consistent with the SFRS, the fibre-based modelling approach of the GFRS was validated against laboratory experimental results.

The next step was to obtain the design displacements from a linear-elastic dynamic analysis following the NBC 2015 (NRC, 2015) clauses. With the design displacement of each direction, the drift profile for the cantilever and coupled direction was developed according to the Simplified Analysis clause §21.11.2.2 from the CSA A23.3-19 code. The 3D nonlinear model was subjected to the design displacement drift profile by means of a pushover analysis in each direction separately. The fibre element formulation of the GFRS elements assumes that cross-sections remain plain. With this, the strain through the height of the element was extracted from the model and the curvature was computed. The effective flexural stiffness of each member was obtained from the moment-curvature plots.

The effective stiffness results inferred from the moment-curvature analyses were adopted in a linear-elastic virtual twin building model because this analysis is the most common approach used in design practice. This 3D linear-elastic building model was also subjected to the same pushover and drift profile described in the Simplified Analysis of CSA A23.3-19. The GFRS bending moment demands from this linear-elastic model were compared against the bending moment demands of the nonlinear model. Effective stiffness calibration was performed by comparing the linear-elastic vs nonlinear bending moment demands. These last two steps were iterated until good agreement between the linear-elastic and nonlinear building model was achieved.

To facilitate the implementation of the Simplified Analysis in structural design practice while leveraging the results of this study, prediction equations and recommendations on the EI_{eff} of slabs and columns are developed based on a single building case study. Through regression analyses, flexural effective stiffness predictor equations for gravity-frame columns and slabs are proposed for gravity systems with different geometric properties. The most influential and statistically significant design parameters were chosen to predict the effective stiffness in these structural members. Residual analysis was carried out to prove the validation of the regression models and recommendations are proposed. Finally, a validation of the equations' prediction power is carried out. For this, two buildings with the same SFRS, but different GFRS will be used in the assessment. The first goal of this exercise is to ensure there is no significant loss of accuracy when using the generalized expressions. The second goal is to check the prediction power of the equations when a different GFRS is used. The linear-elastic buildings adopted the flexural stiffness modifiers obtained through the proposed flexural effective stiffness prediction equations. Both buildings were subjected to the Simplified Analysis drift profile in each direction separately and their linear-elastic GFRS moment demands were benchmarked against the results of their detailed nonlinear virtual twin.

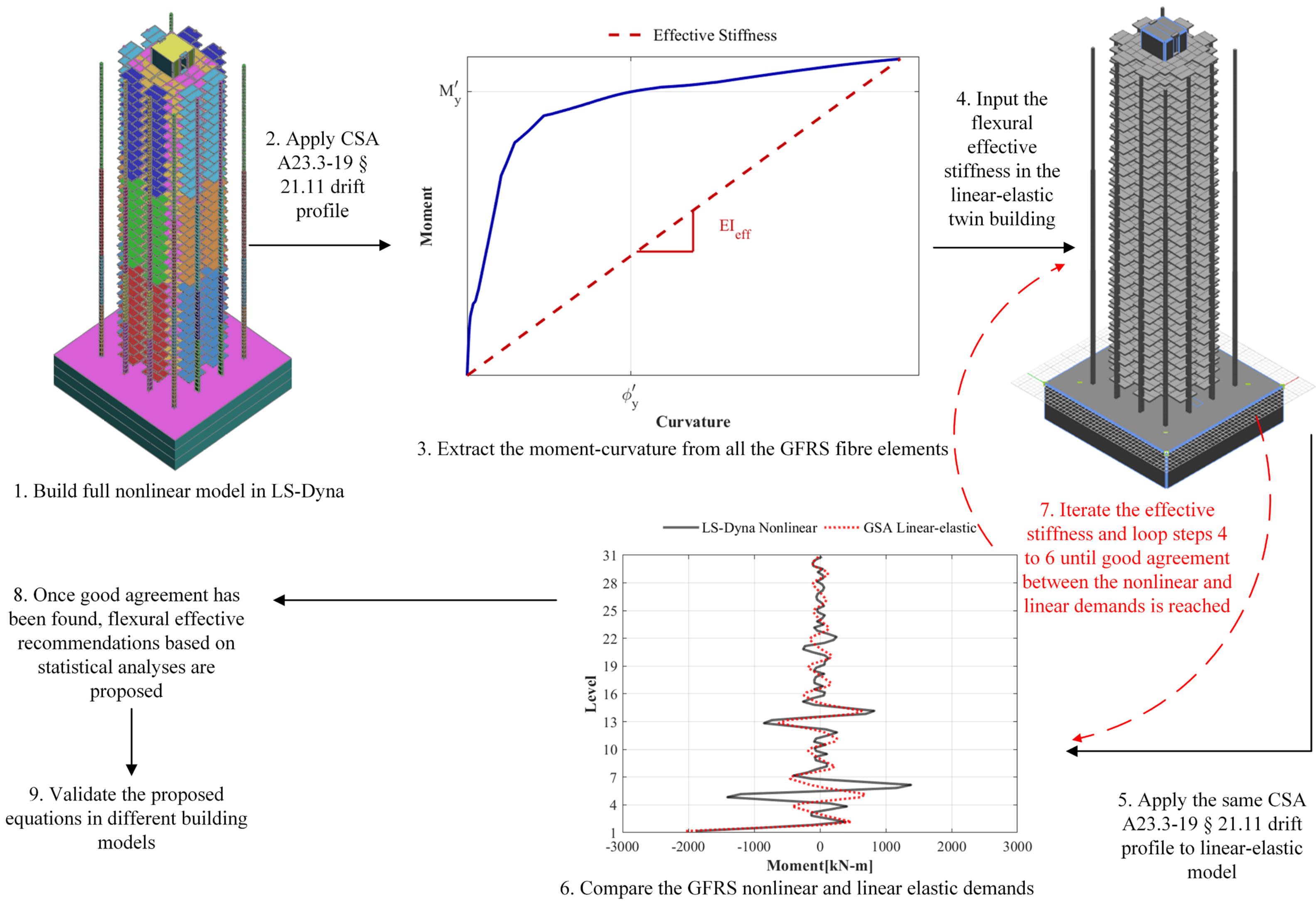

Figure 1.1 Methodology used in this study

1.3 Thesis outline

This thesis proposes flexural effective stiffness modifiers of the GFRS in tall residential RCSW buildings to provide realistic estimates of seismic demands in columns and slabs that are not part of the SFRS. The flexural effective stiffness factors were initially obtained from a single building case study. By performing regression analyses to the flexural stiffness results, proposed equations were developed to generalize the estimation of these modifiers to other gravity-frame members. Additionally, it provides flexural effective stiffness prediction equations for columns and slabs columns that belong to the GFRS to support the implementation of CSA A23.3-19 clause §21.11.2.2 in structural design practice. This thesis consists of the following chapters:

Chapter 1 presents important background information, introduces the research problem, and describes the methodology adopted in this work.

Chapter 2 provides a literature review on 1) the seismic design of RCSW in Canada, 2) case studies of building collapse triggered by failure of the GFRS, 3) the code requirements by CSA A23.3-19 and ACI 318-19 to quantify the seismic demands in the GFRS and a brief comparison between the two standards, 4) a non-prescriptive approach to obtain the seismic demands in the GFRS, 5) the effective width beam (EBW) modelling approach for slabs as an alternative method for lateral analysis, 5) the axial elongation of slabs and beams and its effect on the stiffness of these members, 6) wall-frame interaction, and 7) a discussion on the flexural effective stiffness of reinforced concrete elements and its multiple definitions.

Chapter 3 describes the structural layout of the studied building archetype. Material and geometric properties of the SFRS and GFRS are listed. Additionally, the gravity design of columns and slabs following the CSA A23.3-19 requirements is summarized.

Chapter 4 describes the static pushover analysis for both linear and nonlinear models following the Simplified Analysis procedure. The modelling assumptions of the linear-elastic static (pushover) analysis are presented. Additionally, the feasibility of modelling the slabs as effective width elements is assessed. The next part of this chapter focuses on the nonlinear analysis of the studied building archetype. First, the constitutive material models for reinforced concrete and steel reinforcement are presented. Second, a brief description of the GFRS and SFRS element formulation is summarized. Third, a validation of the fibre-based element formulation used for the elements of the GFRS is performed by calibrating three virtual twin models to experimental results. Last, the induced compressive forces caused by the axial elongation of effective width slabs is discussed.

Chapter 5 establishes and validates the procedure to obtain the moment-curvature plots from the nonlinear building model of Chapter 4. Additionally, the method to compute the flexural effective stiffness of the GFRS components is described. The iteration methodology to calibrate the flexural effective stiffness factors by comparing the linear-elastic against the nonlinear moment demands is discussed. After the iterations showed good agreement, the final flexural effective stiffness values for the GFRS are presented.

Chapter 6 utilizes the flexural effective stiffness data generated in Chapter 5 out of a single building case study to formulate equations for broader use in gravity systems with different geometric properties. These equations predict the flexural effective stiffness modifiers of columns and slabs not part of the SFRS. Several design parameters, geometric, and material variables were assessed to carry out regression analyses. Only statistically significant variables were included in the flexural effective stiffness prediction equations.

Chapter 7 evaluates the prediction power of the equations developed in Chapter 6. For this, the flexural effective stiffness modifiers obtained through the proposed equations are included in two linear-elastic buildings models with different gravity-frame geometric properties but same SFRS. The bending moment demands of each linear-elastic model are benchmarked against its nonlinear twin to analyze the accuracy of the proposed equations. Additionally, the GFRS design compliance is assessed following the § 21.11 CSA A23.3-19 guidelines.

Chapter 8 summarizes the contributions of this thesis, its conclusions and limitations, as well as recommendations to further enhance this research.

Chapter 2: Literature Review

2.1 RCSW High-Rise Design Western Canada

The seismic design of typical high-rise reinforced concrete shear wall buildings follows a prescriptive approach detailed in the National Building Code of Canada (NBC) (National Resources Canada (NRC), 2015). In Southwest BC (British Columbia), the SFRS of high-rise residential buildings is typically composed of cantilevered shear walls, coupled shear walls, or a combination of both. It is assumed that the SFRS will take the bulk of the lateral loads in the structure, i.e. wind and seismic. On the other hand, the gravity-force resisting system (GFRS) will be a combination of columns, bearing walls, slabs, and beams. The GFRS will be designed to take all the vertical loads caused by gravity demands, e.g.: self-weight, superimposed dead load, live load, etc.

Assuming all the seismic load will be resisted by the SFRS yields a conservative design. By developing hinges at the base of the wall and in the coupling beams of the SFRS, the designer intends to protect the GFRS from collapse. The SFRS will yield first as it is the stiffest structural element in the building system, taking the largest portion of seismic demands. Once the seismic demands match the SFRS nominal capacity, concrete cracks and rebar yielding arise at the SFRS bottom walls and coupling beams. At this point, a complete softening of the SFRS occurs resulting in a negligible structural stiffness. Thus, the SFRS will not be able to take more seismic load, however, it can still dissipate seismic energy through inelastic deformations. As the SFRS is not able anymore to accommodate the seismic loads, the GFRS will engage and start accommodating the seismic demands as it is the next stiffer structural system. Consequently, the practicing engineer needs to ensure all the elements of the GFRS have either 1) enough capacity to remain linear elastic under a seismic hazard or 2) enough ductility to accommodate lateral demands (CSA, 2019).

The GFRS is usually composed by columns and flat reinforced concrete slabs. A unique feature of typical gravity columns found in southwest BC is their large, elongated depth in relation to their narrow width. In contrast with square-like shaped cross-sections, these columns have a depth-to-width ratios of at least 2:1, although in many cases the ratio is larger than this. Because of their elongated shape, which resembles that of a wall, they are commonly referred to as "wallumns". As outlined by Adebar et al. (2010), there are a number of reasons to use wallumns as part of the GFRS, including: 1) the long depth reduces the slab span in one direction, resulting in a cost-effective design and less serviceability concerns, 2) the narrow width provides the architect the opportunity to hide this structural element using a partition wall.

2.2 Building Collapse Caused by GFRS Failure

CSA A23.3-19, acknowledges that a "common cause" that leads to the collapse of structures during earthquakes is the failure of the GFRS (CSA, 2019). Observations of different authors (Mitchell, et al., 1995; Hyland, 2012; Elwood, 2013;) concluded that collapse was induced by failure of reinforced concrete elements that are not part of the SFRS due to poor detailing and brittle behaviour.

During the 2011 Christchurch, New Zealand earthquake, the Canterbury Television building collapsed. 62% of all the earthquake fatalities occurred at this location (Ministry for Culture and Heritage, 2021). The six-storey building had a primary lateral system consisting of ductile shear walls at the north and south sides of the building. Columns and beams were not intended to contribute the earthquake resistance (Hyland, 2012). The most certain possible collapse scenario was initiated by failure of an external column when the drift demand exceeded the column's lateral displacement capacity. This put larger gravity loads on the interior columns. Their small cross-section (400mm diameter) and poor transverse reinforcement confinement accelerated the collapse progression. Once the interior columns began to fail, the floor slabs fell down initiating the collapse.

In the same 2011 Christchurch earthquake, the Pyne Gould Corporation building collapsed. The building had an eccentric core wall and a beam-column gravity frame (Elwood, 2013). In this case, the lightly reinforced wall failed first. This failure imposed large deformation demands in the gravity system which caused the joints and columns to snap leading to the loss of gravity load carrying capacity and resulting in the total collapse of the building. In this case, there is a clear necessity to provide seismic detailing to the columns and beams to withstand large nonlinear deformation imposed by the SFRS after a seismic event.

After the 1994 Northridge, California earthquake (Mitchell, et al., 1995) the California State University parking collapsed. The SFRS of this reinforced concrete structure was composed by an exterior ductile moment-frame. The interior columns, which triggered the collapse of the parking, were designed to sustain gravity loads only (Mitchell et al., 1995). The exterior ductile moment frame showed great ability to undergo large deformations and curvatures without the sudden loss of strength. However, the interior columns, which lacked seismic detailing, failed. This example illustrates the need to account for seismic demands when designing members that are not part of the SFRS.

The seismic performance and safety of gravity-loaded columns not part of the SFRS raises concerns about their collapse potential. One problematic aspect of these elements is the unknown amount of earthquake demands they attract, even if the SFRS has not yielded yet. This issue relates with the first building collapse example explained previously in this section. The second problem is related to the seismic detailing of the gravity columns. Unlike common practice in structural design offices in western United States, where the GFRS of reinforced concrete high-rise shear wall buildings is detailed as a moment-resisting frame (J. Hooper, personal communication, January 28, 2021), in Canada the GFRS is typically only designed to support gravity loads and later checked its ability to accommodate seismic displacement demands.

Another challenging issue to satisfactorily design columns is that under a seismic event, both the SFRS and GFRS will need to deform the same amount to achieve compatibility. This means that the columns might experience larger deformations than those estimated in analysis due to the nonlinear deformations experienced at the base of the shear walls. If these elements only were detailed for gravity forces, they could experience brittle failure since their capacity will be exceeded when subjected to seismic deformations. Failure of these elements compromises the gravity-load carrying capacity of the structure and could lead to total or partial collapse. Therefore, proper reinforcement is required to prevent tragedies such as the Pyne Gould Corporation building collapse previously discussed.

2.3 Code Requirements to Quantify Seismic Demands in the GFRS

The most accurate method to obtain the lateral demands in the GFRS is by carrying out a nonlinear time history analysis (NLTHA). In this assessment, the SFRS is modelled using nonlinear material models. The practicing engineer will need to decide if the GFRS elements will be modelled as linear-elastic (force-controlled) or nonlinear (deformation-controlled elements). If the first approach is considered, enough strength should be provided to the GFRS to ensure these elements remain linear elastic. If the GFRS is modelled as nonlinear, adequate seismic detailing should be provided to ensure consistent levels of ductility are achieved.

Accurate NLTHA is challenging. It is a laborious and time-consuming process that requires a highly-skilled engineer or team to obtain reliable results. Furthermore, buildings in western Canada are designed following prescriptive requirements of NBC 2015 (NRC, 2015) and CSA A23.3-19 (CSA, 2019) which do not require a detailed nonlinear analysis. Instead, these codes follow a linear-elastic analysis to estimate the seismic demands in columns and slabs that do not belong to the SFRS once they have been designed for gravity forces only. The following sections provide an overview of the requirements in the Canadian (CSA A23.3-19) and United States (ACI 318-19) concrete standards as they relate to the seismic design of elements of the GFRS. The ACI 318-19 code clauses were not assessed in this study, but are provided to serve as a point of comparison.

2.3.1 Canadian Code

CSA A23.3-19 provides structural engineers with two approaches to estimate the seismic demands in the GFRS, the General Analysis and Simplified Analysis. The General Analysis has four requirements to fulfill as described in Section 2.3.1.1. The Simplified Analysis is a shortcut to the General Analysis and complies with three of the General Analysis requirements by subjecting the building to the drift profile observed in Figure 2.1. Requirement c) listed in Section 2.3.1.1 is not satisfied by displacing the structure to the previously mentioned drift profile.

2.3.1.1 General Analysis

§ 21.11.2.1 of CSA A23.3-19 describes the general analysis to estimate the seismic demands in the GFRS. The requirements for a linear-elastic analysis are:

a) The full structure (GFRS and SFRS) needs to be subjected to the design displacement Δ. Δ is the design displacement at top of the gravity-frame obtained following § 4.1.8.13 of NBC 2015. The displacement needs to account for torsion effects, accidental torsion, and foundations movements. Additionally, it needs to be multiplied by the ductility and overstrength factor, R_d and R_o, respectively.

b) The SFRS must include reduced section properties at locations where plastic hinges are expected. This accounts for the inelastic displacement of the seismic-force resisting system.

c) Upper-bound effective stiffness factors must be provided for all members not part of the SFRS to make a safe estimate of the forces in these elements.

d) The interstorey drift ratio within the plastic hinge should not be less than 60% of inelastic rotational demand. This lower-bound drift limit is applied to account for the shear strains in this region.

2.3.1.2 Simplified Analysis

The practicing engineer could decide to follow the previous procedure or carry out the Simplified Analysis described in § 21.11.2.2 of CSA A23.3-19 in order to obtain the demands in the GFRS: According to this Simplified Analysis procedure, Requirements a), b), and d) of the General Analysis are satisfied if the drift profile of Figure 2.1 is applied to the full structure.

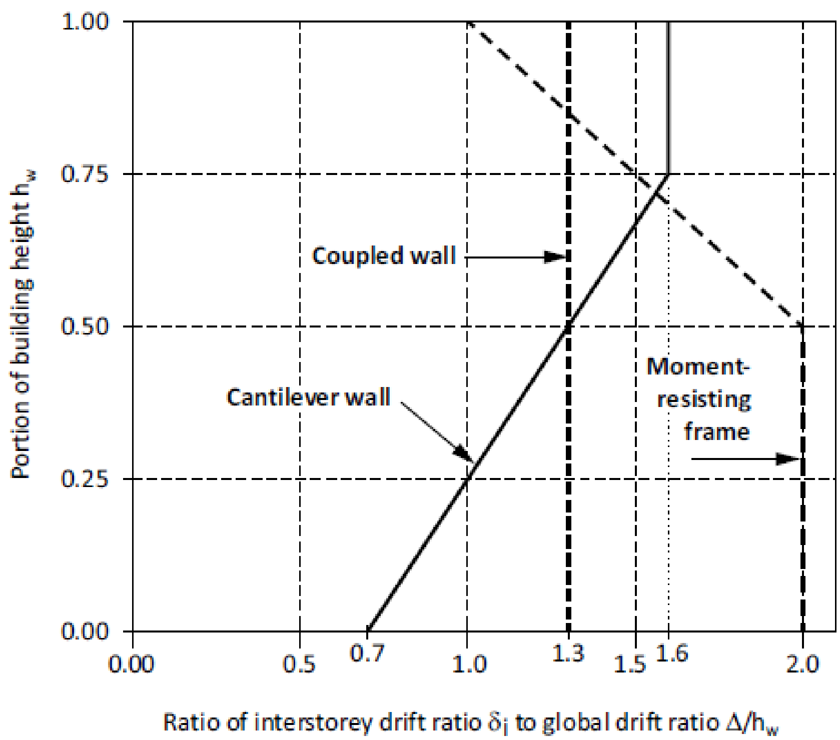

Figure 2.1 Envelope of minimum interstorey drift ratio over the building height (CSA, 2019).

In Figure 2.1, Δ is the design displacement at the top of the gravity frame following the NBC 2015 (NRC, 2015) guidelines. This displacement should account for torsion effects, including accidental torsion, and foundation movement.

The purpose of this clause is to ensure if the gravity design of the GFRS is able to accommodate the anticipated seismic demands. If the Simplified Analysis results indicate that the demands exceed the maximum allowed induced bending moment (refer to Section 7.4), proper seismic detailing is to be provided according to § 21.11.3 of the CSA 123.3-19 standard. Additionally, the vertical loads from the pushover analysis at the vertical elements of the GFRS is obtained by adding the shear forces at the immediate horizontal member above them and considering the contribution of all the superior levels. The minimum curvature for members of the GFRS within the should not be less than curvature demands described in § 21.5.7.2 and § 21.5.8.4.2 of the CSA A23.3-19 guidelines. For low seismicity regions in Canada or for stiff RCSW buildings this check could be omitted if any of the following conditions are met (Adebar, DeVall, & Mutrie, 2014):

- $S_a(0.2) \cdot I_E < 0.35g$
- $\delta_i < 0.5$ for all storeys

Where $S_a(0.2)$ is the spectral acceleration at 0.2 seconds, I_E is the importance factor, and δ_i is the interstorey drift ratio.

Because requirement c) of the General Analysis (§ 21.11.2.1 of CSA A23.3-19) is not met by this Simplified Analysis, one of the goals of this study is to provide realistic flexural effective stiffness modifiers to support the implementation of the Simplified Analysis. With this, the requirement gap found in guideline § 21.11.2.2 of CSA A23.3-19 could be fulfilled and a comprehensive linear analysis following this prescriptive guideline could be implemented to estimate the seismic demands in the GFRS.

§ 18.14 of ACI 318-19 (ACI (American Concrete Institute), 2019) indicates that members that are not part of SFRS need to support gravity loads, vertical ground motion effects, and the seismic design displacement. Models used to estimate the anticipated displacement caused by the design earthquake should include, if applicable, effects of cracked concrete, foundation flexibility, and deformation of floor and roof diaphragms.

The USA code has similar requirements on how to obtain the demands in the GFRS compared to the Canadian concrete standard. Both codes need the design engineer to apply the design displacement, consider the effect of cracking in concrete (effective stiffness factors), and account for foundation flexibility. However, ACI 318-19 does not specify a drift profile as a function of the SFRS inelastic displacement as done in the Canadian standard (refer back to Figure 2.1).

2.4 Alternative Method to Quantify the Seismic Demands in the GFRS

Beauchamp et al. (2017) proposed an alternative method to obtain the seismic demands in the GFRS components. This method does not support the implementation of the CSA A23.3-19 General or Simplified Analysis procedure, but rather recommends a distinct approach.

Beauchamp et al. (2017) proposed a response spectrum analysis in which elements of the GFRS had null stiffness. This method is labelled as GNS (GFRS with Null Stiffness). Although the scope of their study is limited to obtain the displacement demands in the columns, the authors mention that the method could be used to also compute the seismic demands in gravity-frame beams. The steps to obtain the seismic demands according to this method are as follows: 1) build the linear-elastic model considering the SFRS only accounting for cracking of concrete in the SFRS according to CSA A23.3-19, 2) from the previous step model, obtain V_d and V_e following the NBC 2015 guidelines. V_d is the design base shear and V_e is the elastic base shear force, 3) include the GFRS in the building model developed in the first step, 4) assign the upper-bound stiffness factors to the GFRS. Beauchamp et al. (2017) computed these factors following the lower-bound CSA A23.3-19 recommendations for the SFRS of clause 21.2.5.2 and arbitrarily increase them by 25% to obtain upper-bound values, 5) multiply the GFRS stiffness by F_{sr}, which is a factor equal to 10^{-2} to 10^{-3} to decrease its stiffness. Beauchamp et al. (2017) observed that a reduction factor equal to 10^{-2} yielded good results, 6) perform the response spectrum analysis in the complete structure model (GFRS+SFRS), 7) extract the seismic demands in the null stiffness GFRS. This demands are labelled as F_{GNS}, 8) last, compute the seismic demands of the GFRS following Equation (2.1)

$$F_{GFRS} = F_{GNS} \frac{1}{F_{sr}} \cdot \frac{V_d}{V_e} \cdot \frac{R_d R_o}{I_e} \tag{2.1}$$

R_d is the modification factor for seismic analysis that accounts for ductility. R_o is the seismic force modification factor for overstrength. This method did not consider foundation movement, all building models were fixed at grade level, and the structure below grade was not modelled.

Choinière et al. (2019) extend the method proposed by Beauchamp et al. (2017) by considering foundation movement. The soil structure interaction is assessed using two methods: a) a complete set of dashpots and springs and b) a single rotational spring under each RCSW. Method a) models the soil effect by adding dashpots and springs to every node below grade. Under the RCSW, a single rotational spring is included. The soil properties of dashpots and springs are obtained through impedance functions. “These functions can portray the dynamic properties of the soil surrounding the retaining walls as well as below columns and RCSW foundations" Choinière et al. (2019). Method b) is a further modelling simplification of the first approach. This method only includes a single rotational spring under each RCSW and fixes the rest of the nodes at the structure below grade. Either method does not model lateral springs or dashpots at the surface level because the soil is not well compacted to provide passive lateral resistance. After the soil has been modelled using one of the methods, Beauchamp's et al. (2017) procedure is followed to obtain the seismic demands at the GFRS components.

2.5 Effective Beam Width (EBW) Modelling for RC Slabs

In typical tall RCSW buildings, which have a central core and perimeter gravity framing, the slab provides a low framing flexural action throughout its full width when framing columns or walls. For this reason, it is a common practice for structural engineers to model the slabs using effective width beam elements. In this study, the slabs were modelled following Los Angeles Tall Buildings Structural Design Council guidelines (Los Angeles Tall Buildings Structural Design Council (LATBSDC), 2020). These guidelines are based on the findings of Hwang & Moehle (2000). A summary of how to obtain the effective beam width modelling approach is illustrated below.

To find the effective width of the slab b_{eff}, Equation (2.2) from Hwang and Moehle (2000) is used. c_1 is the depth of the column or wall framing into the slab and l_1 is the slab span. Figure 2.2 illustrates the definitions of c_1 and l_1 for the EBW model in a typical floor plan. For any level of the building, half of the EBW that spans between the wallumn and core will be computed using the depth of the wallumn. The other half will be obtained using the core geometric properties.

$$b_{eff} = \begin{cases} 2c_1 + \dfrac{l_1}{3} & \text{for interior frames} \\ c_1 + \dfrac{l_1}{6} & \text{for exterior frames} \end{cases} \tag{2.2}$$

The validation of EBW modelling will be assessed in Section 4.2.2 of this thesis.

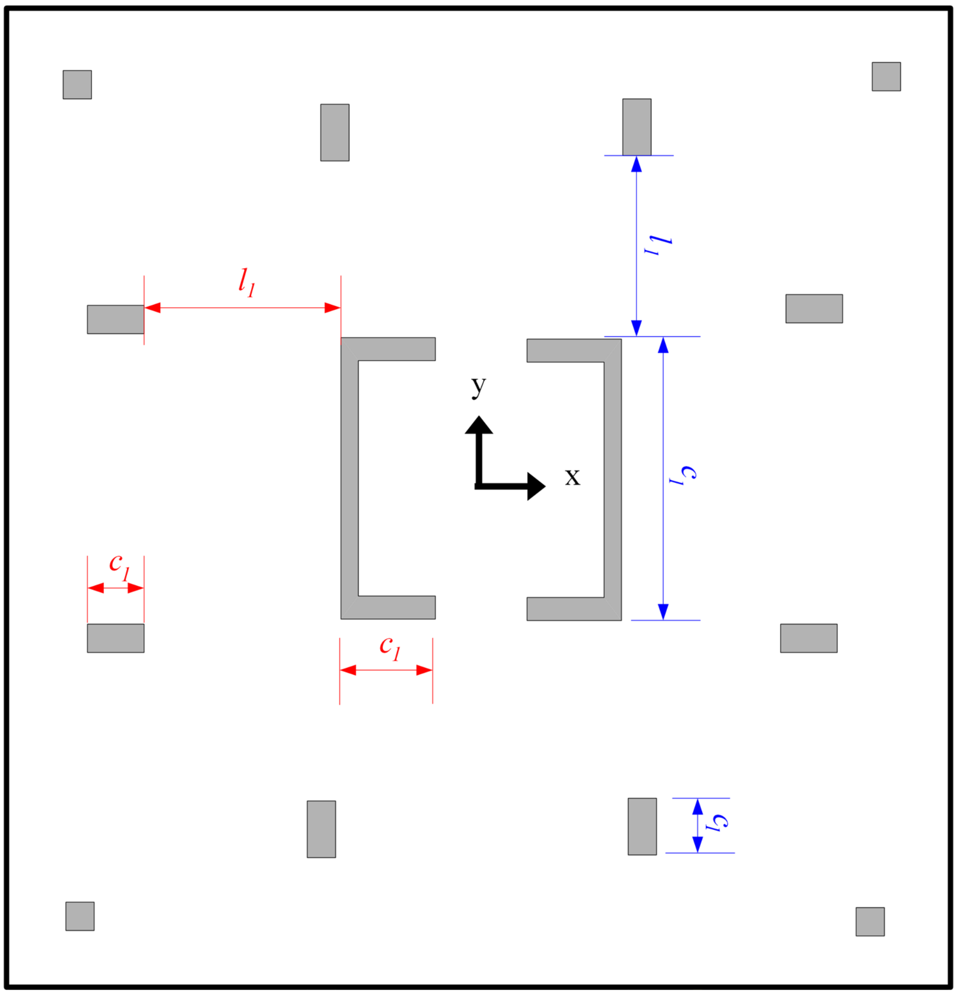

Figure 2.2 Floorplan definition of c_1 and l_1 for the x coupled and y cantilever direction.

2.6 Wall-Frame Interaction

In general, a cantilever wall system under lateral load deforms in a bending mode with single curvature. By contrast, a coupled wall system, will tend to deform in a shear mode (MacLeod, 1971). A frame system with rigid slabs will deform in a shear mode resulting in a double curvature at the columns. The mode of deformation in columns when a cantilever or coupled wall is connected to a gravity-frame depends on a number of factors. The deformation mode in the full building will depend on 1) the drift profile applied, 2) relative stiffness between slabs and columns, 3) amount of cracking in each element: walls, columns, and slabs. These will be explained in Section 2.6.1 of this thesis.

Understanding the deformation mode in the building is very informative because it will dictate the curvature seen at the GFRS columns. The curvature will influence the amount of cracking and effective stiffness of columns. For example, if a shear mode is governing the upper storeys of the building, each storey will experience double curvature and the top and bottom sections of the columns will see the largest demands and cracking. By contrast, if the flexural mode governs at the bottom of the building, the bottom ends of each column in each storey will see the largest demands and cracking (Abrams & Sozen, 1979).

2.6.1 Effect of Building Drift Profile on GFRS Column Curvature

Unlike a typical pushover (i.e., a concentrated displacement at top of the building), which imposes a bending deformation mode on the gravity-frame system and a single curvature in all its column elements, the enforcement of different drift profiles, such as those observed in Figure 2.1 will enact either double curvature (shear mode) or single curvature (bending mode) in the columns. The deformation mode when the Figure 2.1 drift profiles are applied depend on 1) relative stiffness between the EBW slabs and columns and 2) amount of cracking in the GFRS and SFRS. These effects are discussed below and supplemented with a sensitivity analysis included in Appendix A

It is generally accepted that a lateral pushover analysis of a frame system with flexurally rigid slabs framing into flexible columns will yield double curvature in the columns (Bazargani, 2014). Nevertheless, beams are never fully rigid in bending. The mode of deformation will depend on how stiff the columns are in relation to the slabs or beams. For this context the slab or beam definition will be used indistinctively. MacLeod (1971) proposed the following parameter, λ , to assess the deformation mode in a frame.

$$\lambda = \frac{\frac{E_{col} I_{col}}{h}}{\frac{E_{slab} I_{slab}}{l}} \tag{2.3}$$

The term $E_{col} I_{col}$ represents the flexural stiffness of the column, h is the height of the column, $E_{slab} I_{slab}$ represents the flexural stiffness of the slab, and l is the slab span. The closer λ is to zero the more likely a shear deformation mode will be dominant. Even a small amount of flexural stiffness in the slabs could be effective in restraining the flexural deformation imposed by lateral loads. However, if the slabs have yielded the load will be taken only by the columns and a bending deformation mode with single curvature will arise. Likewise, if the slabs are framing into stiff wallumns it is more likely to observe single curvature in these elements. Typical values (MacLeod, 1971) of Equation (2.3) that result in a shear deformation mode in RCSW buildings, are between 0.5 and 10. Within this range, contraflexure will be experienced by the GFRS frame columns around mid-height. Upper and lower storeys will be governed by the bending deformation of the wall. Thus, single curvature will be observed at those gravity-frame columns.

Under seismic loads, it is expected that the stiffer SFRS will take all the inertial forces. Once the walls have cracked or yielded, the GFRS will engage and start contributing to the lateral response. As the frame action in the GFRS is engaged, the slabs or beams will be the next member to experience large amounts of cracking and yielding, if a capacity design philosophy was followed. Once the beams yield, columns will experience a single curvature.

2.7 Axial Elongation of Reinforced Concrete Beams and Slabs

When a reinforced concrete beam experiences positive sagging bending moment, concrete cracking on the bottom tension face will shift the neutral axis of the section upwards from its original location. Similarly, if the beam is exposed to negative hogging bending moments, the neutral axis will move downwards from its original location when the top tension face cracks. As a result, the mid-depth fibre of the beam will be under tension. This phenomenon, coupled with the fact that the tensile strains in the longitudinal steel are larger than the compressive strains in the extreme concrete fibre in compression results in an extension of the member (Fenwick & Megget, 1993).

A beam free to elongate will not experience any additional stresses. However, in indeterminate structures the axial elongation of beams will be restrained by other elements. This will induce compression forces in beams or slabs. The axial elongation effect or beam growth has been experimentally tested. Results had shown that indeterminate frame assemblies have an overall strength at least 20% larger than determinate frame assemblies, in terms of lateral load carrying capacity. Moreover, the axial compression force induced in beams part of indeterminate assemblies increased their flexural strength (Zerbe & Durrani, 1989) by as much as 50% (Sakata et al., 1987).

The beam growth also affects the flexibility of beams and slabs. Large axial compression forces not only increase the strength of these elements, but also impact their stiffness. All restrained elements will see an increase in their stiffness caused by the induced compression forces. As a result, the assumption of having a very flexible beam element with low effective stiffness factors can be unrealistic.

Common linear-elastic structural analysis software is not able to capture the cracking of beam elements and their axial growth. More detailed models (Kim et al., 2004) able to link the axial and rotational behaviour of beams are needed to capture the induced axial forces caused by axial elongation. More powerful nonlinear software can model this effect if the proper element formulation (e.g., fibre elements or multilayer shells) is selected.

2.8 Effective Flexural Stiffness

Effective flexural stiffness factors are used for linear-elastic seismic analysis to achieve similar results to those observed in nonlinear models that are able to capture the inelastic response of reinforced concrete elements, consisting of rebar yielding and concrete cracking. These stiffness factors are usually expressed as a fraction of the gross moment of inertia of the cross-section.

Priestley (1998) and Elwood & Eberhard (2009) defined the effective flexural stiffness, EI_{eff}, of a reinforced concrete member as:

$$EI_{eff} = \frac{M'_y}{\phi'_y} \tag{2.4}$$

Where M'_y is the moment at first yield and ϕ'_y is the curvature at first yield. Watson et al. (1994), Benzoni et al. (1996), Elwood & Eberhard (2009) defined M'_y and ϕ'_y as the minimum moment and curvature developed when the extreme steel rebar in tension reaches the yield strain, ε_y, or when the extreme fibre concrete in compression reaches a strain equal to 0.002. This definition, hereinafter referred to as First Yield, is appropriate for elements that yield. For elements that do not yield, or experience demands lower than the yield force Equation (2.4) is not valid since it will result in an unreal flexural effective stiffness equal to the gross moment of inertia, even if member has cracked. Because the GFRS is not intended to dissipate seismic energy, less nonlinearity will be experienced by its members in relation to those of the SFRS. For these reasons, a different approach is required to characterize the effective flexural stiffness of its members.

The General and Simplified Analysis of CSA A23.3-19 described in this document (Section 2.3.1.1 and 2.3.1.2 of the standard) follows a displacement based approach rather than a force-based approach to determine the demands in the GFRS based on the notion that the gravity system will need to displace as much as the SFRS to achieve compatibility. One of the goals of this thesis is to find good agreement between the demands in the GFRS of a linear-elastic analysis model, by applying flexural effective stiffness factors, when compared to a detailed nonlinear model of the same structure when both models are subjected to the same level of deformation. An effective stiffness definition that is consistent with the goals of this study was developed by Paulay (2001). This definition states that the effective stiffness is the secant line from the origin to the point where the last deformation and demand was observed. This approach, hereinafter referred to as the Secant Stiffness was used throughout the development of this research project.

Figure 2.3 illustrates the effective flexural stiffness following the First Yield and Secant Stiffness approaches under different levels of bending moment demand, M_f. The First Yield approach will return the same flexural stiffness modifier whether the demands exceed M'_y or have just reached this value. If these stiffness modifiers are used in a linear-elastic model, the chances of overestimating the linear-elastic bending moment demands for elements that experience deformations considerably beyond yielding are high. On the other hand, for members that experience demands lower than M'_y the linear-elastic demands might be underestimated.

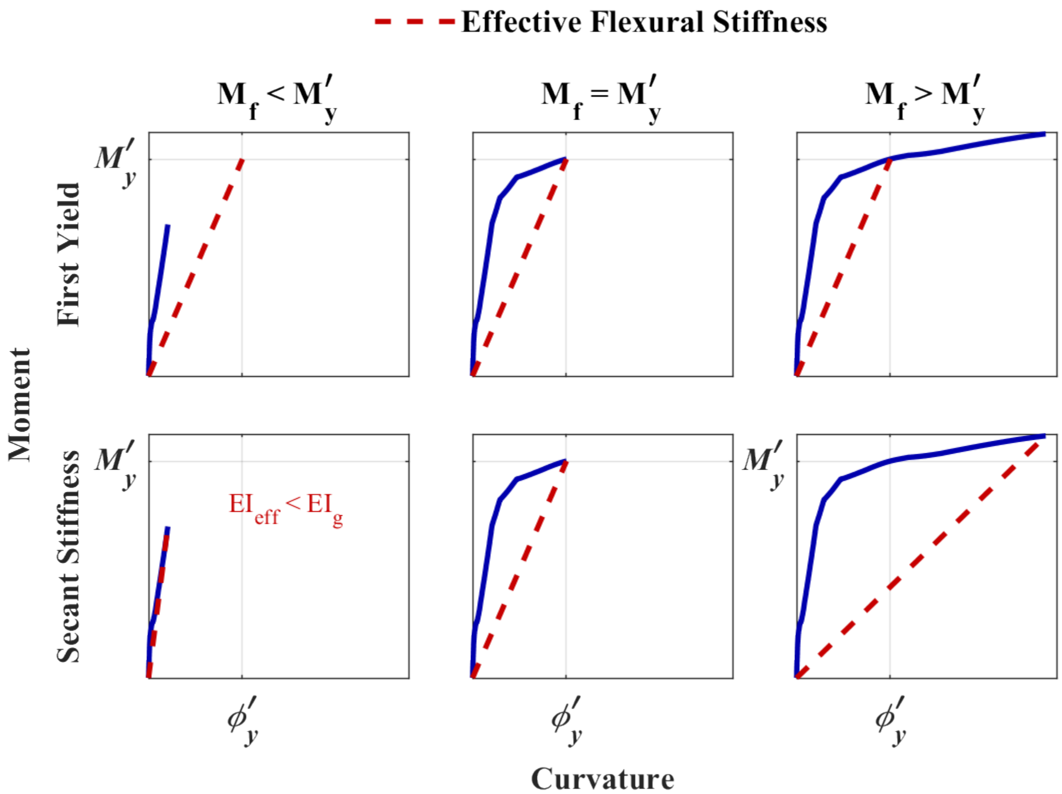

Figure 2.3 Effective stiffness approaches comparison for a member experiencing different levels of demands and deformation.

The Secant Stiffness approach will provide a suitable flexural effective stiffness modifier as a function of the bending moment demands and curvature experienced by the structural member. At low levels of curvature and cracking, this method will yield stiffness modifiers close to the gross stiffness. At high levels of cracking and beyond the first yield, the resultant effective stiffness will be less.

Chapter 3: Archetype Building Description and Structural Design

3.1 Building Description

The archetype building evaluated in this study is a 30-storey residential structure representative of the most common typology of RCSW buildings in the Metro Vancouver region. The SFRS is composed by a 7.3 m long and 460 mm thick cantilever walls in the *y* direction, as shown in Figure 3.1, and coupled walls in the *x* direction composed by 2.5 m long and 610 mm thick wall piers connected by 750 mm deep coupling beams. The floor plate dimensions are 25.9 m in the longer cantilevered direction and 25 m in the shorter coupled direction. The gravity-force system consists of 205 mm thick flat slabs spanning from the central core to perimeter columns. Square columns are used at the corners of the floor plate and wallumns with a depth-to-width ratio equal to 2.5 are used at other locations. The cross-section of these two vertical elements change throughout the height of the building as summarized in Table 3.4 and Table 3.5. The ground floor of the building has a storey height of 3.8 m, while upper storeys have a uniform height of 2.9 m each. The building has a 5 m tall bulkhead above the 30^{th} floor, resulting in a total height above grade of 92.9 m. Below grade, there are three basement levels with a storey height of 3 m each.

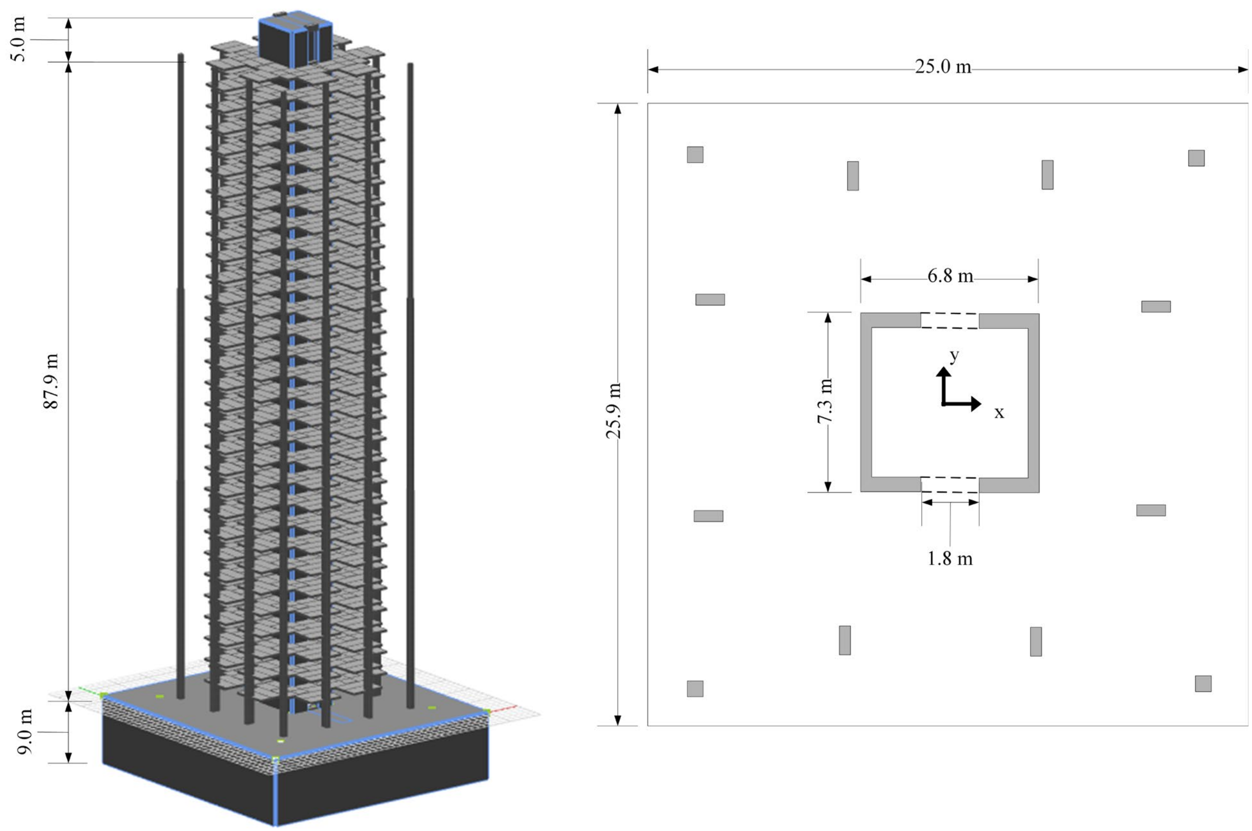

Figure 3.1 Isometric and floorplan view of the assessed building model.

A three-dimensional model of the building was created in Oasys (Arup, 2021) to obtain the design loads. The RCSW and retaining walls were modelled using two-dimensional shell elements. The columns and headers were modelled as one-dimensional beam-column elements. The slabs were also modelled with one-dimensional elements using an equivalent beam width approach. While the SFRS and GFRS above grade accounts for cracking of concrete, the basement is assumed to remain linear elastic. The flexural effetive stiffness of the SFRS walls are $0.5E_cI_g$ and $0.6E_cI_g$ (Eksir Monfared et al., 2021) for the coupled and cantilevered direction, respectively. Foundation movement and flexibility of the soil surrounding the basement was neglected. The model was assumed to be fixed at the top of the mat foundation.

Nominal concrete and steel material properties were used for the preliminary analysis and design of the SFRS and GFRS. Table 3.1 shows the nominal concrete properties assuming normal weight concrete with a density equal to 2400 kg/m3. Table 3.2 lists the material properties for steel reinforcement, which uses Grade 400W steel.

Table 3.1 Nominal concrete material properties for design (Eksir Monfared, 2020).

Elements	Level	Nominal f'_c [MPa]	Nominal E_c [MPa]
SFRS + GFRS columns	21 to 31	30	29,300
	11 to 21	35	31,100
	Basement to 11	45	34,300
GFRS slabs	Basement to 31	35	31,100

Table 3.2 Nominal steel reinforcement material properties for design for all levels and structural members.

Nominal f_y [MPa]	E_s [MPa]
400	200,000

3.2 SFRS Design

The modelling and design of the SFRS was done as part of Eksir's Monfared (2020) Master's Thesis. An overview of the design process and modelling assumptions is provided here, but the reader can refer to Eksir Monfared (2020) and Eksir Monfared et al. (2021) for further details.

A linear-elastic model was developed in GSA (Arup, 2021). RCSW, slabs, and retaining walls below grade were modeled as 2D shell elements. Columns and coupling beams were modelled using 1D beam-column elements. Moment releases were applied to the ends of the gravity-frame columns to prevent any sort of contribution to the lateral resistance of the building system. "The building was designed for a 2% in 50 years hazard level Site Class C spectrum, including 10% of accidental torsion" (Eksir Monfared et al., 2021). The gravity loads considered for design can be retrieved from Table 3.3. The total seismic mass for the modal analysis resulted in 144MN. The first three periods of the building are 5.57 s, 5.41 s, and 2.85 s for the translational coupled direction, translational cantilevered direction, and torsional mode, respectively. "The ductility and overstrength factors, R_d and R_o, are equal to 3.5 and 1.6, respectively, in the cantilevered direction, and 4 and 1.7, respectively in the coupled direction" (Eksir Monfared et al., 2021). The coupling beams were designed first, as their overstrength affects the RCSW design. Large nonlinear deformations are expected in these elements. For this reason, "demand-to-capacity ratios up to 1.25 are permitted by the standard. The amplifying factor of axial forces at grade for the RCSW due to the effect of coupling beam overstrength was found to be 1.6" (Eksir Monfared et al., 2021). The plastic hinge length in the RCSW walls was limited to 12.9 m as required by CSA A23.3-14. Amplification of shear demands due to flexural overstrength and higher modes was accounted when providing the steel reinforcement for the boundary regions in the RCSW.

At all levels, the provided coupling beams had a depth of 750 mm, a width of 460 mm, the longitudinal reinforcement was 6-30M at 16.2°, and 10M buckling prevention ties were provided every 100 mm. All boundary regions of the RCSW had 10M ties every 150 mm from level -3 to 6, at other levels the tie spacing was increased to 300 mm. For levels -3 to 21, 12-25M longitudinal steel rebars were provided at the corner boundary regions of the C-shape RCSW, for levels 21 to 31 the longitudinal reinforcement provided was 12-20M. At the inner boundary region located in the coupled piers, the provided longitudinal reinforcement was 10-25M for -3 to 21, for levels 21 to 31 the longitudinal reinforcement was set to 10-20M. At the cantilevered wall pier panel zone, 2-15M longitudinal rebars were provided every 350 mm for all levels. The cantilevered panel shear reinforcement was 2-20M @ 150 mm for levels -3 to 6, 2-15M @ 200 mm between levels 6 to 21, and 2-15M @ 300 mm at other levels. The coupled wall pier panel zone was provided with 2-15M @ 250 mm for longitudinal reinforcement. The provided shear reinforcement in the coupled panel zone was 2-20M @ 200 mm for levels -3 to 6 and 2-15M @ 250 mm for other levels.

3.3 GFRS Design

The GFRS was designed for gravity forces only as is typically done in design practice. This system will later be checked in Section 7.4 to ensure it can accommodate lateral demands. The design shown in this section was done by Dr. Jose Centeno and Glotman Simpson Consulting Engineers. The geometry and reinforcement layout for columns and slabs part for the GFRS, see Table 3.4, Table 3.5 were designed follwing the NBC 2015 (NRC, 2015) load combinations and CSA A23.3-14 (CSA, 2014) gravity design clauses for reinforced concrete. The CSA A23.3-14 concrete standard clauses were followed over the CSA A23.3-19 design guidelines because the CSA A23.3-

14 is the design standard for concrete structures enforced in Vancouver, BC at the time of writing. The loads for gravity design are found in Table 3.3.

Table 3.3 Design Gravity Loads.

Load	Type	Value
Dead Loads	Selfweight	2400 kg/m^3
	Superimposed dead load	0.72 kPa
	Façade	1.9 kN/m
Live Loads	Tower live load	1.9 kPa
	Grade live load	4.8 kPa
	Basement live load	2.4 kPa

The superimposed dead load is applied at all levels. The façade load is applied around the perimeter of the tower and grade levels. Equation (3.1) is the factored load combination (NRC, 2015) for gravity design of columns of slabs.

$$1.25D + 1.5L \tag{3.1}$$

In this equation, D and L are the dead and live loads, respectively.

3.3.1 Columns Gravity Design

For the gravity design, the longitudinal reinforcement for columns was obtained through a compressive analysis following Equation (3.2) of clause § 10.10.3 of CSA A23.3-14 (CSA, 2014).

$$P_{r,\max} = (0.2 + 0.002h)P_{ro} \leq 0.8P_{ro} \tag{3.2}$$

$P_{r,\max}$ is the maximum compressive force resistance and P_{ro} is defined in Equation (3.3)

$$P_{ro} = \alpha_1 \phi_c f_c^{'} (A_g - A_{st}) + \phi_s f_y A_{st} \tag{3.3}$$

Where α_1 is the ratio of average stress in the rectangular compression block to the specified concrete strength. ϕ_c is the material strength reduction factor for concrete, $f_c^{'}$ is the specified concrete strength, A_g is the section gross area, A_{st} is the longitudinal steel reinforcement area, ϕ_s is the material strength reduction factor for steel bars and f_y is the specified yield strength for steel.

The longitudinal reinforcement obtained from Equations (3.2) and (3.3) needs to fulfill the minimum requirement specified in § 10.5.1.2 of CSA A23.3-14 (CSA, 2014). Equation (3.4) denotes the minimum longitudinal reinforcement proportioned at each section of the structural column.

$$A_{s,\min} = \frac{0.2\sqrt{f_c'}}{f_y} b_t d \tag{3.4}$$

Where $A_{s,\min}$ is the minimum longitudinal reinforcement, b_t and d is the width of the tension zone and member depth, respectively.

Ties for compression members followed the recommendations of clause § 7.6.5 (CSA, 2014). The diameter of ties is the minimum recommended, i.e., 10M. The ties spacing, s, was selected following Equation (3.5).

$$s = \min \begin{cases} 16\phi_l \\ 48\phi_t \\ \min(b, d) \\ 300 \text{ mm for bundled bars} \end{cases} \tag{3.5}$$

Where ϕ_l is the diameter for longitudinal reinforcement, ϕ_t is the diameter for transverse reinforcement, b and d are the width and depth of the member, respectively. The building's plastic hinge zone is in the first 5 storeys (Eksir Monfared A. , 2020). Larger demands are expected within this region. As a result, column ties at the plastic hinge were spaced following buckling prevention ties clause § 21.2.8 (CSA, 2014), see Equation (3.6).

$$s = \min \begin{cases} 6\phi_l \\ 24\phi_t \\ 0.5\min(b, d) \end{cases} \tag{3.6}$$

The summary of the geometry and reinforcement layout for wallumns and square columns is presented in Table 3.4 and 3.5, respectively. All wallumns have ten longitudinal reinforcing bars and all square columns have eight. Wallumns and square columns are detailed with 10M ties and 5 cm of clear cover.

Table 3.4 Geometry and reinforcement layout summary for wallumns.

Level	Depth (d) [mm]	Width (b) [mm]	Longitudinal Bar Size (ϕ_l)	10M Tie Spacing (s) [mm]
21 to 31	760	305	10-25M	300
11 to 21	1015	405	10-30M	300
6 to 11	1140	460	10-35M	300
1 to 6	1140	460	10-35M	200

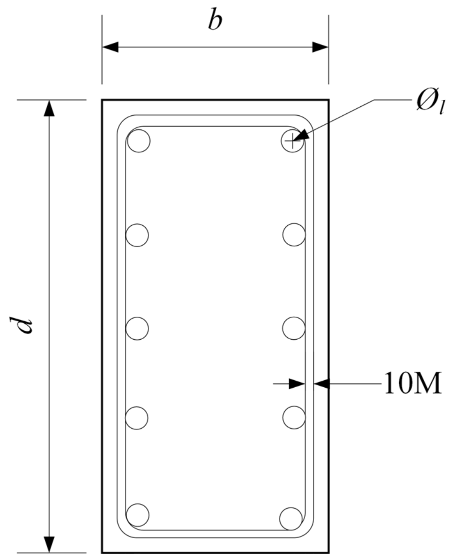

Figure 3.2 Wallumns layout.

Table 3.5 Geometry and reinforcement layout summary for corner square columns.

Level	Side (l) [mm]	Longitudinal Bar Size (ϕ_l)	10M Tie Spacing (s) [mm]
21 to 31	460	10-25M	300
11 to 21	610	10-30M	300
6 to 11	660	10-35M	300
1 to 6	660	10-35M	200

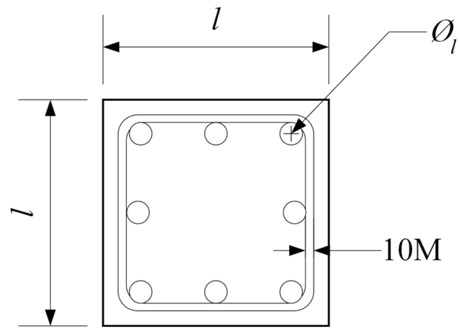

Figure 3.3 Square columns layout.

3.3.2 Slabs Gravity Design

The bending moment demands for the gravity design of the slabs come from the factored gravity forces at the columns, see Table 3.3. A cross-sectional analysis was performed to obtain the longitudinal reinforcement for sagging and hogging bending moment. It was checked that the factored bending moment demands M_f were larger than the factored bending moment capacity M_r. The factored bending moment capacity is defined in Equation (3.7).

$$M_r = \phi_s A_s f_y \left(d - \frac{\phi_s A_s f_y}{2\phi_c \alpha_1 f'_c b_t} \right) \tag{3.7}$$

The sagging and hogging longitudinal reinforcement, A_s, from Equation (3.7) was compared against the minimum required from Equation (3.4). The thickness of all the slabs was set to 205 mm and shear studs were provided at the slab-to-column and slab-to-core connections to prevent punching shear failure. The reinforcement layout designed by Dr. Jose Centeno and Glotman Simpson Consulting Engineers for both connections is displayed in Figure 3.4.

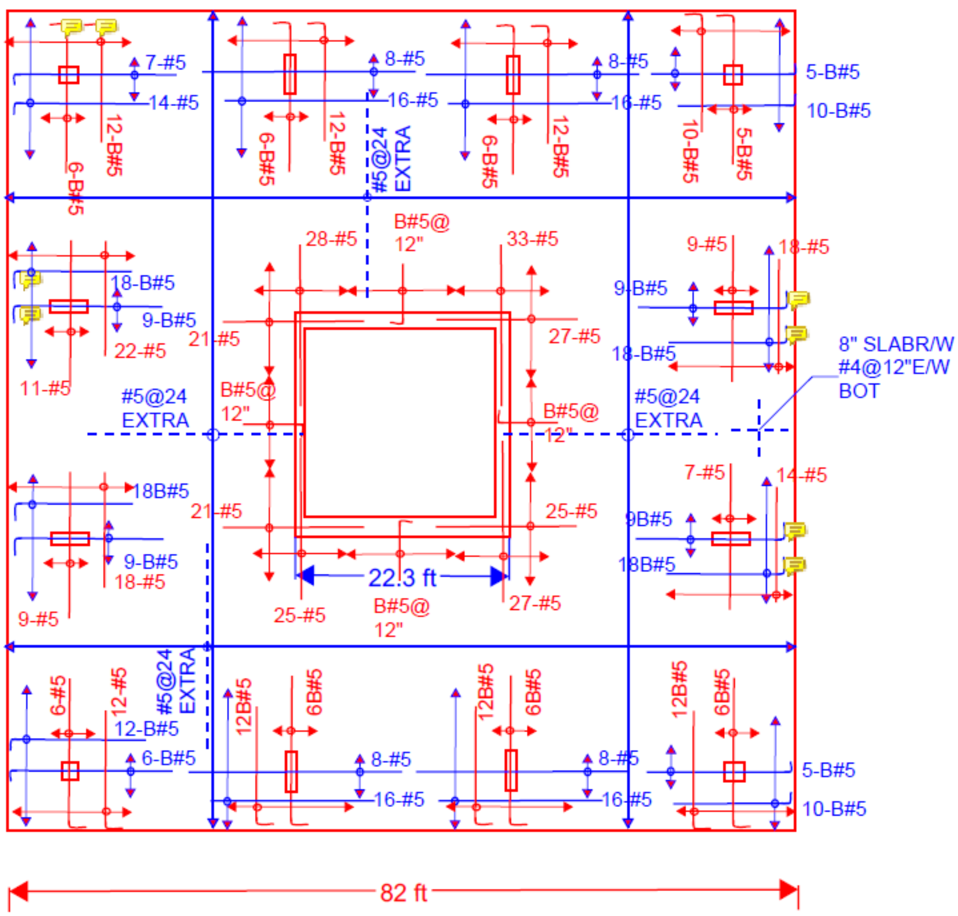

Figure 3.4 Steel reinforcement for slabs

Chapter 4: Linear and Nonlinear Static (Pushover) Analysis Modelling

In this chapter, the drift envelope applied to both linear-elastic and nonlinear models will be described in Section 4.1. The modelling assumptions considered for the linear-elastic and nonlinear static (pushover) analyses are discussed in Sections 4.2 and 4.3, respectively.

4.1 Drift Profile for Pushover Analysis

A static pushover analysis that enforces the drift profile of the Simplified Analysis described in § 21.11.2.2 of CSA A23.3-19 is required to obtain the GFRS seismic demands. This pushover analysis was done to ensure that the demands from a three-dimensional linear-elastic analysis model with appropriate flexural effective stiffness modifiers are in good agreement with the demands of an equivalent full nonlinear model. By carrying out these static pushover analyses it is possible to answer the questions of what the appropriate flexural stiffness modifiers for the elements of the GFRS are. The factored gravity forces applied on both models follow the gravity loads and factored load combination described in Table 3.3 and Equation (3.1), respectively. The seismic displacement applied in the static pushover analysis is the Simplified Analysis drift profile of clause § 21.11.2.2 of the CSA A23.3-19 standard. The design displacements in the cantilevered and coupled direction are required to define the Simplified Analysis drift profile. These design displacements are summarized in Table 4.1 and were obtained from the SFRS design, recall Section 3.2. which follows the NBC 2015 guidelines (NRC, 2015).

Table 4.1 Design displacements for the definition of the Simplified Analysis drift profile.

Direction	Δ [m]
Cantilever	0.997
Coupled	0.927

The drift profile shown in Figure 4.1 is the drift applied in each direction to both the linear-elastic and nonlinear models. The drift accounts for torsional effect, including accidental torsion, which was explicitly considered in the SFRS design. This correspondent drift was applied at all the nodes of each level.

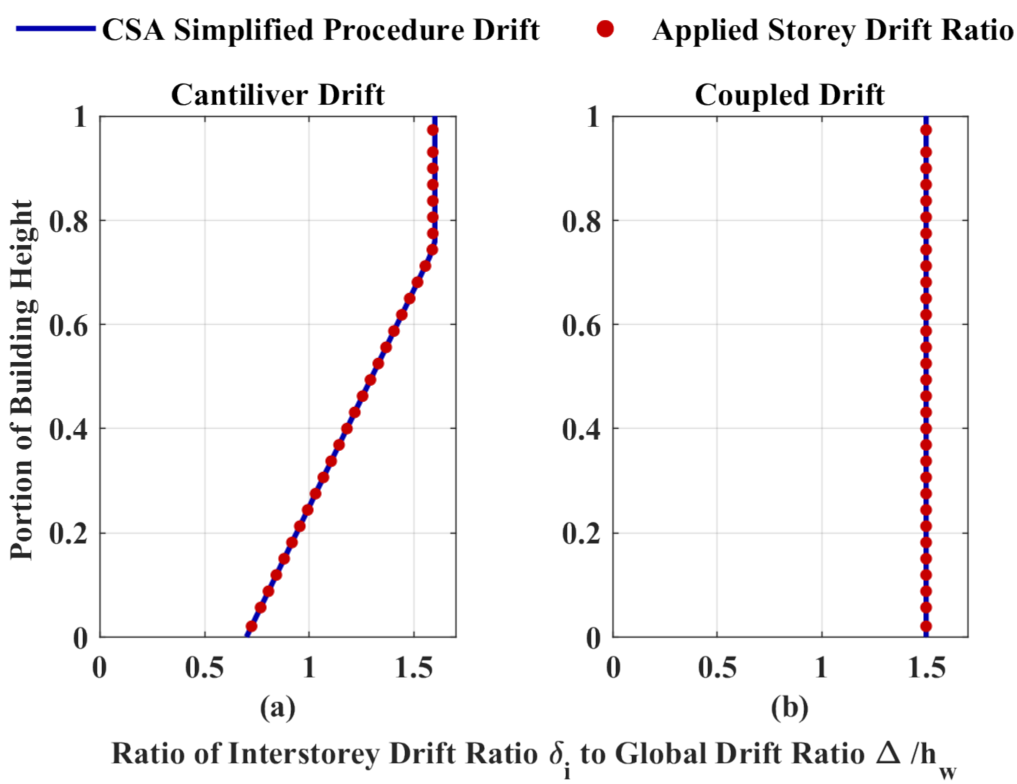

Figure 4.1 Storey drift ratio applied in the (a) cantilevered and (b) coupled direction.

Expected concrete and steel material properties, as recommended by PEER (Pacific Earthquake Engineering Research Center, 2017), were used in both linear and nonlinear static pushover analyses. Usually, linear-elastic analyses do not consider expected material properties because the purpose of this type of models is to design the structural elements. Nevertheless, one of the goals of this thesis is to achieve good agreement in the seismic demands between a detailed nonlinear model against an equivalent linear-elastic one. Because of this, it is important to compare both models with identical material properties. The impact of this assumption in the linear-elastic model results in having a SFRS and GFRS with the same stiffness as in the nonlinear model. Table Table 4.2 shows the expected concrete properties assuming a normal weight concrete density equal to 2400 kg/m^3. Table Table 4.3 lists the material properties for steel reinforcement, which uses Grade 400W steel.

Table 4.2 Concrete material properties for static pushover analyses.

Elements	Level	Expected f'_{ce} [MPa]	Expected E_c [MPa]
SFRS + GFRS columns	21 to 31	39.0	28,100
	11 to 21	45.5	30,350
	Basement to 11	58.5	34,400
GFRS slabs	Basement to 31	45.5	30,350

Table 4.3 400W steel reinforcement material properties for static pushover analyses.

Expected f_{ye} [MPa]	Expected f_{ue} [MPa]	E_s [MPa]
460	620	200,000

The variables shown in Tables Table 4.2 and Table 4.3 represent the following: $f_{ce}^{'} = 1.3 f_c^{'}$ is the expected concrete strength, E_c is the Young Modulus for concrete; $f_{ye} = 1.15 f_y$ is the expected yield stress of steel; $f_{ue} = 1.35 f_{ye}$ (CSA, 2009) is the expected ultimate stress of steel; and E_s is the Young Modulus for steel reinforcement. Except for the expected ultimate steel stress, the concrete and steel reinforcement expected strength values follow the LATBSDC (2020) recommendations.

4.2 Linear-Elastic Static Pushover Modelling

4.2.1 Slabs Modelling

For lateral analysis, it is possible to model the slabs following an effective width approach (Hwang & Moehle, 2000). Section 2.5 of this study summarized this method. To obtain the design demands in the slabs, these elements were initially modelled as 2D shell elements in the linear-elastic model, recall Section 3.1. For the static (pushover) analysis, the 2D shell elements were substituted by beam-column 1D effective beam width (EBW) slabs. The latter modelling technique was used since the slabs in the 3D nonlinear model were implemented as beam-column distributed plasticity fibre elements to obtain their moment-curvature response, see Section 5.1.

The EBW slabs are assorted into two groups. The first group represents the slabs that frame into the RCSW piers (EBW-to-core slabs) and the second group represents the slabs that frame into the wallumns (EBW-to-wallumn slabs). Equation (2.2) for interior frames is used to compute the effective with for core-to-slab and wallumn-to-slab connections. The EBW slab geometry and reinforcement used for the static (pushover) analyses are displayed in Figure 4.2 and Table 4.4, respectively. A validation of the EBW approach is shown in Section 4.2.2.

Table 4.4 Geometry and reinforcement layout summary for EBW slabs.

Direction	Level	Effective width (b_{eff}) [mm]	15M bars (hogging moment)	10M bars (sagging moment)	Connection type
Cantilever	2 to 31	7000	40	14	EBW-to-core
Coupled	2 to 31	7300	32	14	
Cantilever	21 to 31	4060	24	8	EBW-to-wallumn
	12 to 20	4570	24	10	
	2 to 11	4820	24	10	
Coupled	21 to 31	3970	27	8	
	12 to 20	4480	27	10	
	2 to 11	4730	27	10	

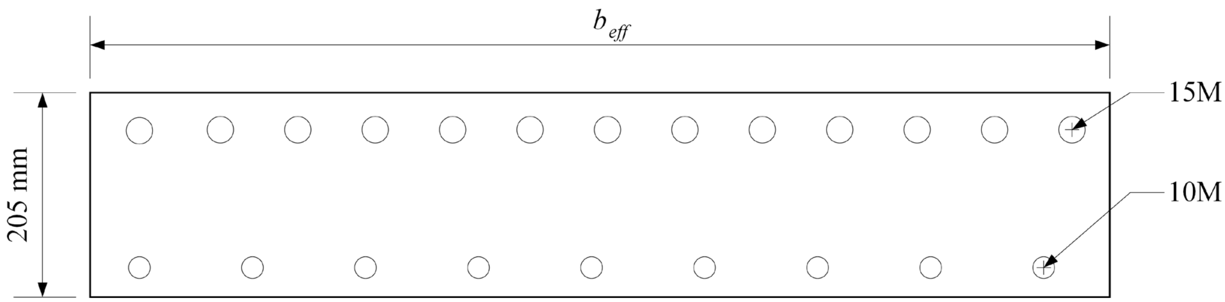

Figure 4.2 EBW slabs layout.

4.2.2 EBW Modelling Validation

It is crucial to verify that the EBW modelling technique does not affect the dynamic characteristics and stiffness of the building. To guarantee that this modelling approach does not alter the building's characteristics, the dynamic properties of a liner elastic model using EBW elements to simulate the slabs were benchmarked against the model used in design, which utilized 2D shell elements to model the slabs. The results of this exercised are summarized in Table 4.5. The comparison was made using cracked properties for the SFRS and moment releases at the GFRS columns.

Table 4.5 Dynamic properties of the linear-elastic building modelling slabs as 2D shell and EBW beam-column elements.

Mode Description	Periods [s]		Mass Participation	
	2D Shells	EBW	2D Shells	EBW
1st Translational Coupled	5.572	5.439	67.0%	66.2%
2nd Translational Cantilever	5.413	5.234	65.0%	64.1%
3rd Torsional	2.847	2.316	78.8%	64.3%

As observed in Table 4.5, the modelling of slabs as 2D shells or EBW results in small changes to the periods and mass participation in the first two translational modes. While the differences are more pronounced in the third torsional mode, this is of less importance because the building will only be subjected to a pushover analysis in both translational directions.

4.2.3 Analysis Stages for Linear-Elastic Static (Pushover) Analysis

The linear-elastic static (pushover) analysis was carried out in two different stages: 1) all elements except for the EBW slabs were analyzed and the corresponding gravity load was applied to the columns, as opposed to apply the uniform distributed load in the EBW slabs. This was done to prevent shifting of axial loads, from the wallumns to the core, caused by the high stiffness ratio of core walls in relation to the gravity columns; 2) the drift profile defined in Figure 4.1 was applied as a displacement to all the nodes of the same level. In this stage, all the building elements were considered for analysis. The two-stage analysis was required to ensure the gravity load wallumns were experiencing their intended axial load before the drift profile was applied. Table 4.6 summarizes the stages.

Table 4.6 Staged static (pushover) analysis for the linear-elastic model.

Stage	Structural elements in analysis	Applied load/displacement
1	All elements excluding EBW slabs	Factored gravity loads
2	All elements	Simplified Analysis drift profile

Using superposition, the results of the 1st plus the 2nd stage resulted in the overall demands at the GFRS in the linear-elastic model.

4.3 Nonlinear Static Pushover Analysis

To obtain the moment-curvature and the flexural effective stiffness of the GFRS elements, a detailed full nonlinear model of the structure was developed in LS-Dyna (LSTC, 2020). Basement components were modelled as linear-elastic elements. The model geometry is consistent with that of the linear elastic model, as previously shown in Figure 3.1. Prior to assigning the nonlinear material properties, in order to ensure the Oasys GSA and the LS-Dyna models had consistent dynamic characteristics, an eigen value analysis of both structural models was conducted (assuming uncracked section properties). The purpose of this comparison was to ensure the dynamic characteristics of both models were equivalent. While trivial, this check is important when developing equivalent models using different structural analysis software tools. A summary of the translational modes is shown Figure 4.1. The similarity in the translational periods serves as a point of departure to the linear and nonlinear static (pushover) analyses, in Oasys GSA and LS-Dyna, respectively.

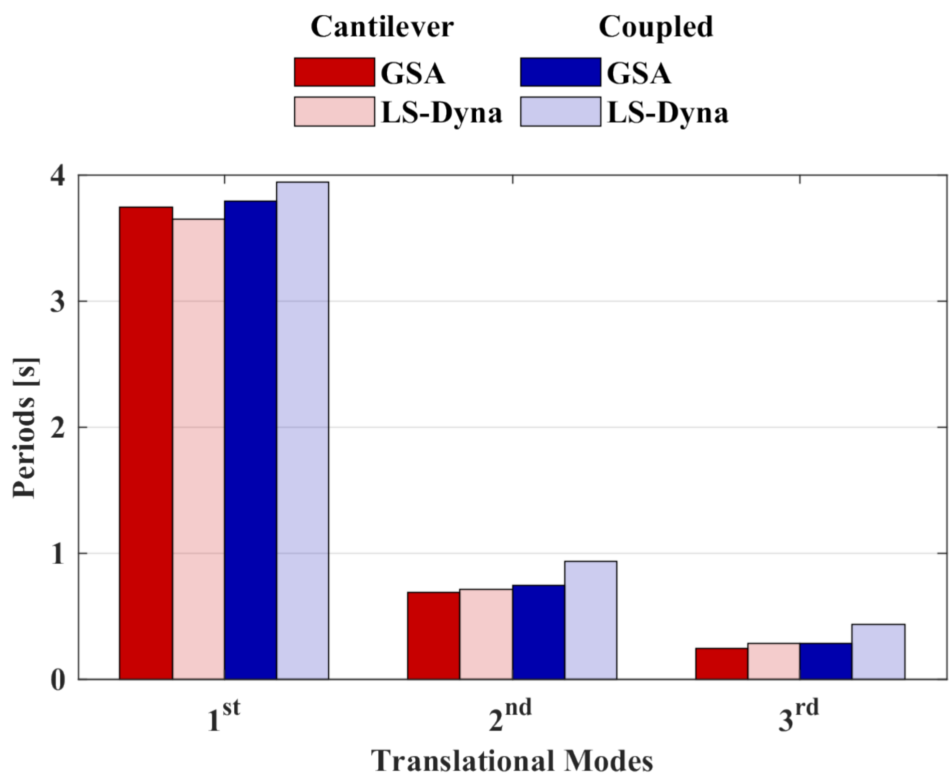

Figure 4.3 Uncracked periods comparison between the GSA and LS-Dyna building model.

4.3.1 Constitutive Material Models

This section provides an overview of the material constitutive models used in the fibre-based elements modelling approach of outrigger wallumns, non-outrigger square columns, and EBWs. The *MAT_CONCRETE_EC2 (ID 172) material card in LS-Dyna was used to model the confined and unconfined concrete fibres in the columns and EBW slabs. This model can capture concrete crushing in compression and cracking in tension. For all the unconfined concrete fibres of the GFRS under compression, the strain at maximum stress, ε_c, is set to 0.002. The crushing concrete strain, ε_{cu}, was assumed to be 0.0035 as per CSA A23.3-14 recommendations (CSA, 2014). The spalling of unconfined concrete strain, ε_{sp}, was set to 0.005 (LATBSDC, 2020). The tensile concrete behaviour was computed following Massicotte et al. (1990) and LSTC (2020) recommendations. The tensile strength was calculated as $f_t' = \sqrt{f_{ce}'}/3$ (Collins & Mitchell, 1987) and the cracking strain was defined as $\varepsilon_{cr} = f_t'/E_c$ (Massicotte et al., 1990). Last, the ultimate tensile strength is $\varepsilon_{ut} = 5\varepsilon_{cr}/0.22$ (Massicotte et al., 1990; LSTC, 2020). Refer to Table 4.7 for a summary of unconfined concrete properties in compression and tension.

Table 4.7 Unconfined concrete parameters for all GFRS components.

GFRS Components	Level	Compression Parameters				Tension Parameters		
		f_{ce}' [MPa]	ε_c	ε_{cu}	ε_{sp}	f_t' [MPa]	ε_{cr}	ε_{ut}
All	21 to 31	39.0	0.002	0.0035	0.005	2.08	0.00007	0.0017
	11 to 21	45.5	0.002	0.0035	0.005	2.25	0.00007	0.0017
	1 to 11	58.5	0.002	0.0035	0.005	2.55	0.00007	0.0017

The Mander et al. (1988) model for confined concrete was used to obtain the confined concrete strength and strain at maximum stress, f_{cc}' and ε_{cc}, respectively. The confined crushing concrete strain was computed as $\varepsilon_{cu} = 5\varepsilon_{cc}$ and the confined spalling strain is $\varepsilon_{sp} = 0.004 + \varepsilon_{cu}$. The confined crushing and spalling strain follow the equations used in Karthik and Mander (2011). The parameters for the confined concrete in tension are the same as for unconfined concrete. The summary of confined concrete properties for the GFRS square columns and wallumns is presented in Table 4.8. The EBW slabs do not have confinement reinforcement, therefore, no confined concrete fibres were used.

Table 4.8 Confined concrete parameters for the GFRS square columns and wallumns.

GFRS component	Level	Compression Parameters					Tension Parameters		
		f'_{ce} [MPa]	f'_{cc} [MPa]	ε_{cc}	ε_{cu}	ε_{sp}	f'_t [MPa]	ε_{cr}	ε_{ut}
Square columns	21 to 31	39.0	40.2	0.0025	0.013	0.017	2.08	0.00007	0.0017
	11 to 21	45.5	47.3	0.0026	0.013	0.017	2.25	0.00007	0.0017
	6 to 11	58.5	60.4	0.0027	0.014	0.018	2.55	0.00007	0.0017
	1 to 6	58.5	62.0	0.0030	0.015	0.019	2.55	0.00007	0.0017
Wallumns	21 to 31	39.0	40.2	0.0024	0.012	0.016	2.08	0.00007	0.0017
	11 to 21	45.5	47.3	0.0026	0.013	0.017	2.25	0.00007	0.0017
	6 to 11	58.5	60.3	0.0027	0.013	0.017	2.55	0.00007	0.0017
	1 to 6	58.5	62.0	0.0030	0.015	0.019	2.55	0.00007	0.0017

The compression and tension properties for concrete described in Table 4.7 and Table 4.8 are displayed in Figure 4.4

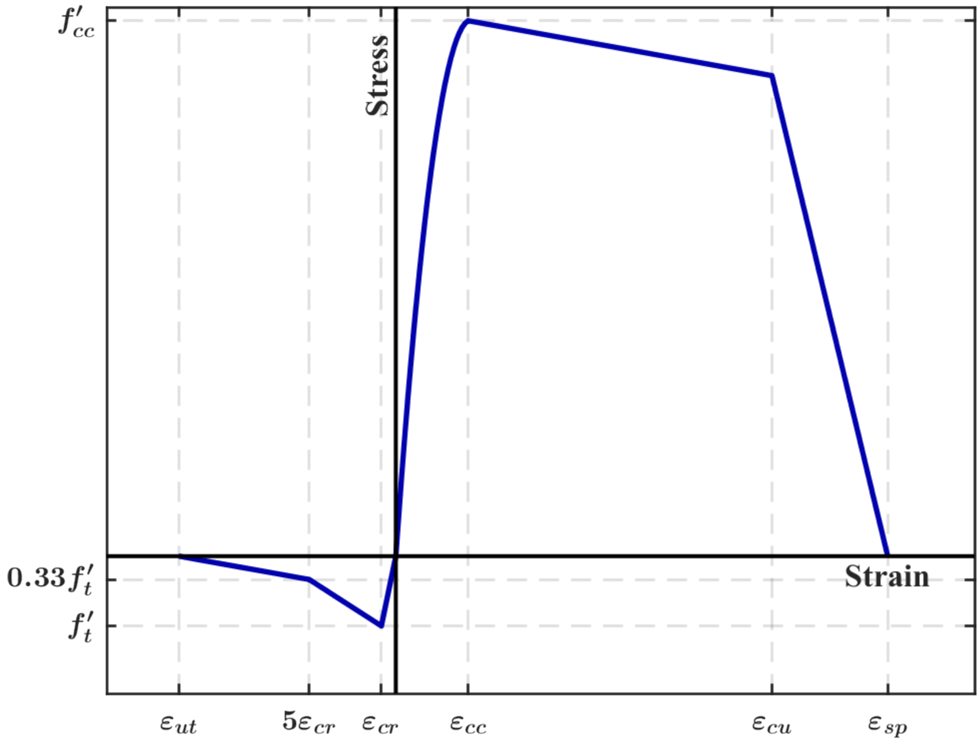

Figure 4.4 Concrete material model for nonlinear (static) pushover analysis.

4.3.1.1 Steel Reinforcement Model

The *MAT_HYSTERETIC_REINFORCEMENT (ID 203) material card in LS-Dyna (LSTC, 2020) was used to model the steel rebar fibres. This material model is ideal to capture the hysteretic behaviour of steel rebars. The tensile and compressive response is shown in Figure 4.5. Although no dynamic analyses are carried out in this study, the steel model follows a Bauschinger-type curve under cyclic loading and reloading. The steel buckles in compression at the onset of the ε_{cu} (Marafi et al., 2020), these values are found in Table 4.8. The common strain rupture value for grade 400W steel is equal to 0.13 (CSA, 2009) and the strain hardening was defined as $\varepsilon_{sh} = 0.006$ (Paultre et al., 2001).

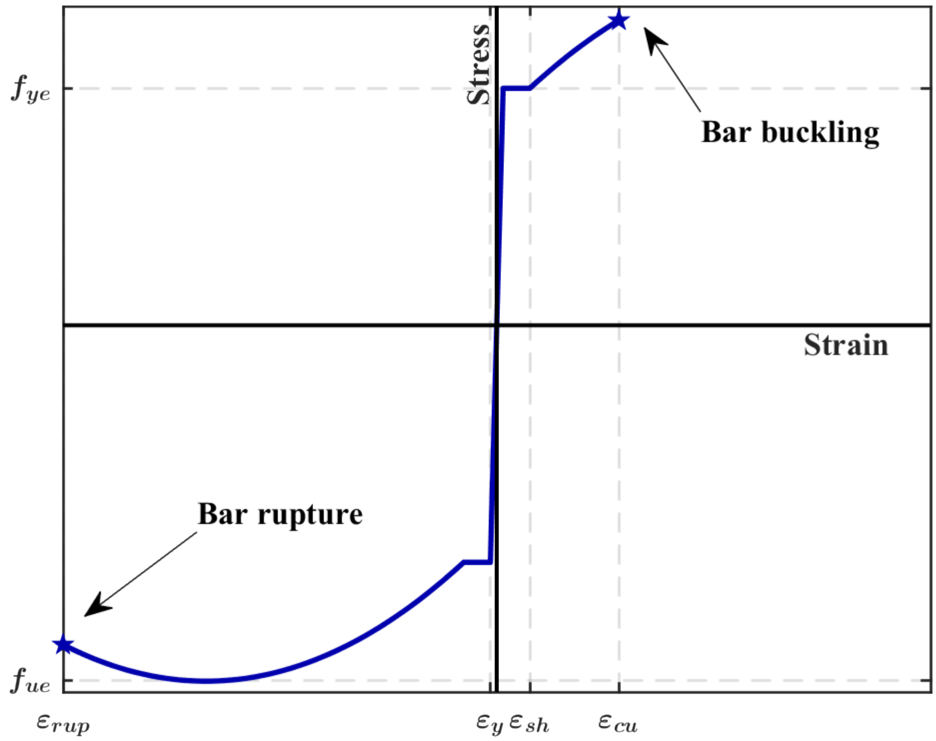

Figure 4.5 Tensile and compressive behaviour of the steel rebar fibres

4.3.2 Seismic-Force Resisting System Nonlinear Modelling

An overview of the SFRS modelling assumptions is provided here. The reader can refer to Eksir Monfared et al. (2021) for further details. The nonlinear behaviour of coupling beams was modelled using lumped plasticity flexural hinges at both ends of the beam element. The hysteretic behaviour of these elements was calibrated using experimental tests. "A cyclic backbone curve was used to describe the moment-rotation relationship of the flexural hinges and the stiffness terms were modified per PEER TBI (2017)" (Eksir Monfared et al., 2021). The cracking moment M_{cr} was calculated using the rupture modulus $f_r = 0.6(f'_c)^{0.5}$. "A constant moment resistance from initiation of yielding, M_y, to the ultimate point of the backbone, M_u, is assumed" (Eksir Monfared et al., 2021). The moment resistance of these elements was increased by 30% to account for the strength contribution of the slabs. The shear walls were defined using multi-layer shell elements. This type of shell element can capture the shear-flexure interaction. The longitudinal and transverse reinforcement was explicitly defined with specific orientations for each one. The confined and unconfined concrete were also included into the modelling. “The reinforcing steel follows a Bauschinger-type curve but is not able to capture fatigue. The post-yield properties of the reinforcement are: ε_{sh} = 0.006, ε_{rup} = 0.13, and $f_u = 1.35 f_y$. The constitutive material model for concrete followed the Mander model. ε_{co} was assumed equal to 0.002 and ε_{cu} = 0.003 for unconfined concrete and 0.0036 and 0.016 for confined concrete, respectively” (Eksir Monfared et al., 2021). The nonlinear behaviour of the walls was calibrated against experimental tests that “exhibited both nonlinear flexural and shear deformation towards the lateral displacement of the wall. The multi-layered shells performed well in terms of capturing the strength, stiffness, and cyclic behaviour of the experimental tests, therefore, enabled the validation of this element formulation” (Eksir Monfared et al., 2021).

4.3.3 Gravity-Force Resisting System Nonlinear Modelling

Fibre beam-column elements were chosen to capture the nonlinearity in the GFRS. With this element-type formulation it was possible to obtain the strain profile through the cross-sections of square columns, wallumns, and slabs. The strain profile is required to obtain the moment-curvature and consequently the flexural effective stiffness as will be described later in Chapter 5. The fibre beam-column elements follow a Hughes-Liu beam formulation (Hughes & Liu, 1981a; Hughes & Liu, 1981b) able to capture axial-flexural interaction. The slab-to-column and -to-wall nodal connection is modelled as rigid.

Figure 4.6 shows a diagram of the nonlinear GFRS storey modelling following a beam-column fibre element formulation. By default, LS-Dyna assigns a single integration point per beam-column element. Therefore, when modelling the square columns and wallumns, three beam-column elements were used at each storey to obtain an accurate picture of the cracking distribution throughout the elements' height (at the ends and mid-span). Sensitivity analyses showed that two or three beam-column elements per storey were enough to correctly capture the nonlinear behaviour without loss of objectivity in the GFRS beam-column elements. More than four beam-column elements yielded localization of strains at the base of the columns. The EBW slabs were modelled with two beam-column elements at each EBW-to-core and EBW-to-wallumn connection (i.e., four elements through the EBW span). Extensive analyses also showed that at least 30 fibres were needed to obtain realistic results. 54 fibres were used for the square columns, 55 for wallumns, and 64 on average for the EBW slabs.

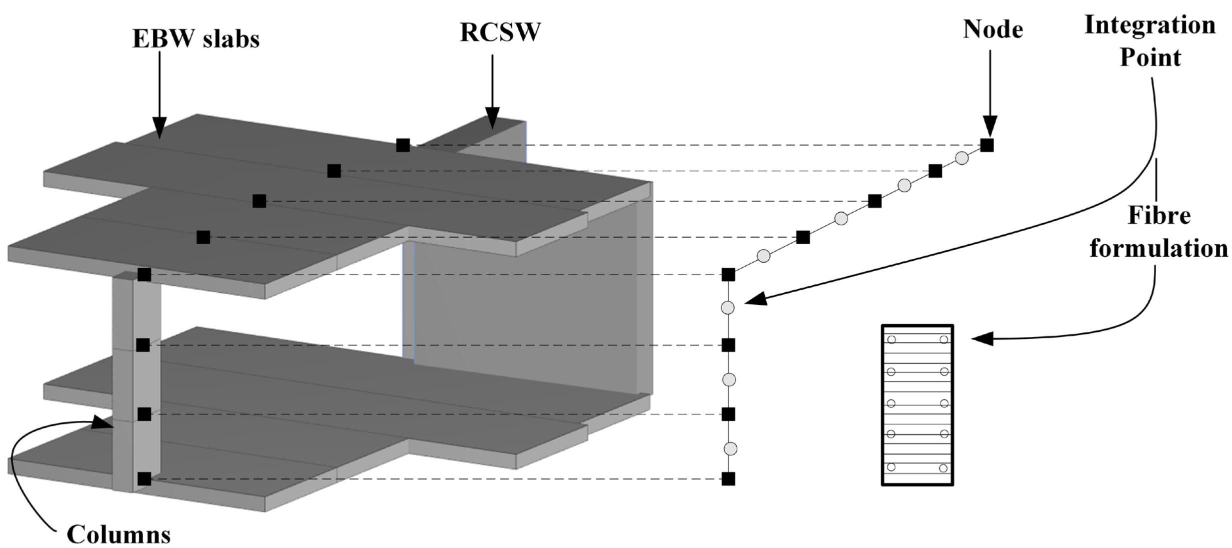

Figure 4.6 GFRS analytical model.

To validate the nonlinear modeling of the columns, different experimental tests (Saatciougluu & Ozcebe, 1989; Kono et al., 2006) were calibrated against virtual twins in LS-Dyna. As observed in Figure 4.7, which illustrates a subset of these experiments, the fibre beam-column element modelling approach performs well in terms of stiffness, strength, and cyclic behaviour. In general, the initial stiffness of the virtual experiments is slightly larger than that observed experimentally. This is explained by the following reasons: 1) The fibre model is stiffer than the experimental specimen because it does not account for shrinkage and temperature cracking effects that occur prior to the laboratory cyclic test (Spacone et al., 1996). 2) The concrete modulus of elasticity was estimated following the CSA A23.3-14 (CSA, 2014) recommendations (i.e., it was not reported in the experiments). This CSA 2014 equation provides a best estimate of the modulus of elasticity based on assumptions of aggregate size, which may differ from those employed in the laboratory specimens.

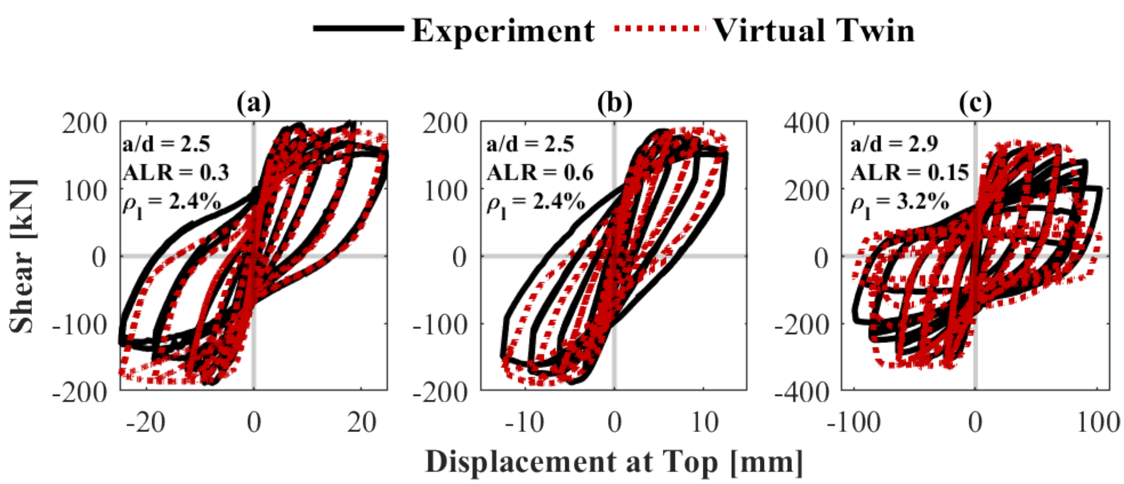

Figure 4.7 Virtual calibration against experimental tests of fibre beam-column elements; (a) D1N30 specimen (Kono et al., 2006); (b) D1N60 specimen (Kono et al., 2006); (c) U4 specimen (Saatciougluu & Ozcebe, 1989).

A flexural failure mode is expected at the EBW slabs. This assumption is valid since shear studs are provided at the EBW-to-core and EBW-to-wallumn connections which aims to prevent a punching shear failure. No experimental slabs specimens were validated against a EBW slab virtual twin model due to the lack of access to slabs experiments that failed in a pure flexural mode. However, the modelling behaviour was validated by checking the capacity of the EBW slabs against code equations in both positive and negative bending.

4.3.4 Analysis Stages for Nonlinear Static (Pushover) Analysis

As well as in the linear-elastic analysis, a two-stage analysis was needed in the nonlinear static analysis in order to prevent shifting of axial loads from the wallumns to the core. This was required to ensure the gravity-load wallumns had their intended axial design load before the pushover was carried out. This effect was caused by the high stiffness of EBW-to-core components. The elements considered in each stage are described in Table 4.6 and are the same as in the linear-elastic analysis performed in GSA. In the GSA linear-elastic analysis, each stage was a separate analysis and superposition was performed to obtain the overall demands in the model. By contrast, in the nonlinear LS-Dyna model, a single analysis was carried out, but each stage is introduced at different time intervals. The staged nonlinear static (pushover) analysis is shown in Figure 4.8 and summarized in the next paragraph.

In the first stage, all the elements except for the EBW slabs were included at the time t_1 = 0.0 s and the stiffness and mass of all the elements in this stage were ramped up in the following 2 s through the application of an acceleration representative of gravity. Here, all the gravity load was applied to the gravity-columns and RCSW to ensure they experience the appropriate factored axial load.

The six second interval time between t_2 = 2.0 s to t_3 = 8.0 s was adopted as a stabilization period in all the elements included in first stage. At t_3 = 8.0 s the second stage commenced. All the EBW slabs were included into the nonlinear model and their stiffness and mass was ramped up in the following 2 s. The EBW slabs were introduced in the second stage to prevent shifting of the gravity loads from the core to the outrigger wallumns. The addition of the EBW slabs caused larger dynamic effects in all building components. For this reason, a 10 s time interval from t_4 = 10.0 s to t_5 = 20.0 s was included to damp the dynamic effects caused by the inclusion of EBW slabs. Finally, at t_5 = 20.0 s the Simplified Analysis drift profile was applied. It took ten seconds to achieve the drift specified in Figure 3.5. The analysis ended at t_6 = 30.0 s. The addition of new elements at each stage causes vibration. Stiffer elements, like the EBW slabs, will cause larger dynamic effects. For this reason, mass damping is applied during the first twenty seconds of the analysis observed in Figure 4.8 until the element response converges. No frequency specific damping was applied since this is a static pushover analysis.

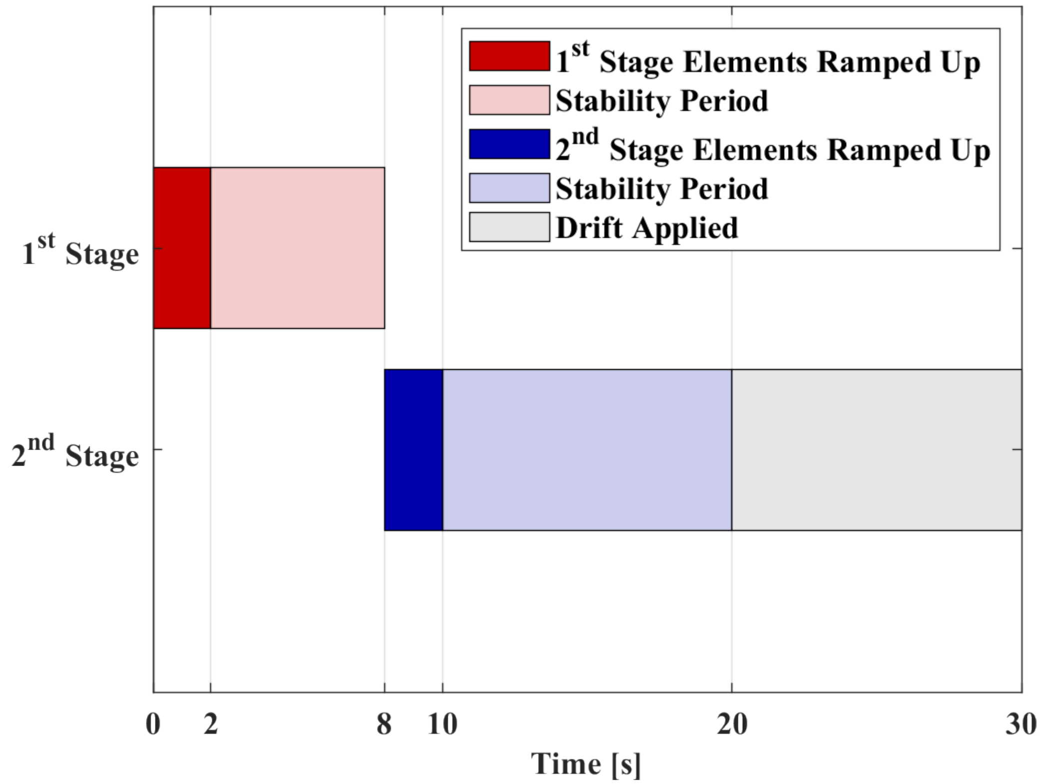

Figure 4.8 Timeline during the two-stage analysis of the nonlinear pushover in LS-Dyna.

4.3.5 Axial Elongation in EBW slabs

Referring back to Section 2.7, the nonlinear EBW slabs will crack and elongate. Consequently, internal compression forces will develop caused by the constraints of the indeterminate building system. On average, it was found that the EBW slabs in the LS-Dyna nonlinear model experience an axial load ratio of about 0.1 to $0.2A_g f'_{ce}$ when subjected to the drift profile described in Figure 4.1. This finding has the following effects: 1) the EBW slabs will be stiffer than anticipated due to the additional compressive axial force, attracting larger seismic demands; and 2) the slab's nominal flexural capacity will increase when considering the interaction of axial load and bending moment. The following figures in this section illustrate that the induced compressive force changes in proportion to the applied displacement, i.e., as the lateral displacement increases, rotations also increase, resulting in more cracking, axial elongation, and additional compressive axial forces. The rotation was computed as $(d/2)\cdot k$, where $d/2$ is the assumed plastic hinge length and k is the curvature.

The EBWs were classified according to the connection type, i.e. connection to a column/wallumn or to the core, and based on whether they were positioned in the "tension" or "compression" side of the analysis. The "tension" or "compression" side refers to the axial force that the outrigger wallumns experience. The wallumns that were in the "tension" side experienced less axial force, although the net axial load was always compressive. The "compression" wallumns experienced larger axial compressive demands. Figure 5.7 shows a diagram of the GFRS elements located in the "tension" or "compression" side for the cantilevered and coupled nonlinear static (pushover) analyses.

Figure 4.9 and Figure 4.10 show that the compressive axial force in the EBW slabs increase as lateral displacement and cracking in these elements build-up, supporting the literature review in Section 2.7. The axial load ratios in the EBW slabs range from 0.1 to $0.2A_g f'_{ce}$, approximately. These axial load ratios are consistent, according to the axial stiffness of the beams and slabs, to what is observed in other experimental (Zerbe & Durrani, 1989) and analytical studies (Kim et al., 2004). Zerbe & Durrani (1989) observed a 5% axial load ratio in the beam elements of an indeterminate multi-span experimental test. The beams in the experimental test had an axial stiffness 16 to 25 times smaller than the EBW slabs adopted in this nonlinear static (pushover) analysis study and described in Table 4.4. Kim et al's. (2004) analytical model of a five-storey four-bay frame building, observed around 10% of axial load ratio in beams with an axial stiffness 1.5 to 2.2 times smaller than the EBWs analyzed in this thesis.

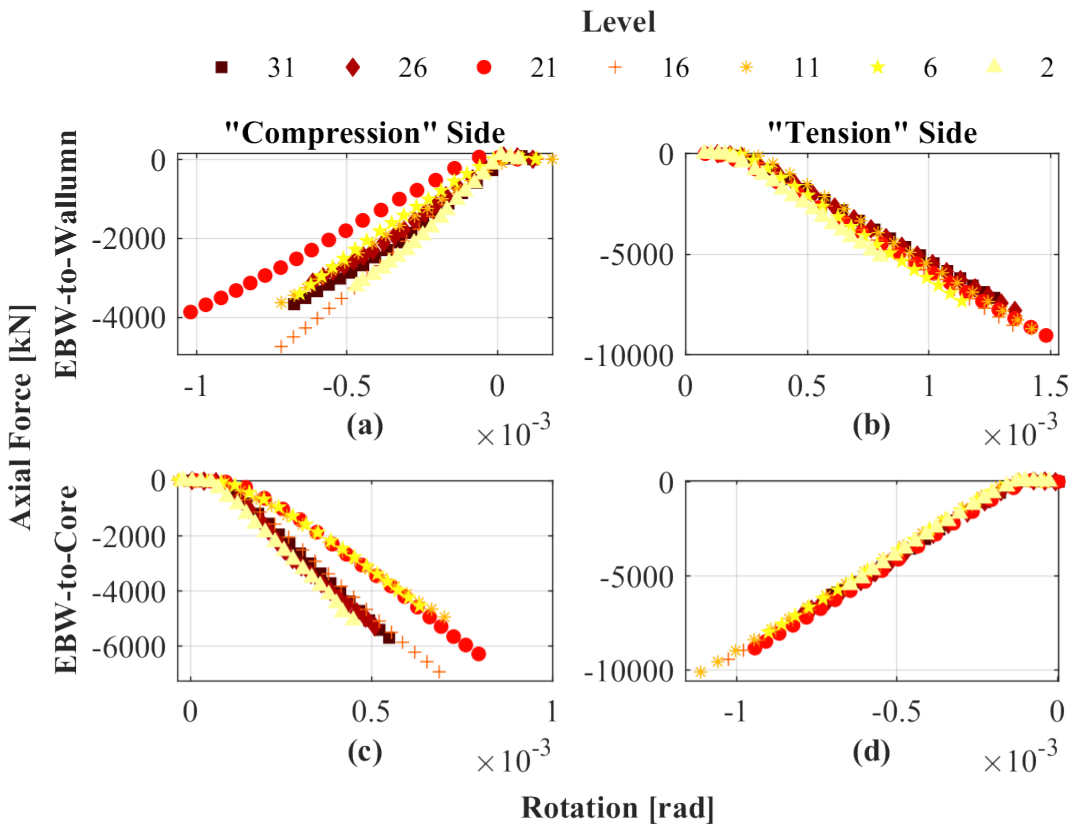

Figure 4.9 Increase in compressive axial force vs rotation for EBW slabs in the cantilevered direction; (a) EBW-to-wallumn “compression” side; (b) EBW-to-wallumn “tension” side; (c) EBW-to-core “compression” side; (d) EBW-to-core “tension” side.

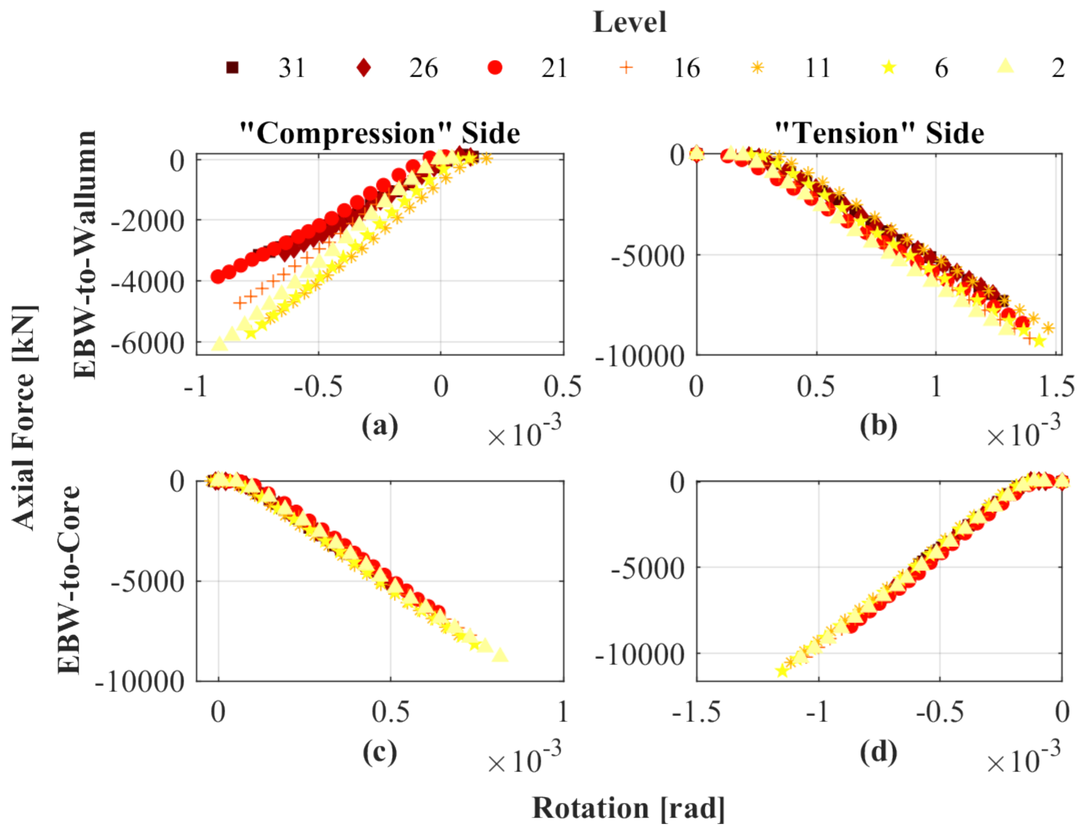

Figure 4.10 Increase in compressive axial force vs rotation for EBW slabs in the coupled direction; (a) EBW-to-wallumn "compression" side; (b) EBW-to-wallumn "tension" side; (c) EBW-to-core "compression" side; (d) EBW-to-core "tension" side.

Chapter 5: GFRS Component Effective Stiffness Results and Calibration

In Canada, the current code-prescriptive method to assess if the GFRS within a RCSW building can accommodate seismic displacements is the General Analysis (CSA, 2019) previously described in Section 2.3.1.1. However, practicing engineers could also choose to use the Simplified Analysis (CSA, 2019) which fulfills three out of four requirements of the General Analysis method by means of a prescribed drift profile previously illustrated in Figure 2.1. The only outstanding requirement is to ensure that upper-bound stiffness estimates of components of the GFRS are used in the analysis. Currently, the Canadian standard for design of concrete structures (CSA, 2019) does not provide specific stiffness modifiers to comply with this requirement. As it was previously discussed, structural design offices have adopted a flexural stiffness value of 10-25% of the gross stiffness for slabs and 70% for columns (J. Centeno, personal communication, November 11, 2021). Although this is a well-informed approach, a formal calibration of stiffness coefficients for EI_{eff} based on nonlinear analyses is needed for the linear seismic analysis of square columns, wallumns, and slabs that form part of the GFRS.

This chapter discusses the method followed to obtain flexural effective stiffness factors for members of the GFRS by leveraging results from the nonlinear model in LS-Dyna, as well as how these can be used for implementation in a linear-elastic analysis model to comply with the outstanding requirement of the Simplified Analysis. Section 5.1 describes the steps to follow to construct the moment-curvature plots for the GFRS components using the strain profile of cross-sections of relevant members in order to derive flexural effective stiffness values. Section 5.2 provides an overview of how these flexural effective stiffness modifiers were adopted in the linear-elastic model and an iterative calibration process followed to find agreement between seismic demands in the linear-elastic and the nonlinear analysis models. Section 5.3 provides a comparison between the linear-elastic and nonlinear bending moment demands observed in the components of the GFRS. Additionally, Section 5.4 summarizes the GFRS flexural effective stiffness factors obtained from this calibration exercise in support of appropriate stiffness factor recommendations for use in the Simplified Analysis procedure (CSA, 2019).

5.1 Moment-Curvature Analysis of Elements of the GFRS

The fibre beam-column element formulation used to model the GFRS in the nonlinear analysis model follows the assumption that plane sections remain plane. This results in a linear distribution of strain along the depth of the cross-section. Figure 5.1 shows the typical strain profile of a GFRS column throughout the nonlinear analysis pushover. Initially, when the global drift, Δ, is equal to zero, the cross-section strain profile is uniform since the member only experiences gravity loads, (refer back to Section 4.3.4). As the pushover analysis beings, some fibres will start to experience tensile strains resulting in cracking of the cross section. For the GFRS element shown in Figure 5.1, this first crack occurs when $\Delta = 0.64\Delta_y$, where Δ_y denotes the yield drift of the story. As the displacement continues, more concrete cracking is observed, which shifts the position of the neutral axis.

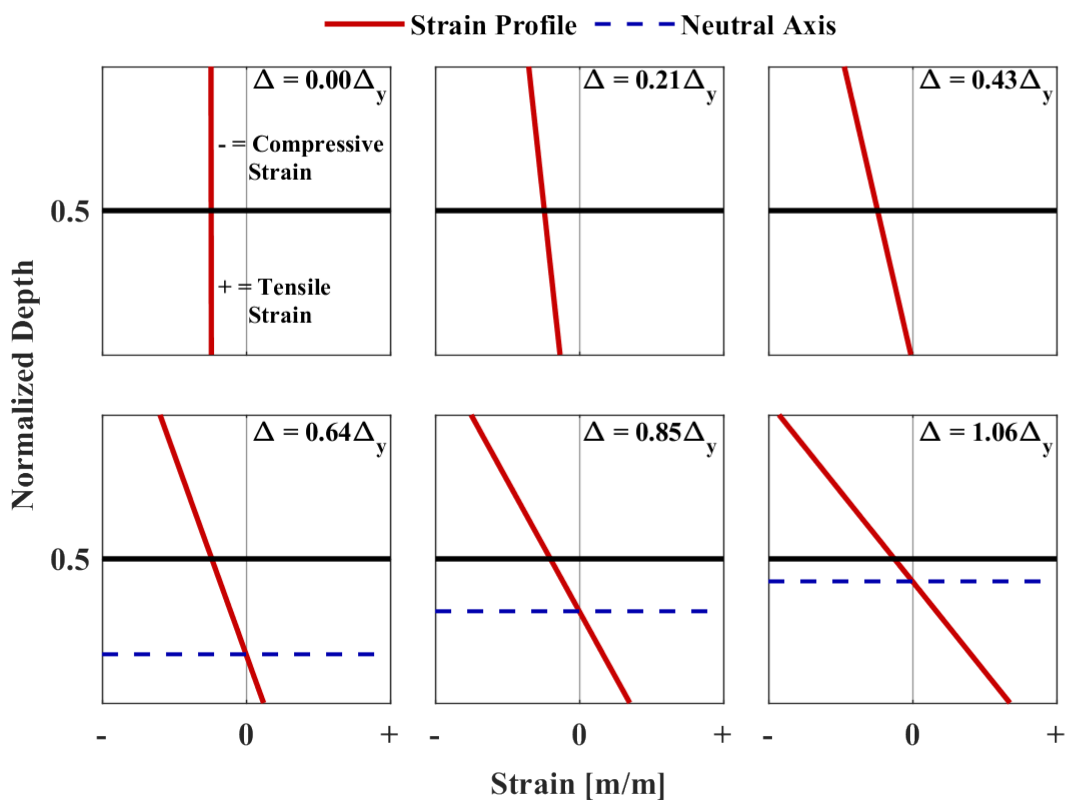

Figure 5.1 Typical strain profile evolution over time observed in the GFRS components obtained from the nonlinear pushover analysis.

5.1.1 Curvature Computation

LS-Dyna does not output the moment-curvature results of fibre-based beam elements. For this reason, the curvature was computed from the strain profile at each time step. The curvature is defined (Hibbeler, 2011) in Equation (5.1)

$$k = \frac{-\varepsilon}{y} \tag{5.1}$$

Where ε is the strain observed at a specific fibre and y is the distance from the neutral axis to the chosen fibre. Accordingly, the strain values of a fibre along with the distance from that fibre to the neutral axis are required at every time step to obtain the full moment-curvature analysis of the GFRS elements. While the strain is known at each time step as a direct output of the analysis, the y values need to be computed. The y distance varies at each analysis time step because the strain profile changes according to the deformation and cross-section cracking. Figure 5.2 shows how the distance from a specific fibre to the neutral axis decreases as the pushover analysis is carried out.

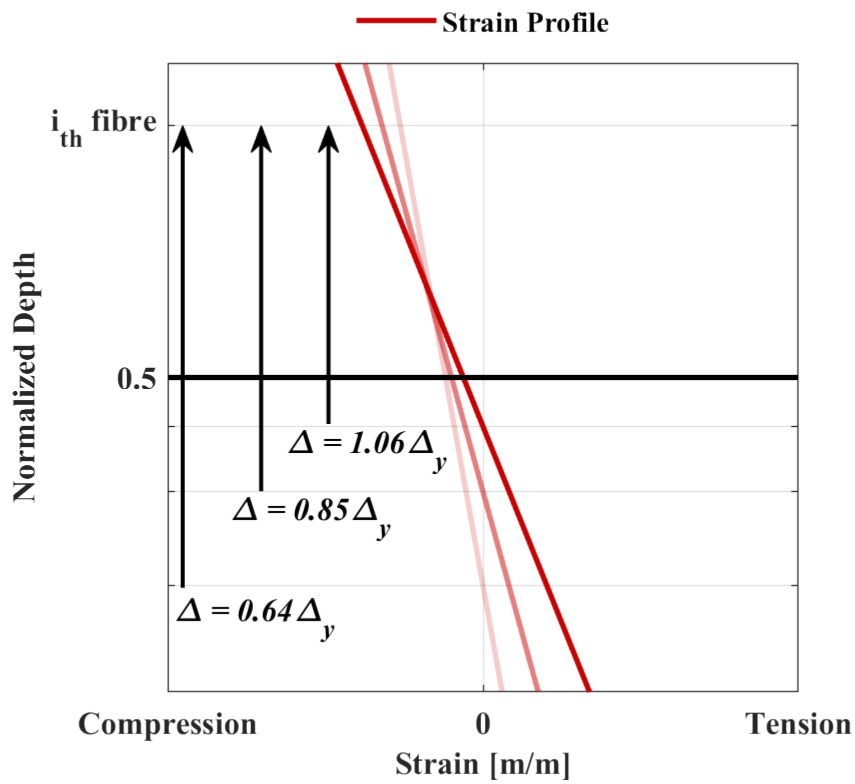

Figure 5.2 Distance variation from a specific fibre to the neutral axis over time.

Nevertheless, the y distance can be calculated by similar triangles since the vertical length from the mid-depth fibre to any other fibre along the member depth is known, as well as their corresponding strain values. This approach is illustrated in Figure 5.3. for two cases: 1) one where the mid-depth fibre is in compression; and 2) one where the mid-depth fibre is in tension.

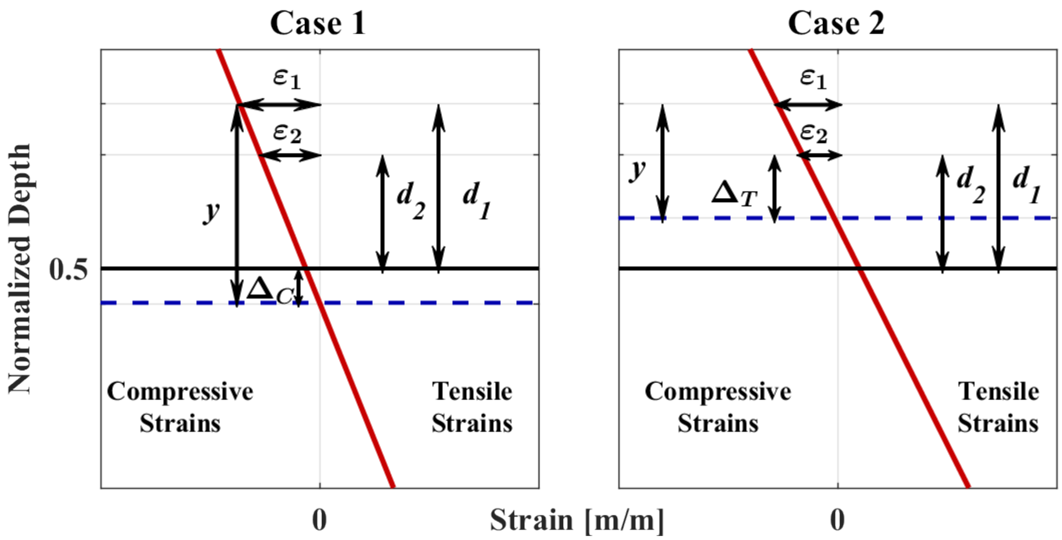

Figure 5.3 Geometrical relationships to compute y.

In Figure 5.3, d_1 and d_2 are the distances from the mid-depth fibre to other two fibres, fibre 1 and fibre 2, respectively. ε_1 and ε_2 are the observed strains at fibres 1 and 2, respectively. Δ_C and Δ_T are the missing distances to solve for y based on similar triangles as follows. For Case 1, when the mid-depth fibre is in compression, the value of Δ_C is first required to solve for y. The geometrical relationship of Equation (5.2) was developed to find its value.

$$\frac{\Delta_C + d_2}{\varepsilon_2} = \frac{\Delta_C + d_1}{\varepsilon_1} \tag{5.2}$$

Solving Equation (5.2) for Δ_C yields Equation (5.3).

$$\Delta_C = \frac{\varepsilon_2 d_1 - \varepsilon_1 d_2}{\varepsilon_1 - \varepsilon_2} \tag{5.3}$$

Next, the similar triangles relationship required to obtain y is expressed in Equation (5.4).

$$\frac{y}{\varepsilon_1} = \frac{\Delta_C + d_2}{\varepsilon_2} \tag{5.4}$$

The Δ_C value of Equation (5.3) is substituted in Equation (5.4) and y can be expressed in terms of known variables. Equation (5.5) is the expression used to obtain the distance from the neutral axis to fibre 1 at every time step when the mid-depth fibre is in compression.

$$y = \frac{\varepsilon_1 \left(d_1 - d_2\right)}{\varepsilon_1 - \varepsilon_2} \tag{5.5}$$

For Case 2, when the mid-depth fibre is in tension, Equations (5.6) and (5.7) were used to obtain the y value in terms of known variables.

$$\Delta_T = y - d_1 + d_2 \tag{5.6}$$

$$\frac{y}{\varepsilon_1} = \frac{\Delta_T}{\varepsilon_2} \tag{5.7}$$

By substituting (5.6) into (5.7) the expression for y when the mid-depth fibre experiences tensile strain is obtained. The resulting equation is the same as in Case 1, see Equation (5.5). Now it is possible to obtain the curvature at every time step by replacing the distance from the neutral axis to fibre 1 from Equation (5.5) into Equation (5.2) together with ε_1. The method defined in this section is used to obtain the full moment-curvature plot of the GFRS members, as illustrated in Figure 5.4.

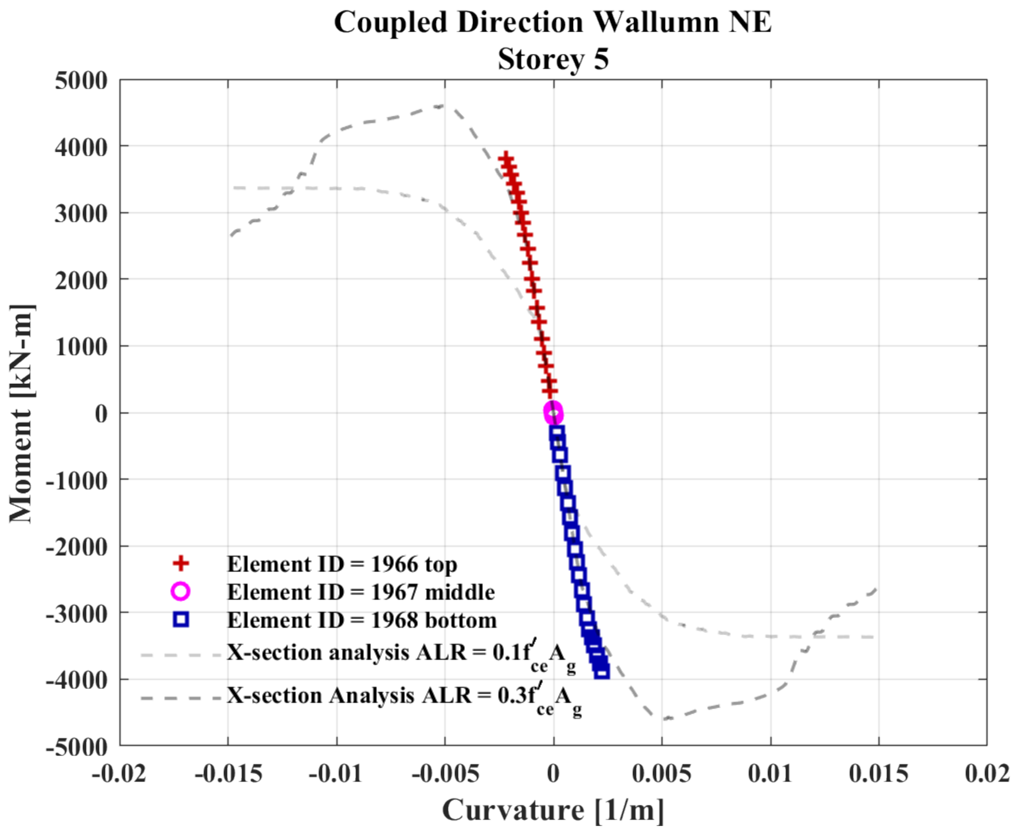

Figure 5.4 Full moment-curvature plot from the pushover analysis of a wallumn in the coupled direction.

To ensure the moment-curvature of GFRS components was computed using the method previously described, a simple exercise was carried out to ensure the results were independent of the fibres chosen to carry out the calculations (i.e., to ensure any two fibers would yield consistent moment-curvature results).

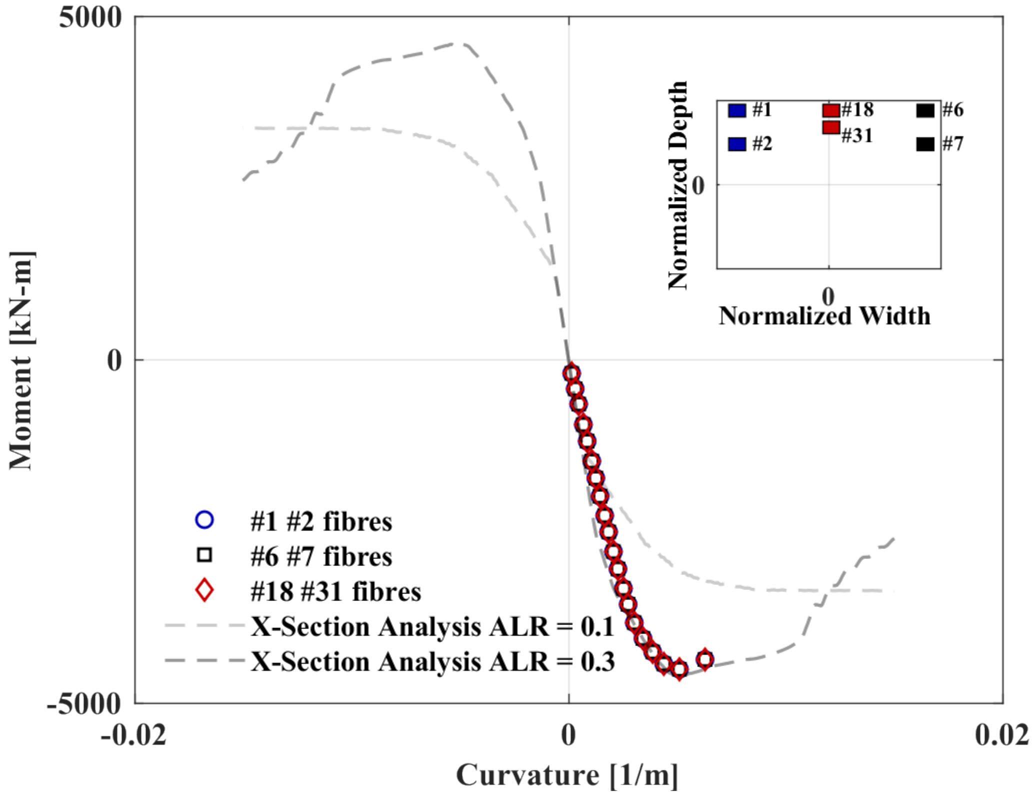

Figure 5.5 Moment-curvature of a GFRS component using three different set of fibres to obtain the curvature.

Figure 5.5 validates the methodology introduced in Section 5.1.1 to calculate the curvature. Using three different sets of fibres, Equation (5.5) yields the same curvature regardless the fibres' position or corresponding material. Fibres 1, 2, 6, 7, and 18 are unconfined concrete fibres. Fibre 31 is a confined concrete fibre. The curvature of the GFRS component can be computed as long as the strain of two different fibres throughout the depth of the cross-section is known.

5.1.2 GFRS Secant Stiffness from the Moment-Curvature Plots

From the moment-curvature relation, the Secant Stiffness (Paulay, 2001) at the end of the analysis is calculated in order to establish the flexural effective stiffness, EI_{eff}, for GFRS elements. The

Secant Stiffness of an element is the relationship between the observed demands and deformation. For this study, EI_{eff} was obtained by dividing the last observed moment demand over its corresponding curvature. For instance, the flexural effetive stiffness of the top, middle, and bottom portions of the GFRS column shown in Figure 5.4 is displayed in Figure 5.6. In this example, the column experiences double curvature with almost no seismic demands observed at mid-height.

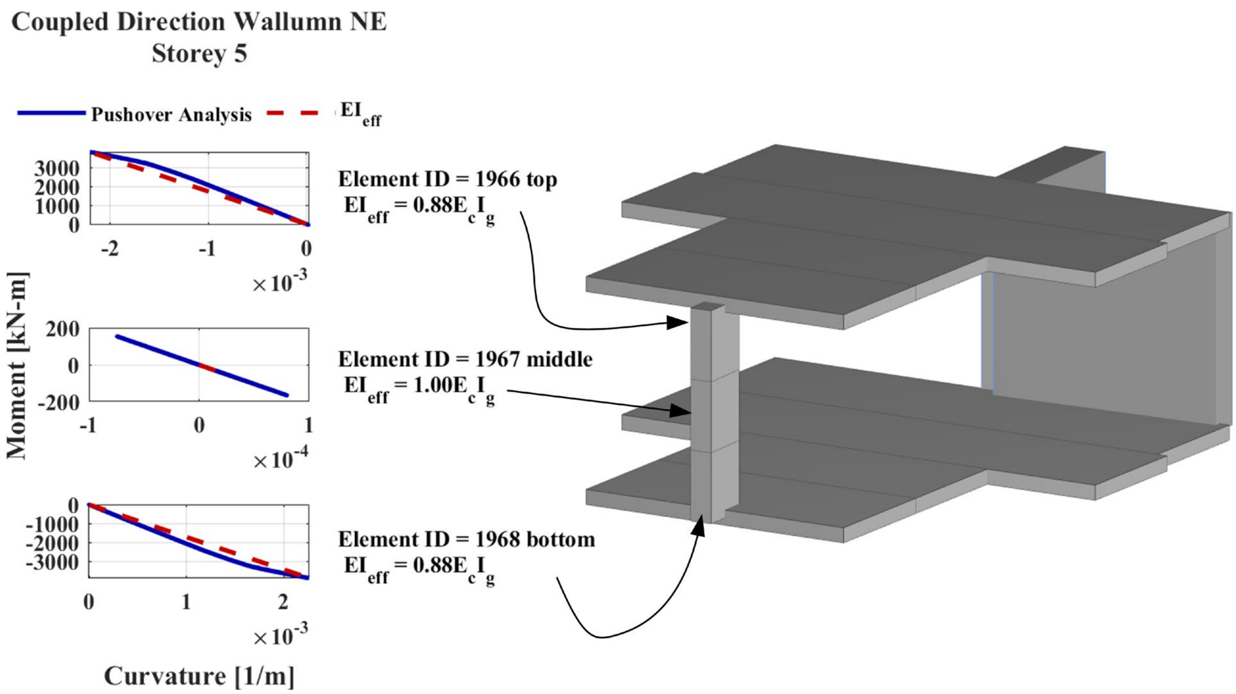

Figure 5.6 Effective flexural stiffness of a wallumn element.

For practical purposes, it is not efficient to assign a flexural effective stiffness value to each linear-elastic column throughout the storey height. Industry practice allocates a single flexural effective stiffness factor for the column element at the corresponding story. Therefore, the weighted average value of the three beam-column elements of each storey was computed for use in the linear-elastic analysis model. The columns could bend in single or double curvature as explained in Section 2.6.

This results in a different cracking level depending on the observed curvature. For instance, the bottom portion of the column will experience the largest cracking if it bends in single curvature. In contrast, the bottom and top portions of the column will observe the largest cracking if it bends in double curvature. Thus, this average value yields a good estimate of the column's cracking (Paulay & Priestley, 1992) throughout its length. In contrast with the approach followed to determine the flexural effective stiffness of the columns, the effective stiffness value used in the linear-elastic EBW slabs was retrieved from the beam-column element connecting the wallumn or core. This approach was considered since the cross-section of the EBW components connecting the wallumn is different from those connecting the core.

5.2 Effective Stiffness Calibration in the Linear-Elastic Model

The flexural effective stiffness modifiers estimated for the different components of the GFRS, obtained as described in Section 5.1.2, were adopted in the linear-elastic model. Upon subjecting the linear-elastic analysis model to the prescribed drift profile, described earlier in Section 4.1, it was observed that the bending demands in some GFRS elements differed from those in the nonlinear model. In order to obtain better agreement, the original EI_{eff} values were calibrated through an iterative process described in Equation (5.8).

$$EI^{i}_{eff} = \frac{M_{NL}}{M^{i-1}_{LE}} EI^{i-1}_{eff} \tag{5.8}$$

Where for each element, the flexural effective stiffness at iteration i, EI^{i}_{eff}, is equal to the bending moment demand obtained from the nonlinear model, M_{NL}, divided by the bending moment demand obtained from the linear-elastic model in the previous iteration, M^{i-1}_{LE}, multiplied by the flexural effective stiffness from the previous iteration, EI^{i-1}_{eff}. This calibration was carried out for all the GFRS components regardless of the initial degree of convergence. It was observed that for GFRS elements that showed an initial good agreement in the first iteration, this calibration did not significantly alter the effective flexural stiffness value, primarily because the M_{NL}/M^{i-1}_{LE} ratio remained close to 1.0 throughout the calibration. The overall calibration routine ceased when either 1) most of the elements reached good agreement, i.e., the M_{NL}/M^{i-1}_{LE} ratio is within ±10% of 1.0 or 2) the linear-elastic bending moment demands converged, even if the M_{NL}/M^{i-1}_{LE} ratio was not close to 1.0, which usually occurred around the tenth iteration.

Generally, the bending demands in the EBW elements within the linear-elastic model reached good agreement against their nonlinear twins around the fourth iteration. For the square columns and wallumns, the demands converged around the tenth iteration. While results were not always identical on an element by element basis, they showed better agreement than in the first iteration. One of the reasons why the moment demands in the columns of the linear-elastic model could not closely match those of the nonlinear model at certain locations is attributed to the project constraint of developing a single flexural effective stiffness modifier for each column type. The columns in the nonlinear model consist of three beam-column elements per storey. In principle, this would translate to three different flexural effective stiffness modifiers per storey in the linear-elastic model. However, the calibration intends to derive a single flexural stiffness modifier per story, as typically done in practice, resulting in discrepancies at some building locations.

5.3 Nonlinear vs Linear-Elastic GFRS Moment Demands

The results of the calibration exercise described in Section 5.2, are summarized here in both the cantilevered and coupled building directions. Referring back to Figure 3.1, the building layout is symmetrical. This permitted grouping GFRS components according to their experienced demands and behaviour. The columns were grouped in three categories: square columns, "tension" wallumns, and "compression" wallumns. Because the square corner columns are not in the SFRS plane, they are non-outrigger columns and behave in a similar fashion. On the other hand, the wallumns, which are in the SFRS plane, are outrigger elements due to the framing action with the central core. The wallumns experienced different axial forces depending on their position in the floorplan. The wallumns that were in the "tension" side experienced less axial force, although the net axial load was always compressive. The "compression" wallumns experienced larger axial compressive demands. The EBWs were classified according to the connection type, i.e. connection to a wallumn or to the core, and based on whether they were positioned in the "tension" or "compression" side of the analysis. Figure 5.7 shows a diagram of the GFRS elements located in the "tension" or "compression" side for the (a) cantilevered and (b) coupled pushover analyses.

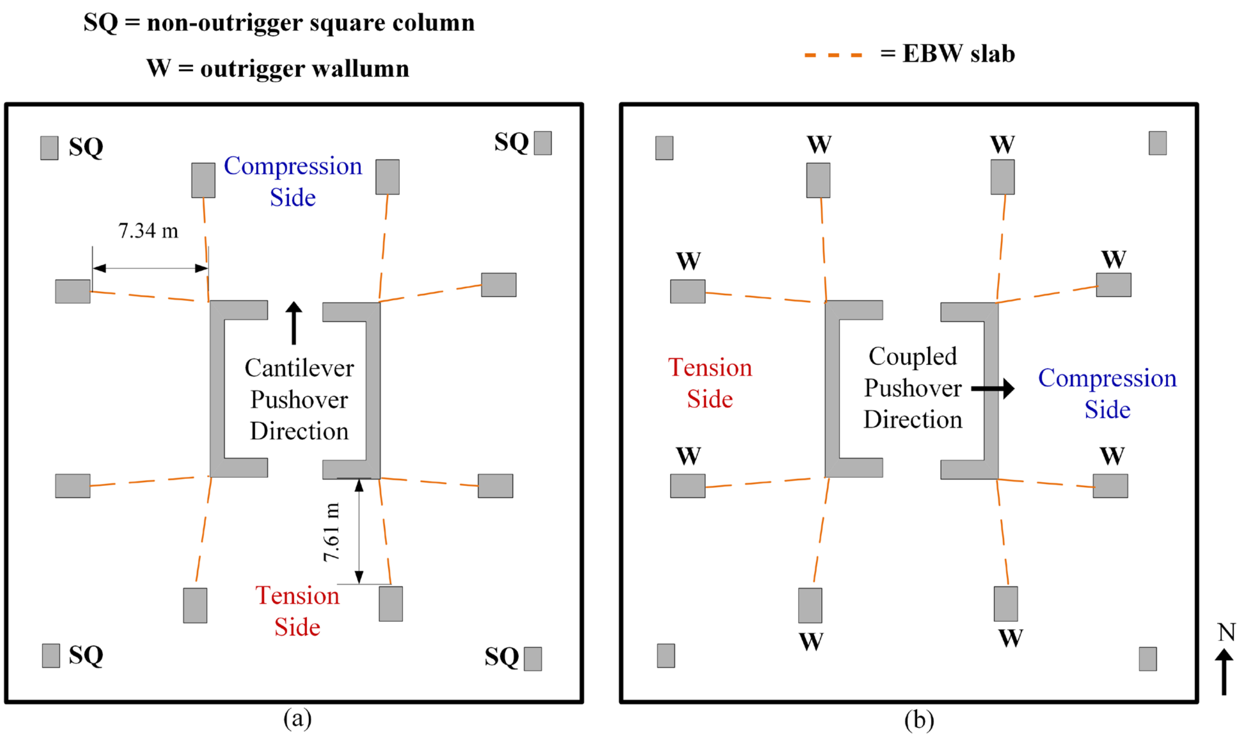

Figure 5.7 "Tension" and "Compression" sides for each direction during the pushover static analyses; (a) cantilevered direction; (b) coupled direction.

Cantilevered Direction

Figure 5.8 compares the linear-elastic bending moment demands after the flexural effective stiffness modifiers calibration was performed against the nonlinear demands of columns in the cantilevered direction. Three main observations could be pointed out, 1) the demands in the linear-elastic model and the nonlinear model columns are in good agreement in the top two thirds of the building's height; 2) the linear-elastic model tends to overestimate the demands at the base of columns in the cantilever direction; and 3) the large demands observed in levels 7-10 in the nonlinear models, where these elements experience considerable nonlinear behaviour, could not be replicated in the linear-elastic models. The peaks in bending moment demand, which are observed at around one third of the building height, regardless the column type, are attributed to the drift profile. A more detailed discussion on the effect of the drift profile in the column demands is provided in Appendix A .

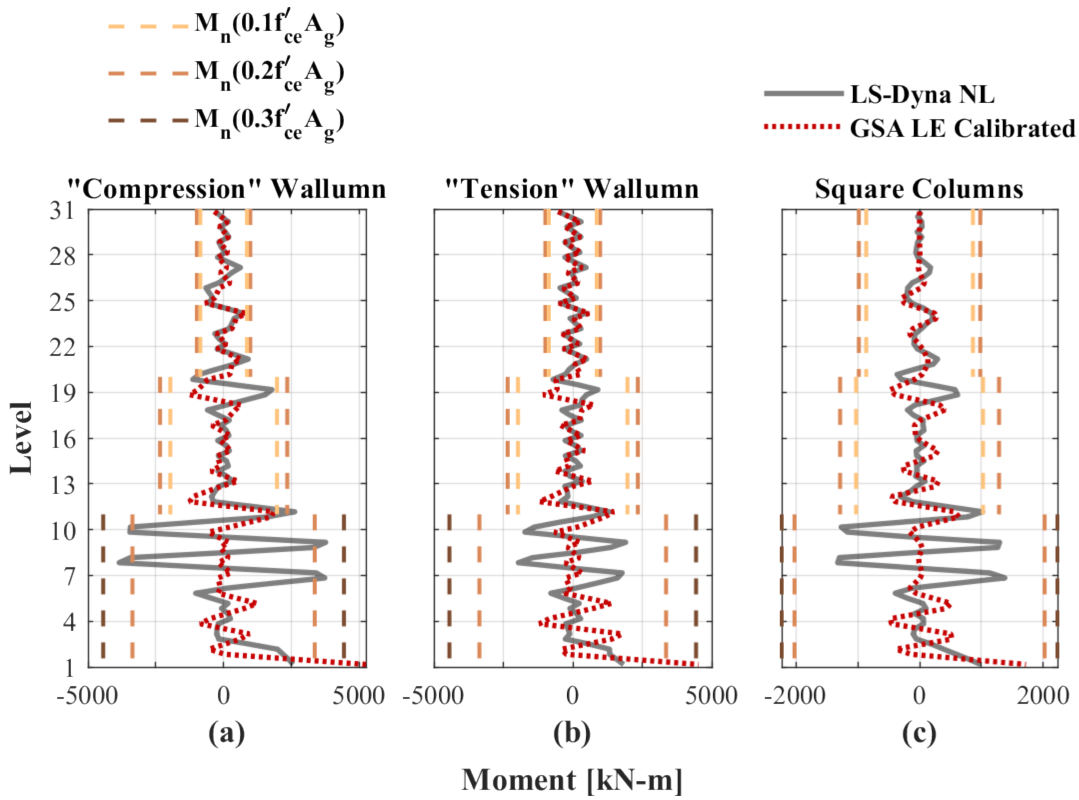

Figure 5.8 Linear-elastic vs nonlinear bending moment demands comparison for columns in the cantilevered direction: (a) “compression” wallumn; (b) “tension” wallumn; (c) square columns.

As observed in Figure 5.9, the EBW demands in the linear-elastic model and the nonlinear model columns are in good agreement. Even though the intent by design is for EBW slabs to yield (to replicate strong-column weak-beam type behaviour), this was not observed primarily due to the induced compressive forces, caused by axial elongation (refer back to Section 4.3.5) and the associated increased in the elements capacity, which typically doubled.

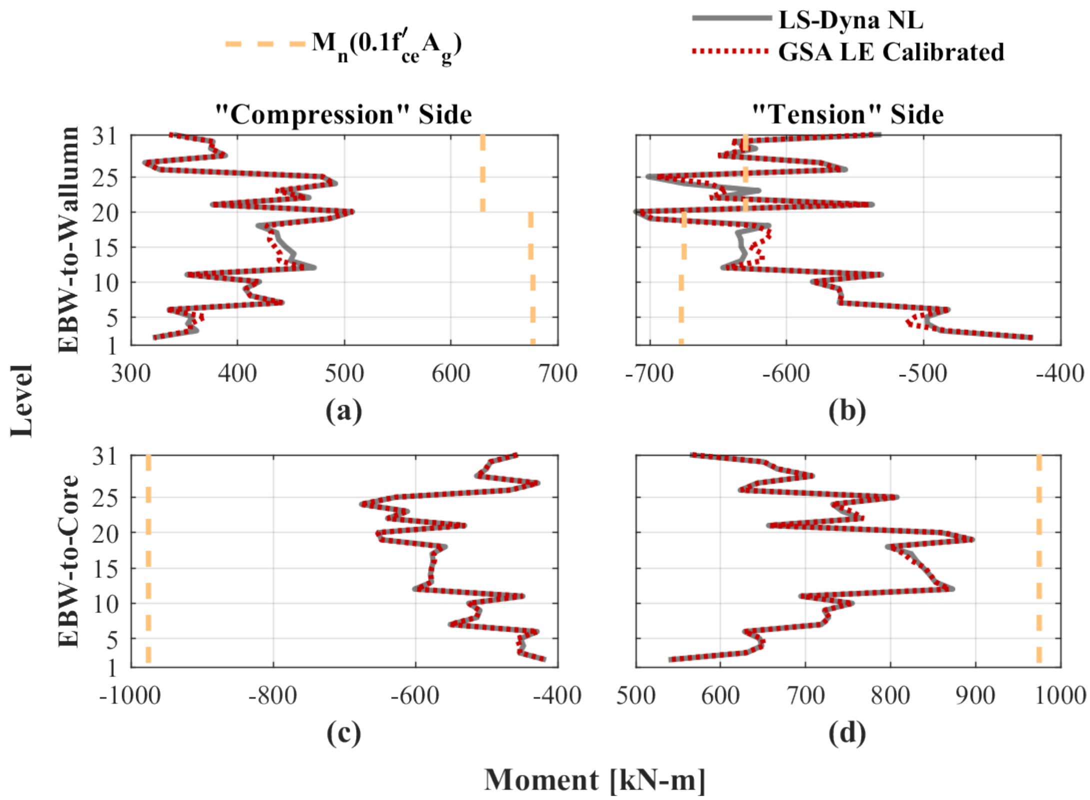

Figure 5.9 Linear-elastic vs nonlinear bending moment demands comparison for EBW slabs in the cantilevered direction: (a) EBW-to-wallumn "compression" side; (b) EBW-to-wallumn "tension" side; (c) EBW-to-core "compression" side; (d) EBW-to-core "tension" side.

Coupled Direction

The linear-elastic column demands in the coupled direction follow the nonlinear moment demands with great accuracy. As observed in Figure 5.10, there is a pattern in the demands for all column types. As with the columns in the cantilever direction, this is attributed to the drift profile as described in more detail in Appendix A .

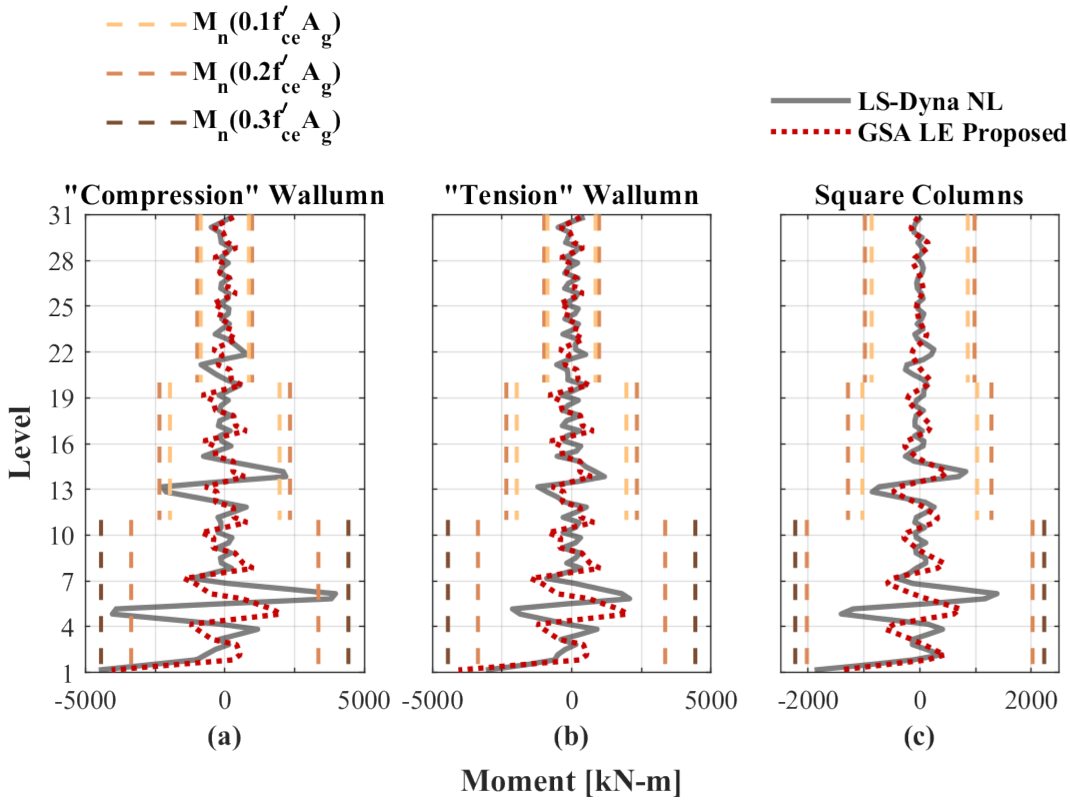

Figure 5.10 Linear-elastic vs nonlinear bending moment demands comparison for columns in the coupled direction: (a) "compression" wallumn; (b) "tension" wallumn; (c) square columns.

The linear-elastic EBW slabs in the coupled direction were also capable to match the nonlinear demands with good accuracy, as observed in Figure 5.11.

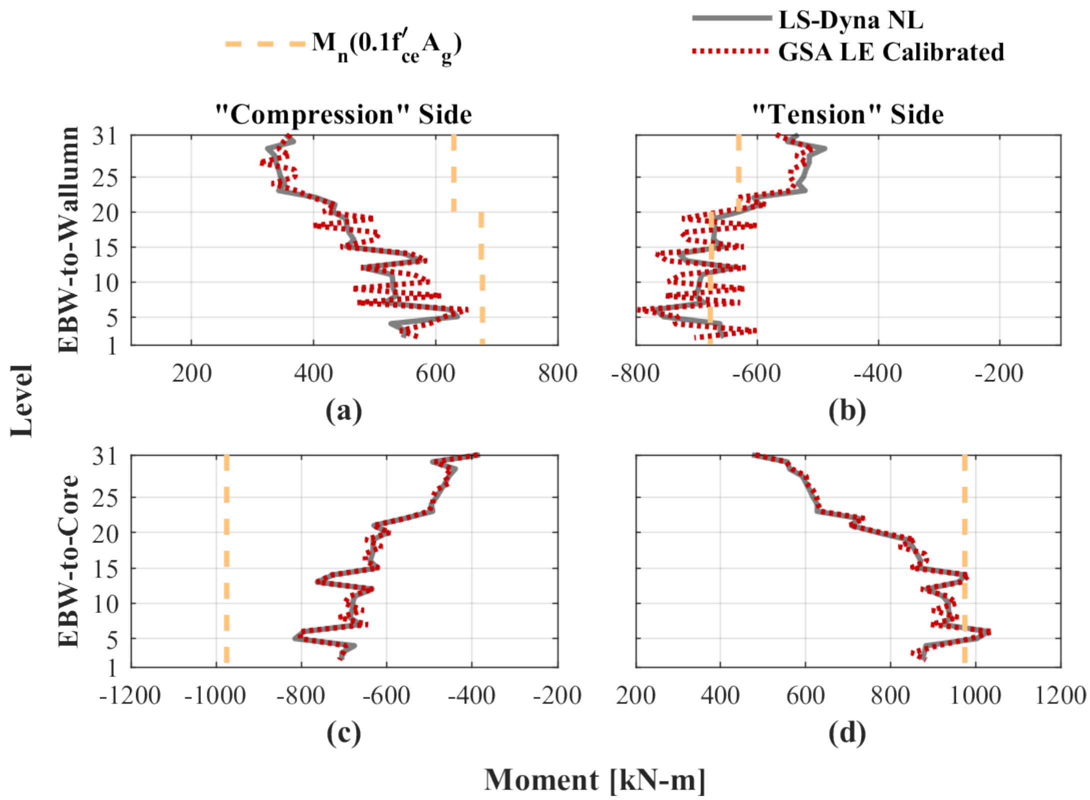

Figure 5.11 Linear-elastic vs nonlinear bending moment demands comparison for EBW slabs in the coupled direction: (a) EBW-to-wallumn "compression" side; (b) EBW-to-wallumn "tension" side; (c) EBW-to-core "compression" side; (d) EBW-to-core "tension" side.

5.4 Summary of Flexural Stiffness Factors for the GFRS members

This section summarizes the flexural stiffness modifiers associated with the demands previously report in Section 5.2. Namely, the modifiers based on the results presented in Figure 5.8, Figure 5.9, Figure 5.10, and Figure 5.11. The plan view of Figure 5.7 shows there are 12 columns in the gravity-frame, each of them has three-beam column elements per storey, and the weighted average value of the three beam-column elements of each storey was computed for use in the linear-elastic analysis model. This results in 30 flexural stiffness modifiers for each gravity-column. There is also one EBW slab at each level per connection type which results in 30 different flexural effective stiffness modifiers for each EBW slab. These results will be used later in Chapter 6 to develop prediction equations to compute flexural effective stiffness factors for GFRS members with different geometric properties. Figure 5.12 and Figure 5.13 show the flexural effective stiffness values for the GFRS members in the cantilevered direction. The flexural effective stiffness values for the columns and EBW slabs in the coupled direction are presented in Figure 5.14 and Figure 5.15, respectively.

Cantilevered Direction

The compression outrigger wallumn in Figure 5.12(a) presents a range of flexural effective stiffness modifiers from $0.09EI_g$ to $1.0EI_g$. Its average value is $0.56EI_g$. The minimum and maximum flexural stiffness modifiers for the cantilevered outrigger tension wallumn in Figure 5.12(b) are $0.06EI_g$ and $1.0EI_g$, respectively. The average flexural stiffness modifier is equal to $0.64EI_g$. The square columns minimum and maximum flexural stiffness modifier are $0.27EI_g$ and $1.0EI_g$, respectively (refer back to Figure 5.12(c)). The average flexural effective stiffness modifier in square columns is $0.71EI_g$. In general, all columns in the cantilevered direction presented smaller flexural effective stiffness modifiers at levels 4, 13, and 16. In contrast, their flexural effective stiffness modifiers remained equal or very close to EI_g at levels seven to nine.

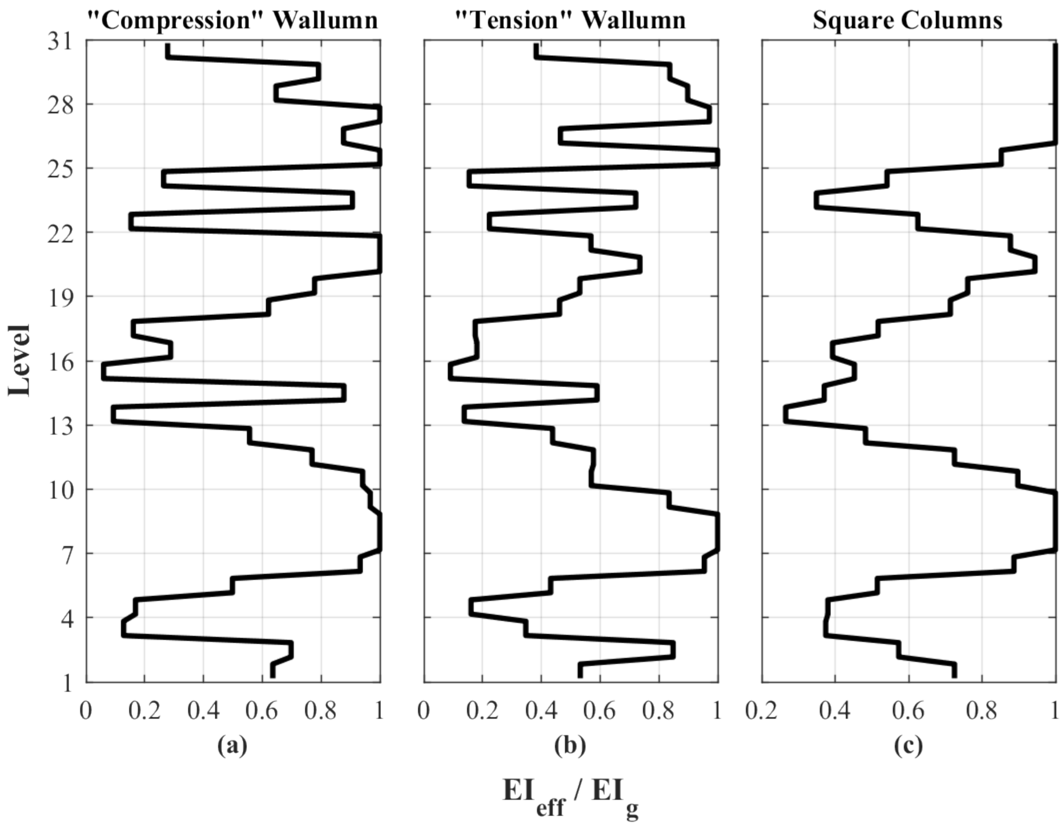

Figure 5.12 Calibrated effective stiffness values for columns in the cantilever direction; (a) “compression” wallumn; (b) “tension” wallumn; (c) square columns.

Figure 5.13(a) and (b) shows that the range of flexural effective stiffness modifiers for the EBW-to wallumn slabs are [0.24EI_g, 0.54EI_g] and [0.49EI_g, 0.62EI_g] for the “compression” and “tension” side, respectively. The average flexural effective stiffness modifier for the “compression” and “tension” EBW-to-wallumn slab is 0.40EI_g and 0.63EI_g, respectively. From Figure 5.13(c), the minimum and maximum flexural stiffness modifiers for the EBW-to-core slab in the “compression” side are 0.18EI_g and 0.64EI_g, respectively; its average value is 0.34EI_g. The “tension” EBW-to-core slab in Figure 5.13(d) shows that the minimum and maximum flexural effective stiffness modifiers are 0.30EI_g and 0.85EI_g, respectively; the average flexural effective stiffness modifier for this member is $0.50EI_g$. In average, the EBW-to-wallumn slabs present larger flexural stiffness modifiers compared to the core connection when they are position on the same side (i.e., "compression" or "tension" side).

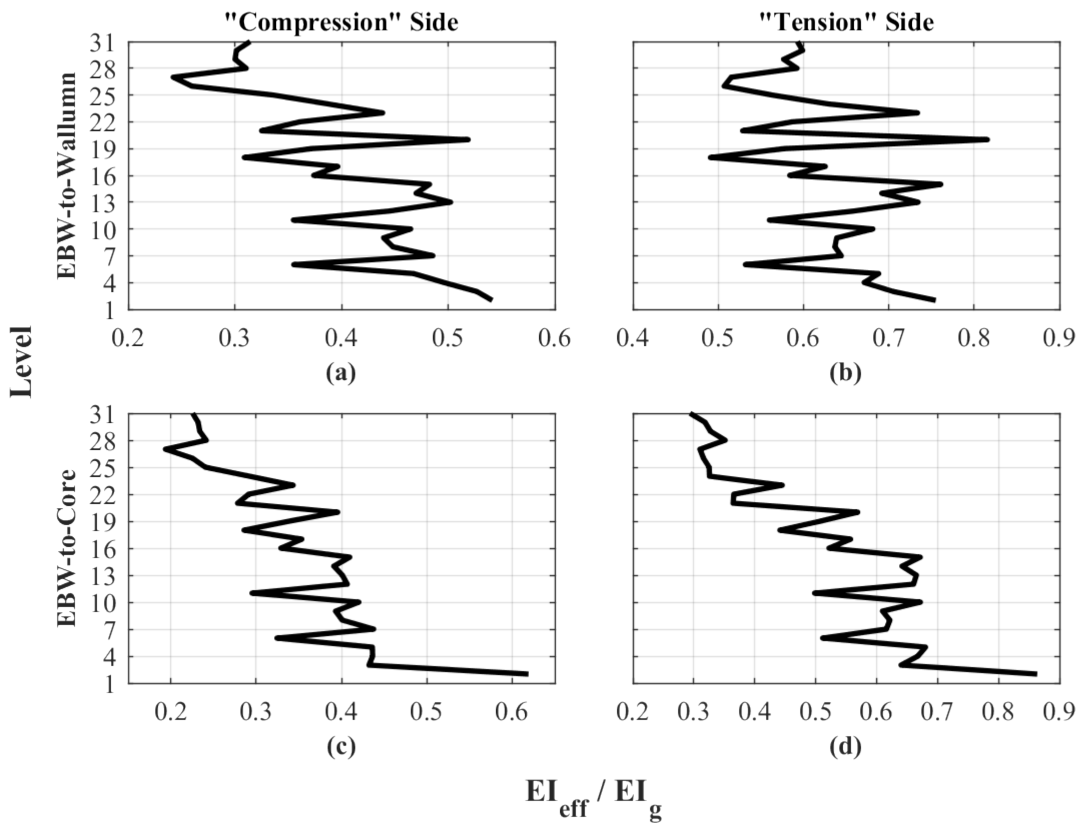

Figure 5.13 Calibrated effective stiffness values for EBW slabs in the cantilever direction; (a) EBW-to-wallumn "compression" side; (b) EBW-to-wallumn "tension" side; (c) EBW-to-core "compression" side; (d) EBW-to-core "tension" side.

Coupled Direction

Figure 5.14 shows that the flexural effective stiffness factors range for the (a) “compression” wallumn, (b) “tension” wallumn, and (c) square columns are [0.03EI_g, 1.0EI_g], [0.06EI_g, 1.0EI_g], and [0.13EI_g, 1.0EI_g], respectively. Their average flexural stiffness modifier is 0.37EI_g, 0.42EI_g, and 0.53EI_g, respectively. For all three column types, level 13 flexural stiffness is equal to the gross stiffness and the smaller flexural effective stiffness values are observed at grade, levels eight to nine, and 17 to 18.

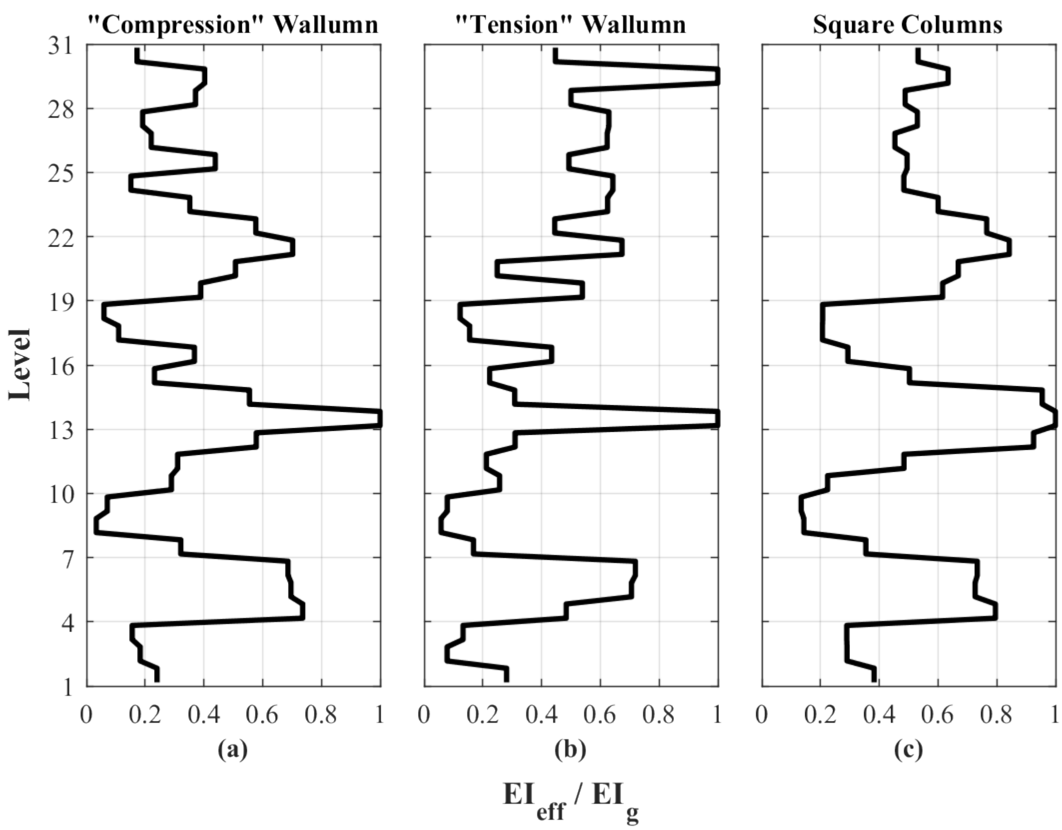

Figure 5.14 Calibrated effective stiffness values for columns in the coupled direction; (a) “compression” wallumn; (b) “tension” wallumn; (c) square columns.

Figure 5.15 shows that the flexural effective stiffness modifiers range for the (a) "compression" EBW-to-wallumn, (b) "tension" EBW-to-wallumn, (c) "compression" EBW-to-core, and (d) "tension" EBW-to-core members are [$0.30EI_g$, $0.56EI_g$], [$0.49EI_g$, $0.80EI_g$], [$0.20EI_g$, $0.54EI_g$], and [$0.25EI_g$, $0.76I_g$] respectively. Their average flexural effective stiffness modifier is $0.40EI_g$, $0.59EI_g$, $0.35EI_g$, and $0.50EI_g$, respectively. In average, the EBW-to-wallumn slabs present larger flexural effective stiffness modifiers compared to the core connection when they are positioned on the same side (i.e., "compression" or "tension" side).

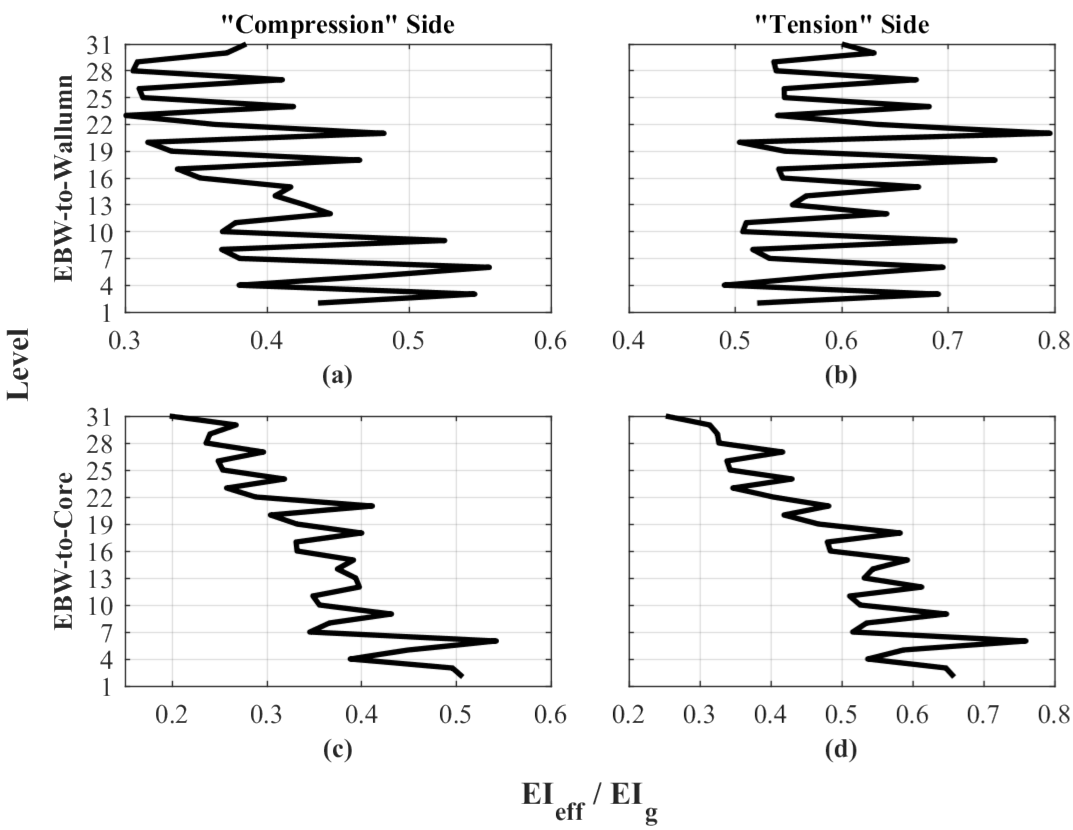

Figure 5.15 Calibrated effective stiffness values for EBW slabs in the coupled direction; (a) EBW-to-wallumn "compression" side; (b) EBW-to-wallumn "tension" side; (c) EBW-to-core "compression" side; (d) EBW-to-core "tension" side.

Chapter 6: GFRS Flexural Effective Stiffness Modifiers Prediction Equations

This chapter presents the development of empirical prediction equations to estimate appropriate flexural effective stiffness modifiers for elements of the GFRS for use in the General or Simplified Analysis procedures outlined in § 21.11.2.1 and § 21.11.2.2 of CSA A23.3-19. The relationships were formulated following a multivariate regression analysis with the data obtained in Chapter 5. The predictor equations are a function of geometric and material properties.

Section 6.1 states the applicability and limitations of the proposed equations. Section 6.2 introduces the statistical procedure to obtain the prediction equations. Sections 6.3 and 6.4 present the predictions equations for the GFRS components in the cantilevered and coupled directions, respectively. The equations developed for the cantilevered and coupled direction are not the same. This is because 1) the drift profile applied to each direction is different and 2) the interaction between a cantilever wall and a gravity-frame is different from a coupled wall and gravity-frame. The recommendations developed in this chapter will be tested and analyzed in Chapter 7.

6.1 Applicability and Limitations

The flexural effective stiffness predictor equations, hereinafter referred to as the *Proposed Equations*, are intended for use when adopting the General Analysis or Simplified Analysis in § 21.11.2.1 and § 21.11.2.2 of CSA A23.3-19 for the design of the GFRS in RCSW buildings consistent with the archetype presented in this study. Each equation is applicable to a specific component type regardless of whether it is positioned in the “tension” or “compression” side.

The equations presented in this chapter allow the structural engineer to compute the flexural effective stiffness factors of each GFRS component throughout the height of the building based on set of predictor variables that are readily available. For columns, this will result in a different flexural effective stiffness factor at each storey. For EBW slabs, the flexural effective stiffness modifier will change at each level. If, for practical purposes, the practicing engineer prefers to apply a single value to each GFRS component type throughout the entire building, as opposed to assigning individual stiffness modifiers to each element, a conservative solution would be to assign the largest flexural stiffness modifier to all GFRS components with the same cross-section layout. For example, if the building has 30 storeys and the cross-section layout of the columns changes every ten storeys the first step would be to obtain the thirty effective stiffness modifiers (one per storey). Next, the largest flexural effective stiffness modifier of each cross-section layout group is selected, resulting in three flexural effective stiffness modifier categories, one for every ten storeys. Finally, each upper-bound flexural effective stiffness factor will be assigned to the columns that share the same cross-section layout (one for the bottom ten storeys, one for the middle ten and one for the top ten).

The limitations are the following:

- The recommendations are based in a single SFRS and GFRS design. As a result, the *Proposed Equations* may not return appropriate flexural effective stiffness modifiers for other building configurations. Different sizes of columns and slabs should be evaluated to increase the range of validity of the regression models. The effect of distance from the outrigger wallumns to the core also needs to be assessed. Multiple building configurations with different RCSW cross-section dimensions should be explored. As future studies explore the effects of varying cross section and building geometry, the proposed equations can be expanded. to other buildings

.

- The EBW slabs *Proposed Equations* are not meant for transfer or post-tensioned slabs.
- Foundation movement was not accounted for when computing the drift profile. Because of this, the *Proposed Equations* are valid for building where the foundation movement is small or could be neglected.
- The flexural effective stiffness modifiers for the EBW slabs should be applied to one-dimensional beam elements and not to two-dimensional linear-elastic shell elements.

6.2 Statistical Methods

To develop the regression model, the flexural effective stiffness modifiers estimated in Chapter 5 were grouped according to their component type. This enabled the development of equations for outrigger wallumns, non-outrigger square columns, and EBW slabs in both the cantilevered and the coupled directions. The symmetrical building layout allowed the columns and EBW slabs to be grouped according to their experienced demands and behaviour. Because of this, the outrigger wallumn data set was composed of 60 flexural stiffness modifiers, 30 of them extracted from the "compression" wallumns and the other 30 from the "tension" wallumns. All the non-outrigger square columns behaved similarly, therefore, this GFRS group was composed of 30 data points. Last, the EBW slabs data set had a total of 120 effective stiffness values, 30 from each connection type, i.e., "compression" EBW-to-wallumn, "tension" EBW-to-wallumn, "compression EBW-to-core, and "tension" EBW-to-core. The earthquake inertial forces exert a load reversal at each GFRS member. Because of this, it is not practical to assign a different value for the "compression" and “tension” members of the building model for design purposes. Thus, the “compression” and “tension” flexural stiffness modifiers of the same GFRS members are lumped into the same regression model, with the intention to obtain a prediction equation that captures the general behaviour of both sides.

Once the data was gathered into corresponding groups, predictors variables were selected based on their capability to estimate the flexural stiffness modifiers. These variables were chosen based on 1) the accessibility of the data, i.e., design variables known to the structural designer such as material and geometric properties, 2) first principles, e.g., concrete cracking is affected by the level of demands and axial load, and 3) past research aimed at developing stiffness modifiers for other structural components.

All the selected variables were dimensionless for consistency with the EI_{eff}/EI_g ratio. Once the data and the predictor variables were defined, an appropriate form for each equation was established. A detailed review of the data scatter plots and the shape of the bending moment demands throughout the building height were crucial to determine a suitable regression model for each GFRS component.

Standard multiple linear and nonlinear regression analyses were performed in MATLAB (2021). The Stepwise approach (Chatterjee & Hadi, 2006) was used to ensure only statistically significant variables at a 95% level were used in the predictive equations. In general, this approach enabled the inclusion of a new variable at each stage if its p-value is less than 0.05, as well as delete another variable if it was not significant at a 95% level. A predictor that was significant at an earlier stage could be removed from the regression model at a later stage. In the development of the *Proposed Equations* the process was to explore a minimum of six to ten variables to understand their prediction power. Consequently, the predictor variables were narrowed down to the handful of variables that were significant and allowed the development of an appropriate prediction equation.

As commonly done in the literature (Lignos & Krawinkler, 2011; Sadeghian & Fam, 2015), the prediction power of linear and nonlinear equations proposed was evaluated using the coefficient of determination (R^2) and the Root Mean Squared Error (RMSE). R^2 is a measure of the linear correlation between the predicted and observed values whereas RMSE indicates how distanced the predicted values are from the experimental values. Moreover, a 45-degree line plot of observed vs predicted values is presented as this visual illustration represents how effective the model is in making estimations (Devore, 2011). In the context of this study, RMSE and the 45-degree line plot are considered the best indices to assess the prediction capability of the proposed equations. Because R^2 measures the goodness of fit along a straight line, for nonlinear regression models, this metric can yield misleading values that might not reflect the true prediction power of the proposed equations. As noted by Sadeghian & Fam (2015), in the hypothetical poor prediction case of observing the predicted vs experimental values laying along a 10-degree line, R^2 will report values close to 1.0, whereas RMSE will be able to show the flaws of the regression model. Furthermore, RMSE and the 45-degree line plot are related. The closer the data points are to the 45-degree line, the closer the RMSE values are to zero. Devore (2011) suggests also to plot the standardized residuals against the predicted values to assess the validity of the model. The scatter plot of the standardized residuals should have a random distribution and 95% of the data points should fall within two standard deviations.

6.3 Cantilever Direction Prediction Equations

6.3.1 Outrigger Wallumns

The selected variables to formulate the prediction equation for outrigger wallumns in the cantilever direction are:

- ***a/d*** = shear span-to-wallumn depth ratio.
- ***d/b*** = depth-to-width ratio.
- ***ρ*** = longitudinal reinforcement ratio.
- f_{ye}/f'_{ce} = expected yield strength to expected unconfined concrete strength.
- $P/A_g f'_{ce}$ = axial load ratio, factored gravity loads divided by the product of the gross area and expected unconfined concrete strength.
- ***δi*** = interstorey drift ratio.
- M_D = $M_n/f'_{ce}d^3$ = dimensionless nominal moment (Priestley, 2003). Nominal moment capacity accounting for factored gravity loads divided by the product of the expected unconfined concrete strength and the cubed depth.
- $u_i/u_{\max}$ = column displacement at the storey mid-height over the displacement at the roof. Both variables result from subjecting the building to the Simplified Analysis drift profile.
- ***d/t*** = wallumn depth-to-slab thickness.

Terms *a/d*, *d/b*, *ρ*, f'_{ye}/f'_{ce}, and *d/t* are geometric and material properties known to the structural designer after carrying out the gravity design for the for the GFRS. $P/A_g f'_{ce}$ accounts for the fact that the axial load ratio is inversely proportional to the level of concrete cracking. By contrast, *δi* and $u_i/u_{\max}$ are included based on the knowledge that larger demands will result in larger cracking of the RC component, hence lower stiffness modifiers. M_D was developed by Priestley (2003) to study the influence of axial load ratio in the capacity of bridge columns to formulate flexural effective stiffness modifiers. The scatter plot of the predictor variables mentioned above was plotted against the flexural effective stiffness modifiers presented in Chapter 5 to identify possible trends, as seen in Figure 6.1.

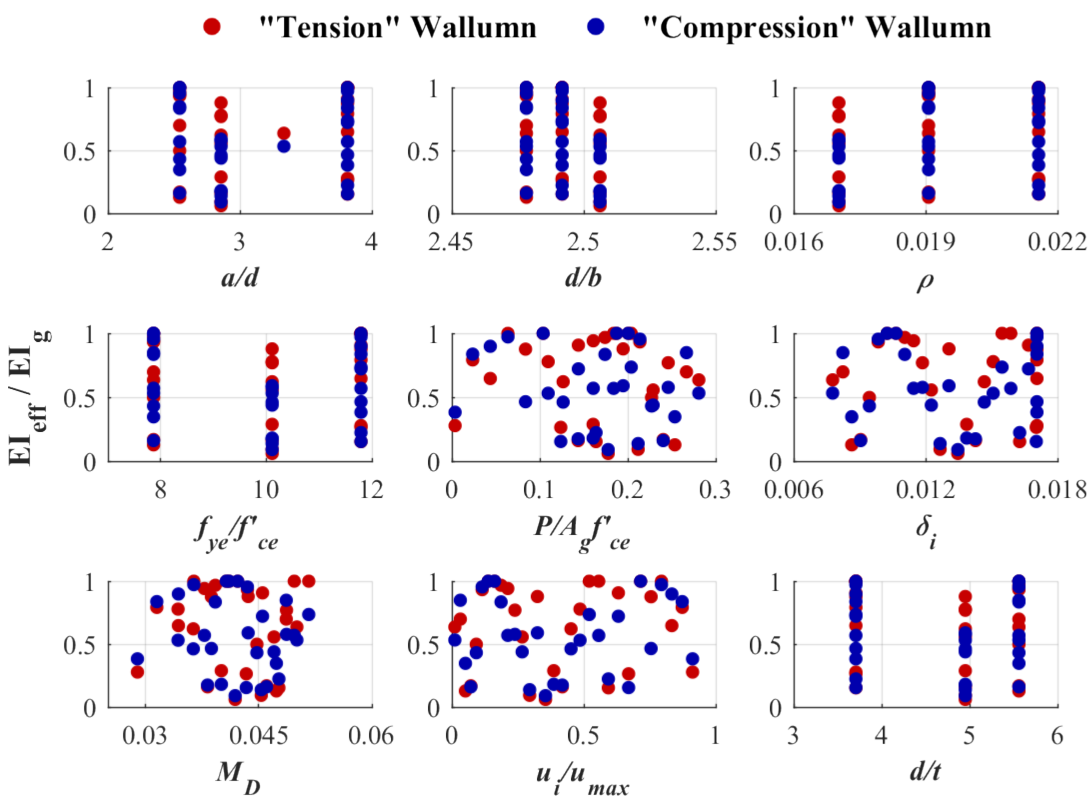

Figure 6.1 Scatter plot of the predictor variables used to develop the outrigger wallumn flexural effective stiffness predictor equation in the cantilever direction.

Out of the nine variables shown in Figure 6.1, the predictors that show a clearer trend are δi and $u_i/u_{\max}$. The pattern they present is close to a wave function. Referring back to plots (a) and (b) of Figure 5.8, the drift demands in the cantilevered direction exert and oscillatory moment demand pattern in the outrigger wallumns throughout the building's height. This shape could possibly be predicted using sine and cosine functions. With these inferences and the 60 data points of flexural stiffness modifiers obtained from Chapter 5, the proposed equation for outrigger wallumns in the cantilever direction is summarized below.

$$\frac{EI_{eff}}{EI_g} = 0.553 - 0.220\cos\left(4072M_D\right) - 0.387\sin\left(4072M_D\right)\cos\left(1005\delta_i\right) \leq 1.0 \tag{6.1}$$

$$R^2 = 0.522 \qquad \text{RMSE} = 0.228$$

Equation (6.1) presents two variables that directly relate to the cracking level of an RC member. M_D explicitly accounts for the cross-section dimensions, material properties, and capacity. δi considers the level of lateral displacement at the outrigger wallumn.

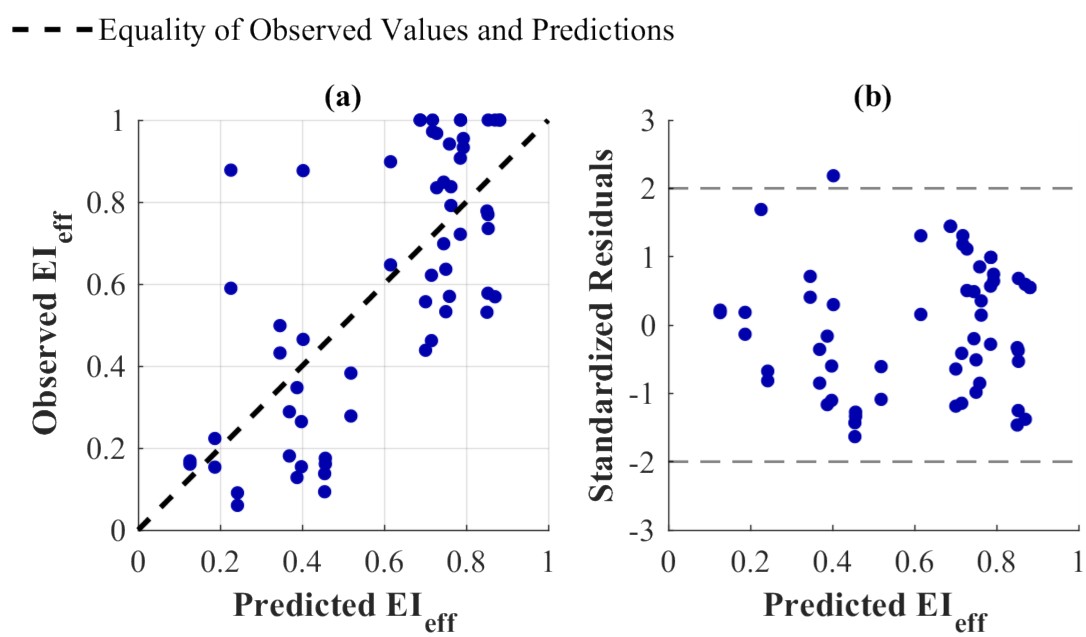

Figure 6.2 Regression model validation of Equation (6.1): (a) 45-degree line plot; (b) standardized residuals plot.

Plot (a) of Figure 6.2 shows that the predicted values of Equation (6.1) are in most cases consistent with the observed flexural effective stiffness modifiers. Plot (b) demonstrates a random distribution of errors and only one residual laying beyond the two standard deviations limit. It could be concluded that the model of Equation (6.1) is valid. The ranges of the parameters used in Equation (6.1) are:

- $0.0289 \leq M_D \leq 0.0516$
- $0.78\% \leq \delta i \leq 1.71\%$

6.3.2 Non-outrigger Square Columns

The variables used to formulate the prediction equation for this component are the same as in Section 6.3.1. The *d/t* predictor was omitted from the regression model because these components are not connected to the core through a EBW slab.

Figure 6.3 illustrates the scatter plot of the predictor variables for the non-outrigger square columns. As seen in the figure, the *d/b* variable does not provide any meaningful correlation, therefore, it is not considered in the regression model. Out of the other seven predictors, the variables that present an oscillatory pattern are $P/A_g f'_{ce}$, δi, M_D, and $u_i/u_{\max}$. δi shows the clearest wave pattern and M_D the most subtle. It is interesting to observe, based on the $u_i/u_{\max}$ plot, that the elements at the top of the non-outrigger square columns remain almost linear-elastic (i.e., $EI_{eff} = 1.0$). These are also the elements that experience the smallest axial load ratios. One of the possible reasons for this observation is the cantilever behaviour of these non-outrigger elements due to absence of framing action. A cantilever element will experience the least amount of demands at the unrestricted end, remaining linear elastic. The *d/b* variable remains constant for all square columns because their depth is equal to the width.

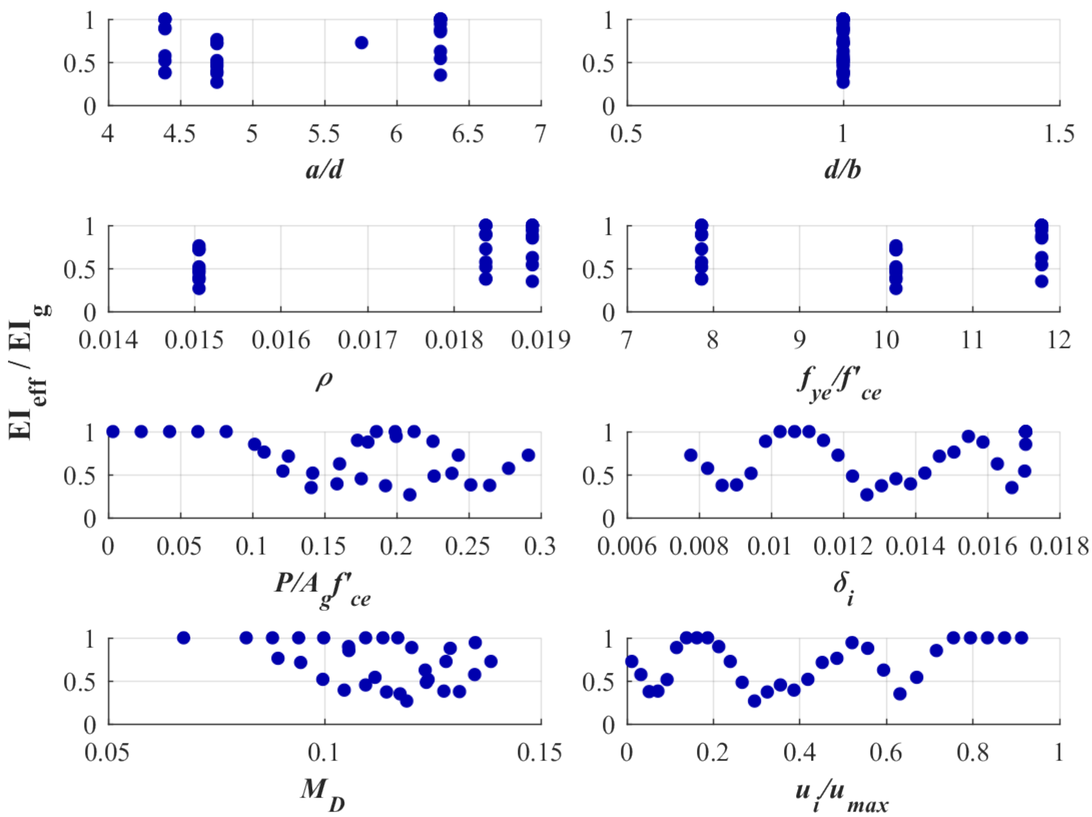

Figure 6.3 Scatter plot of the variables used to develop the non-outrigger square column flexural effective stiffness predictor equation in the cantilever direction.

As well as with the outrigger wallumns, the non-outrigger square columns also presented an oscillatory moment demand shape, refer back to plot (c) of Figure 5.8. This observation coupled with the 30 data points resulted in Equation (6.2) as a flexural effective stiffness predictor for non-outrigger square columns in the cantilevered direction.

$$\frac{EI_{eff}}{EI_g} = 0.668 + 0.364\cos\left(1164\delta_i\right) - 0.235\sin\left(1164\delta_i + 56.089\left(M_D\right)^{0.361}\right) \leq 1.0 \qquad (6.2)$$

$R^2 = 0.667$ RMSE = 0.161

$P/A_g f'_{ce}$ and $u_i/u_{\max}$ were not significant when assessing the regression model of Equation (6.2) because there is an existing correlation between the variables. $P/A_g f'_{ce}$ is implicitly accounted in M_D and $u_i/u_{\max}$ was computed from the interstorey drift ratio.

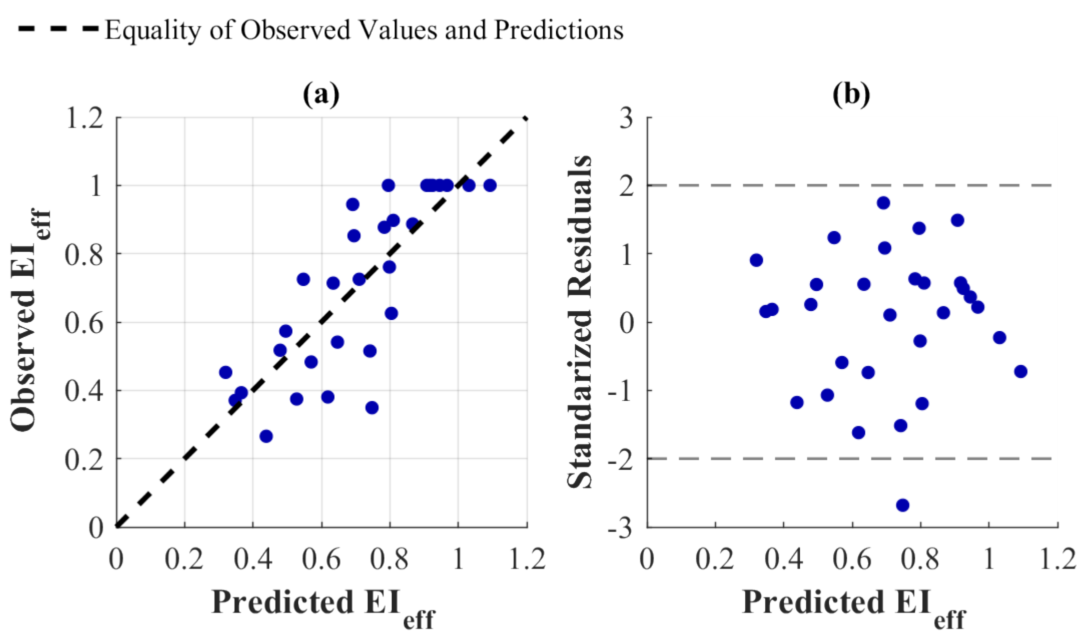

Figure 6.4 Regression model validation of Equation (6.2): (a) 45-degree line plot; (b) standardized residuals plot.

Figure 6.4 demonstrates a good agreement between predicted and observed values for the proposed equation for non-outrigger square columns in the coupled direction. No irregularities are observed in plot (b) of Figure 6.4. Therefore, the regression model is deemed as plausible. The ranges of the predictors used to develop Equation (6.2) are:

- $0.0674 \leq M_D \leq 0.1385$
- $0.78\% \leq \delta i \leq 1.71\%$

6.3.3 EBW slabs

The variables considered to develop an appropriate prediction equation for the EBW slabs in the cantilever direction regardless of their connection type are:

- ***a/t*** = shear span-to-slab thickness ratio.
- ***b_{eff}/t*** = effective width-to-thickness ratio.
- ***ρ^{-}/m*** = longitudinal reinforcement ratio for sagging bending moment per meter of slab width.
- ***f_{ye}/f'_{ce}*** = expected yield strength to expected unconfined concrete strength.
- ***a/b_{eff}*** = shear span-to-effective width ratio.
- ***EI_{pier}/EI_{EBW}*** = gross inertia of the framing element over the gross inertia of the EBW slab. For EBW-to-wallumn connections EI_{pier} is the gross inertia of the wallumn. For EBW-to-core connections EI_{pier} is the gross inertia of the wall pier.
- ***u_i/u_{max}*** = lateral displacement in the EBW over the displacement atop of the roof after applying the Simplified Drift Profile.

a/t, b_{eff}/t, ρ^{-}/m, f'_{ye}/f'_{ce}, and a/b_{eff} are geometric and material properties known to the structural designer after carrying out the gravity design of the GFRS. EI_{pier}/EI_{EBW} was included to assess if the interaction between the GFRS components could explain the values of the flexural effective stiffness modifiers. $u_i/u_{\max}$ was included based on the knowledge that larger demands will result in larger cracking of the corresponding RC members. The scatter plots of the variables used for the regression model of the EBW slabs are summarized in Figure 6.5.

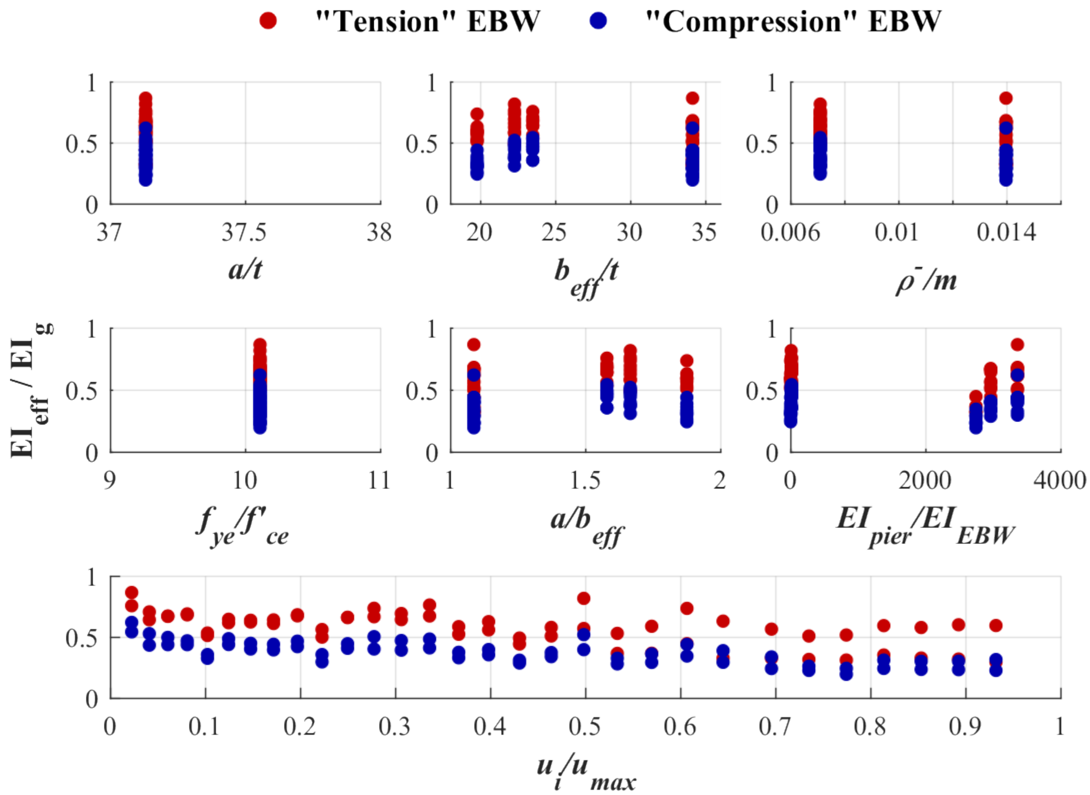

Figure 6.5 Scatter plot of the variables used to develop the EBW slabs flexural effective stiffness predictor equation in the cantilever direction.

The only possible trend to observe in Figure 6.5 is the almost constant relationship between the flexural effective stiffness modifiers and $u_i/u_{\max}$. It would seem feasible to develop and equation using this variable. Nevertheless, after attempting multiple regression models, it was observed that the scatter of the flexural stiffness modifiers in the $u_i/u_{\max}$ plot was excessively large to obtain a useful prediction equation. By sorting the flexural effective stiffness values of the EBW according to their connection (to a wallumn or to a pier), it was observed that the EBW-to-wallumn flexural stiffness modifiers presented the largest dispersion, as seen in Figure 6.6(a).

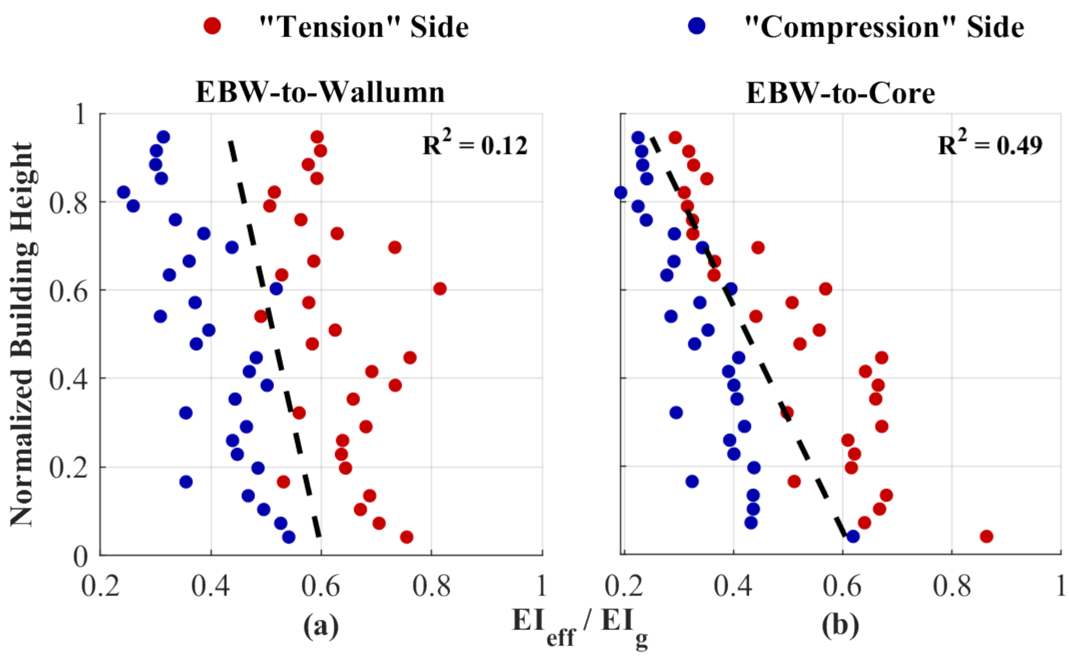

Figure 6.6 Distribution of flexural effective stiffness values for the EBW slabs in the cantilevered direction; (a) EBW-to-wallumn; (b) EBW-to-core.

The larger flexural effective stiffness modifiers deviation in the EBW-to-wallumn components can be attributed to the wide range of wallumn sizes, refer back to Table 3.4, which results in a larger spread of flexural stiffness modifiers. By contrast, the EBW-to-core slabs always frame into the same cantilever wall pier size, refer back to Figure 3.1, which results in less variability. Based on these observations, separate equations were developed for each EBW connection type. Sections 6.3.3.1 and 6.3.3.2 discuss the development of EBW-to-wallumn and EBW-to-core stiffness modifier predictor equations, respectively.

6.3.3.1 EBW-to-Wallumn

The variables previously described in Section 6.3.3 were also used to develop a prediction equation for the EBW-to-wallumn connection. However, it was found that the coefficient of determination for the best regression model was still very low ($R^2 \approx 0.30$). As a result, the development of a nonlinear regression model was explored for the most critical elements only, i.e., the "tension" side values. These values are the most critical because they experienced the largest demands, as previously reported in Figure 5.9. The scatter of the variables using the 30 flexural stiffness data points of the EBW-to-wallumn slabs on the "tension" side is displayed in Figure 6.7.

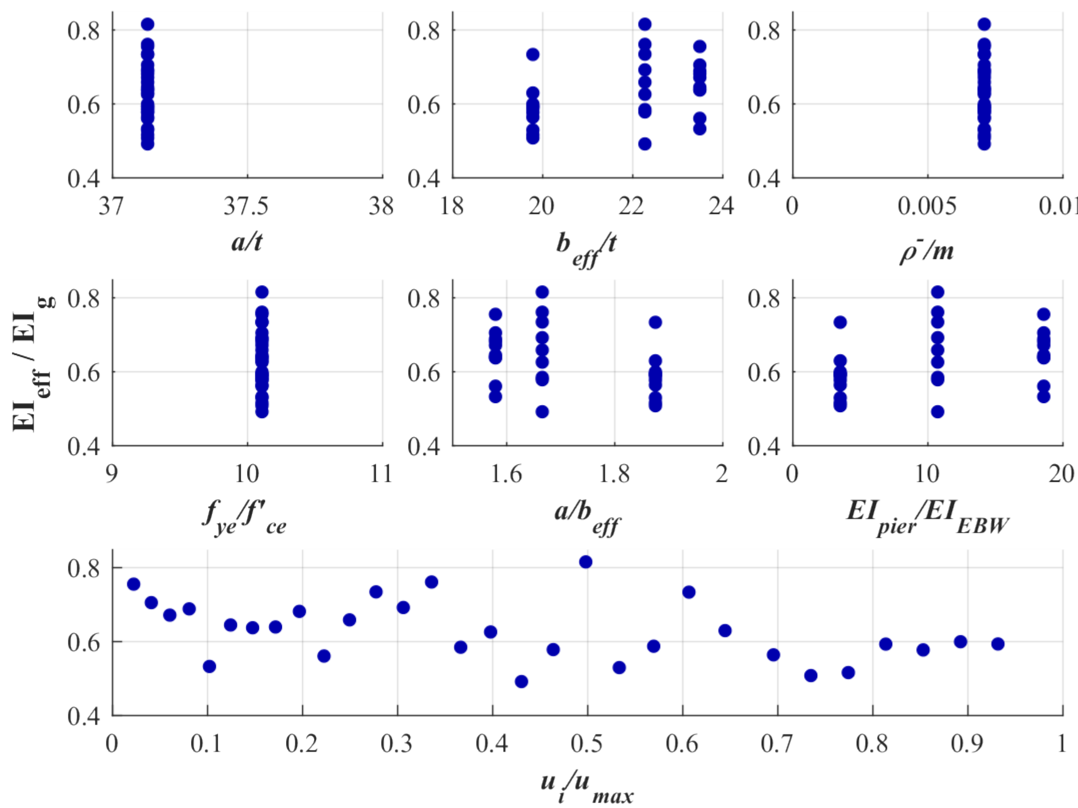

Figure 6.7 Scatter plot of the "tension" side variables used to develop the EBW-to-wallumn flexural effective stiffness predictor equation in the cantilevered direction.

a/t, $\bar{\rho}/m$, and f_{ye}/f'_{ce} were not included in the regression models since they do not explain nor contribute on the estimation of the flexural effective stiffness factors, as observed in Figure 6.7. The proposed regression model is presented in Equation (6.3). It includes a predictor that describes the geometric properties and a variable that accounts for the lateral deformation observed at each EBW-to-wallumn connection, b_{eff}/t and $u_i/u_{\max}$, respectively.

$$\frac{EI_{eff}}{EI_g} = 0.064\cos\left(21.2\frac{u_i}{u_{\max}}\right) + 0.029\frac{b_{eff}}{t} \leq 1.0 \tag{6.3}$$

$$R^2 = 0.435 \qquad \text{RMSE} = 0.064$$

Equation (6.3) is a clear example why RMSE is preferred over R^2. The R^2 results alone would imply the proposed equation might not be a good flexural effective stiffness estimator for EBW-to-wallumn members in the cantilevered direction. However, as observed in plot (a) of Figure 6.8, the predicted vs observed values lay closely around the 45-degree line, which suggests the model can accurately predict the corresponding flexural stiffness factors. The RMSE index validates the latter conclusion. This regression model supports the statement presented in Section 6.2 about the coefficient of determination being misleading when assessing nonlinear models.

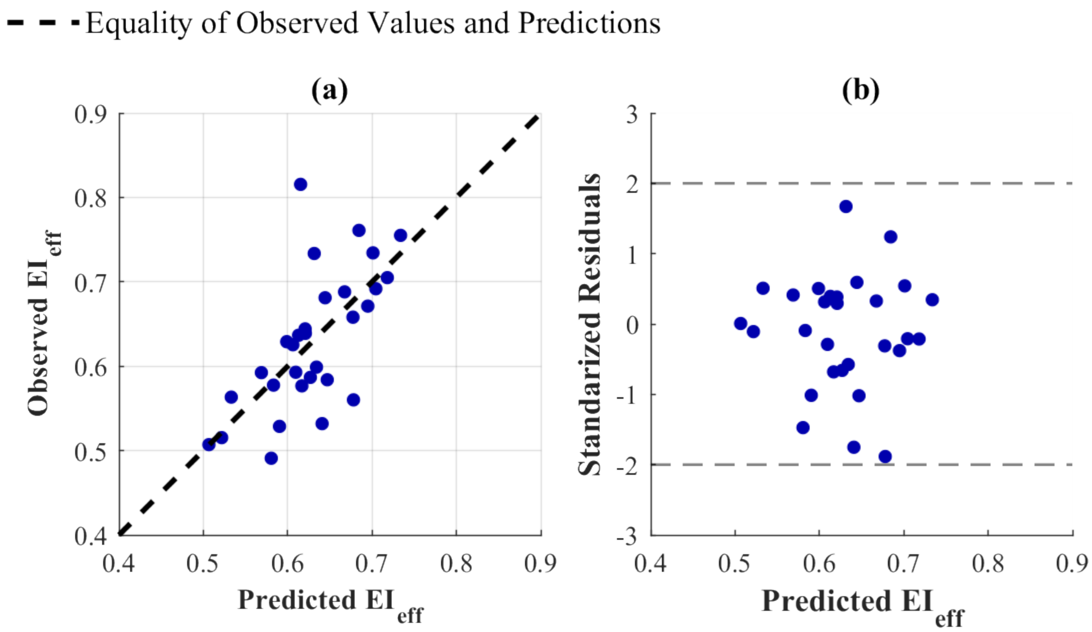

Figure 6.8 Regression model validation of Equation (6.3): (a) 45-degree line plot; (b) standardized residuals plot.

The variables of Equation (6.3) are in between the following intervals:

- $0.0227 \leq u_i/u_{\max} \leq 0.9321$
- $19.7919 \leq b_{eff}/t \leq 23.4992$

6.3.3.2 EBW-to-Core

The same predictors previously described in Section 6.3.3 were used to determine the predictive equation for EBW-to-core members in the cantilevered direction. Contrary to the EBW-to-wallumn slabs, both "tension" and "compression" values were included when developing the regression model because the scatter of the flexural stiffness values is less, refer back to Figure 6.6.

The scatter of the 60 EBW-to-core data points against their possible predictors is summarized in Figure 6.9. With the exception of $u_i/u_{\max}$, the remaining variables do not contribute to the estimation and were disregarded from the regression model. $u_i/u_{\max}$ appears to have a somewhat linear relationship with EI_{eff}/EI_g.

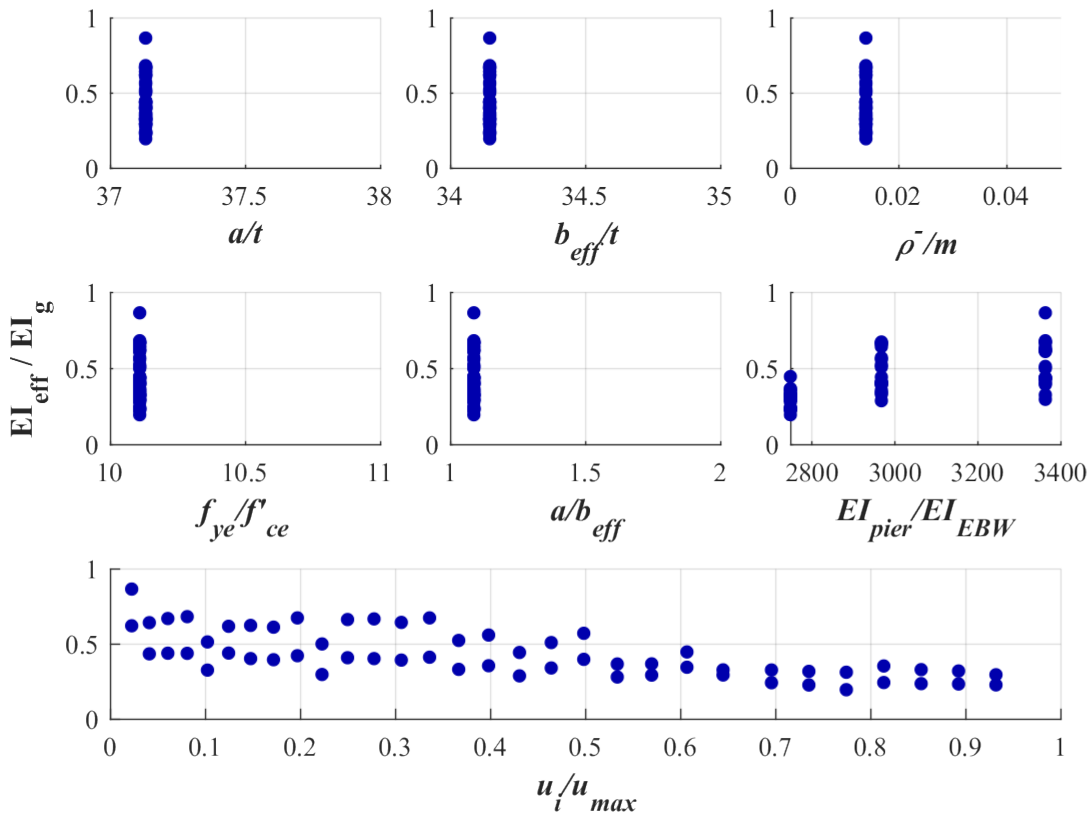

Figure 6.9 Scatter plot of the variables used to develop the EBW-to-core slabs flexural effective stiffness predictor equation in the cantilevered direction.

The resulting regression model for EBW-to-core slabs in the cantilever direction is presented in Equation (6.4).

$$\frac{EI_{eff}}{EI_g} = 0.588 - 0.383\frac{u_i}{u_{\max}} \leq 1.0 \tag{6.4}$$

$R^2 = 0.492 \qquad \text{RMSE} = 0.109$

Equation (6.4) does not present a variable that describes the geometric properties. This is because the effective width of the EBW-to-core slabs does not change throughout the building's height. The effective width is dependent on the wallumn or wall pier depth the slab frames into (refer back to Equation (2.2) and Figure 2.2). Since the depth of the cantilever wall pier is constant throughout the building height, the EBW-to-core effective width does not change and does not explain the variability of the flexural effective stiffness modifiers, as previously shown in Figure 6.9.

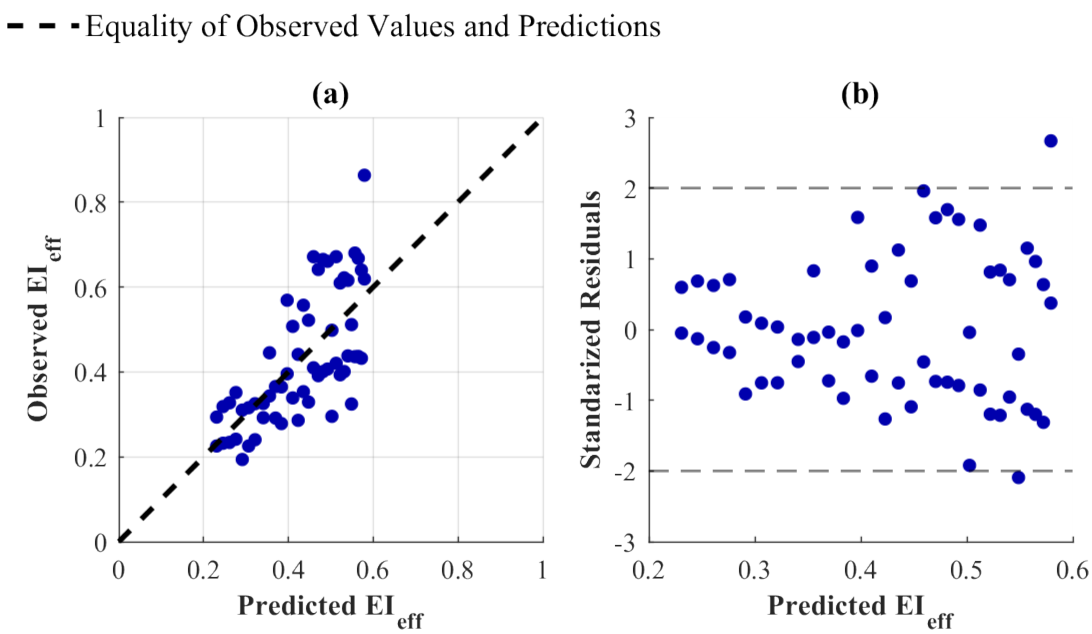

Figure 6.10 Regression model validation of Equation (6.4): (a) 45-degree line plot; (b) standardized residuals plot

Figure 6.10 illustrates the accuracy and soundness of Equation (6.4). The ranges of the predictor for the proposed equation are:

- $0.0227 \leq u_i/u_{max} \leq 0.9321$

6.4 Coupled Direction Prediction Equations

6.4.1 Outrigger Wallumns

The variables used to build the regression model for the outrigger wallumns in the coupled direction are consistent with those introduced in Section 6.3.1, with the exception of δi. This is because the Simplified Analysis drift profile in the coupled direction is uniform. In lieu of δi, the influence of the longitudinal rebar diameter-to-depth ratio, d_B/d, was explored. This ratio is also known by the structural engineer once the GFRS design has been carried out.

During the preliminary regression analyses it was found that the behaviour of three data points was not captured by any regression model. As defined by Anderson et al. (2010) "an outlier is a point that does not fit the trend shown by the remaining data". These data points could influence the accuracy of the developed flexural stiffness modifiers prediction equation. Devore (2011) suggests the following when potential outliers are detected: "When plots or other evidence suggest that the data set contains outliers or points having large influence on the resulting fit, one possible approach is to omit these outlying points and recompute the estimated regression equation. This would certainly be correct if it were found that the outliers resulted from errors in recording data values or experimental errors. If no assignable cause can be found for the outliers, it is still desirable to report the estimated equation both with and without outliers omitted". As it was explained in Section 5.2, one of the reasons why the linear-elastic columns' moment demands could not closely match the nonlinear moment demands at certain locations is attributed to the need to assign a single flexural effective stiffness modifier to each column type, resulting in experimental errors. Moreover, other authors (Sadeghian & Fam, 2015), removed these atypical values from the database to prevent saturation of the RMSE index (i.e., to reduce the mean error between the observed and predicted values).

Following Devore's (2011) approach, the prediction equation including the three outliers is shown first, refer to Equation (6.5). Then the scatter of the 57 flexural stiffness modifiers that resulted in the best regression model is presented in Figure 6.11. Last, the best regression model with only 57 flexural stiffness modifiers is shown in Equation (6.6). Goodness-of-fit estimators (R^2 and RMSE) are used to compare Equations (6.5) and (6.6). Thus, this will demonstrate why including the three potential outliers decreases the prediction power of the proposed regression model for outrigger wallumns in the coupled direction.

$$\frac{EI_{eff}}{EI_g} = 0.616e^{\left[-\left(\frac{\frac{u_i}{u_{\max}}-0.155}{0.0445}\right)^2\right]} + 0.305e^{\left[-\left(\frac{\frac{u_i}{u_{\max}}-0.758}{0.320}\right)^2\right]} + 3.737M_D \leq 1.0 \tag{6.5}$$

$$R^2 = 0.213 \qquad \text{RMSE} = 0.250$$

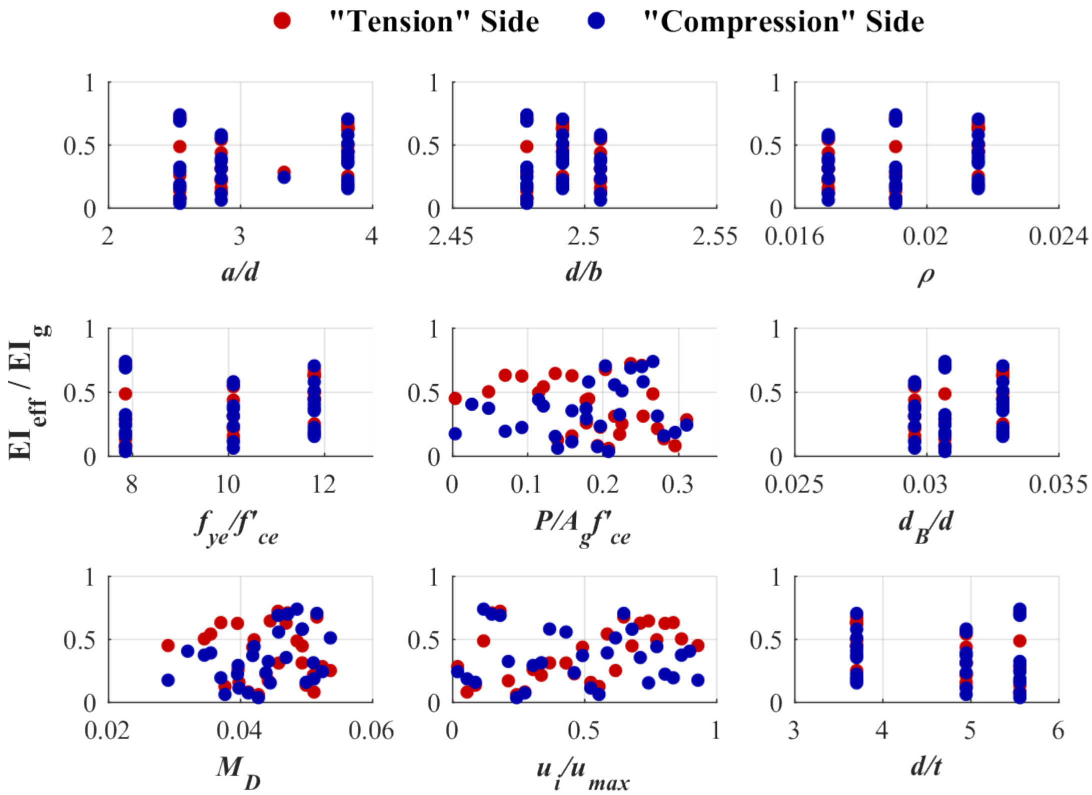

Figure 6.11 Scatter plot of the variables used to develop the flexural effective stiffness predictor equation for the outrigger wallumn equation in the coupled direction.

Referring back to Figure 5.10, the largest moment demands at the outrigger wallumns in the coupled direction are observed in the bottom storeys. An oscillatory moment demand shape is also noticeable. From this assessment, two possible functions could model this behaviour 1) an exponential function that can predict the bottom peak demand or 2) sine or cosine functions that describe the moment demand shape pattern. Equation (6.6) was the best regression model for outrigger wallumns in the coupled direction.

$$\frac{EI_{eff}}{EI_g} = 0.616e^{\left[-\left(\frac{\frac{u_i}{u_{\max}}-0.155}{0.0445}\right)^2\right]} + 0.305e^{\left[-\left(\frac{\frac{u_i}{u_{\max}}-0.758}{0.320}\right)^2\right]} + 3.737M_D \leq 1.0 \quad (6.6)$$

$R^2 = 0.496$ RMSE = 0.158

Equation (6.5), which includes the three potential outliers, presents and $R^2 = 0.213$ and RMSE = 0.250. In contrast, Equation (6.6), while not considering the potential outliers, has a better prediction power demonstrated by a higher $R^2 = 0.496$ and a lower RMSE = 0.158. R^2 and RMSE support the assumption that these three outliers do not fit the remaining data of this model which may have occurred as an experimental error caused by the calibration procedure described in Section 5.2. Because of this, Equation (6.6) is deemed as a better flexural effective stiffness modifier prediction equation for outrigger wallumns in the coupled direction.

In contrast with Equation (6.1) for outrigger wallumns in the cantilevered direction, the equation for outrigger wallumns in the coupled direction includes $u_i/u_{\max}$ instead of δi. As mentioned earlier, this is because the uniform interstorey drift ratio in the coupled direction results in δi values that do not add variability to the prediction. Figure 6.12 shows that the predicted values of Equation (6.6) are in good agreement with the experimental values.

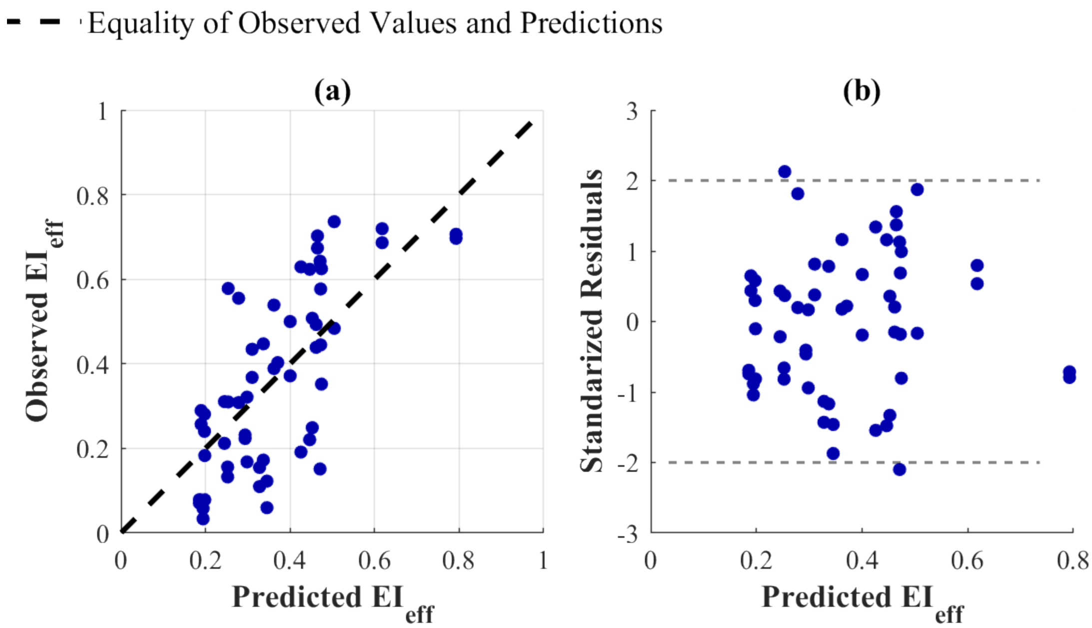

Figure 6.12 Regression model validation of Equation (6.6): (a) 45-degree line plot; (b) standardized residuals plot.

The predictors' intervals of the proposed equation for outrigger wallumns in the coupled direction are:

- $0.0205 \leq u_i/u_{\max} \leq 0.9306$
- $0.0291 \leq M_D \leq 0.0537$

6.4.2 Non-outrigger Square Columns

The predictor variables used for non-outrigger square columns in the coupled direction are consistent with those used in the cantilevered direction, as described earlier in Section 6.3.1. As with the non-outrigger square columns in the cantilever direction, the *d/t* variable was removed from the regression model because it only applies to outrigger elements. Also, *δi* was substituted by d_B/d since the interstorey drift profile in the coupled direction is uniform as previously explained in Section 6.4.1.

Along with the outrigger wallumns in the coupled direction, the potential single outlier that saturated the RMSE index was eliminated from the database (Sadeghian & Fam, 2015). Devore's (2011) approach previously explained in Section 6.4.1 is used to demonstrate that the outlier does not fit the trend of the remaining data. First the regression model of Equation (6.7), which includes the potential outlier, is presented. Second, the scatter of the predictors that resulted in the best regression model and do not consider the potential outlier is summarized in Figure 6.13. Last, the best regression model with only 29 flexural stiffness modifiers is shown in Equation (6.8). Goodness-of-fit estimators (R^2 and RMSE) are used to compare Equations (6.7) and (6.8). Thus, this will demonstrate why including the single potential outlier decreases the prediction power of the proposed regression model for non-outrigger square columns in the coupled direction.

$$\frac{EI_{eff}}{EI_g} = 0.512 - 0.214\cos\left(24.982\frac{u_i}{u_{\max}}\right) - 0.152\sin\left(24.982\frac{u_i}{u_{\max}}\right) \leq 1.0 \tag{6.7}$$

R^2 = -0.281 RMSE = 0.273

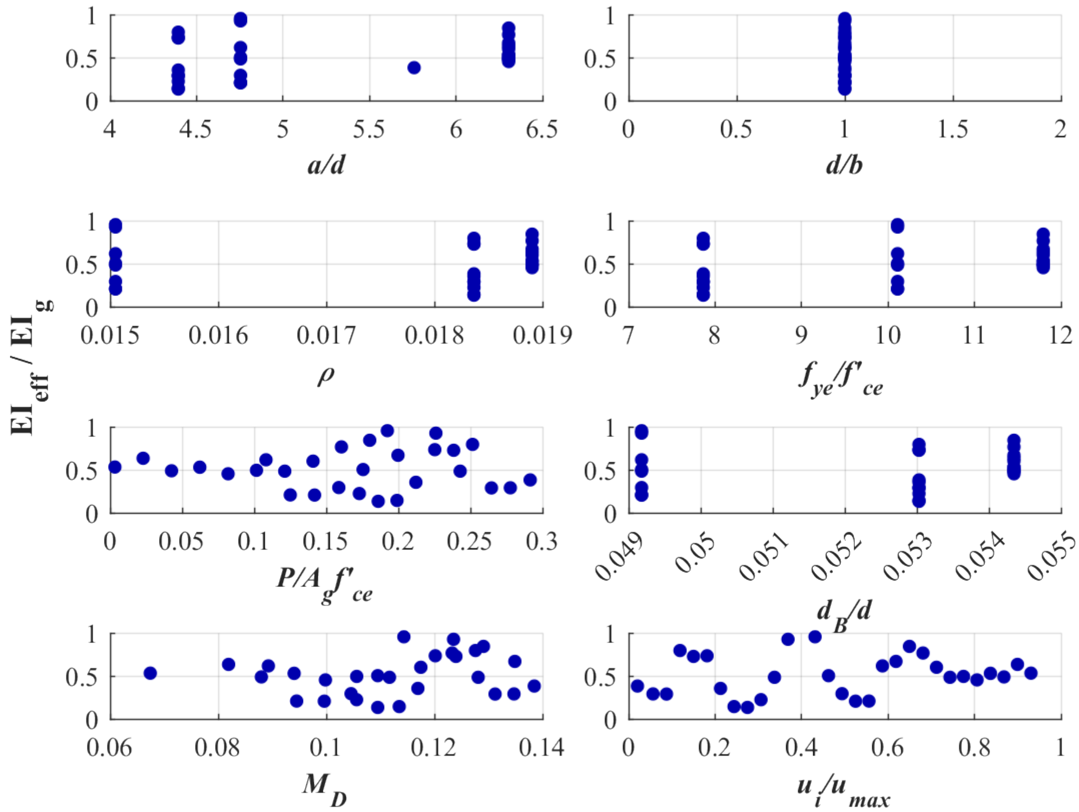

Figure 6.13 Scatter plot of the variables used to develop the flexural effective stiffness predictor equation for the non-outrigger square columns equation in the coupled direction.

From Figure 6.13, it is observed that d/b does not explain the data, hence it was removed from the analysis. It can also be observed that variables M_D and $u_i/u_{\max}$ show an oscillatory pattern. Referring back to plot (c) of Figure 5.10, the shape of the bending moment demands suggests that a regression model that takes the form of an exponential function might be able to replicate the peak demand at the bottom storeys. Based on these observations and iterative analysis, Equation (6.8) presents the proposed regression model for non-outrigger square columns in the coupled direction.

$$\frac{EI_{eff}}{EI_g} = 0.512 - 0.214\cos\left(24.982\frac{u_i}{u_{\max}}\right) - 0.152\sin\left(24.982\frac{u_i}{u_{\max}}\right) \leq 1.0 \tag{6.8}$$

$R^2 = 0.659$ RMSE = 0.144

Equation (6.7) presents and $R^2 = -0.281$ and RMSE = 0.273. In contrast, Equation (6.8)has a better prediction power demonstrated by a higher $R^2 = 0.659$ and a lower RMSE = 0.144. The negative R^2 value of the regression model that includes the potential outlier proves itself that the outlier does not fit the remaining data of this model. As previously described in Section 6.4.1 experimental errors may have occurred by following the calibration procedure described in Section 5.2. Because of this, Equation (6.8), which does not include the outlier, is deemed as a better flexural effective stiffness modifier prediction equation for non-outrigger square columns in the coupled direction.

Equation (6.8) does not include any variables that describes the geometry or material properties of the non-outrigger square columns. The cross-section properties of these elements, previously presented in Table 3.5, shows small variability, particularly in the bottom 20 storeys. This results in a limited contribution of the cross-section properties to the prediction equation. By contrast, the variable $u_i/u_{\max}$ is a good predictor according to R^2 and the RMSE indices. These findings are also supported by the 45-degree line plot showed in Figure 6.14.

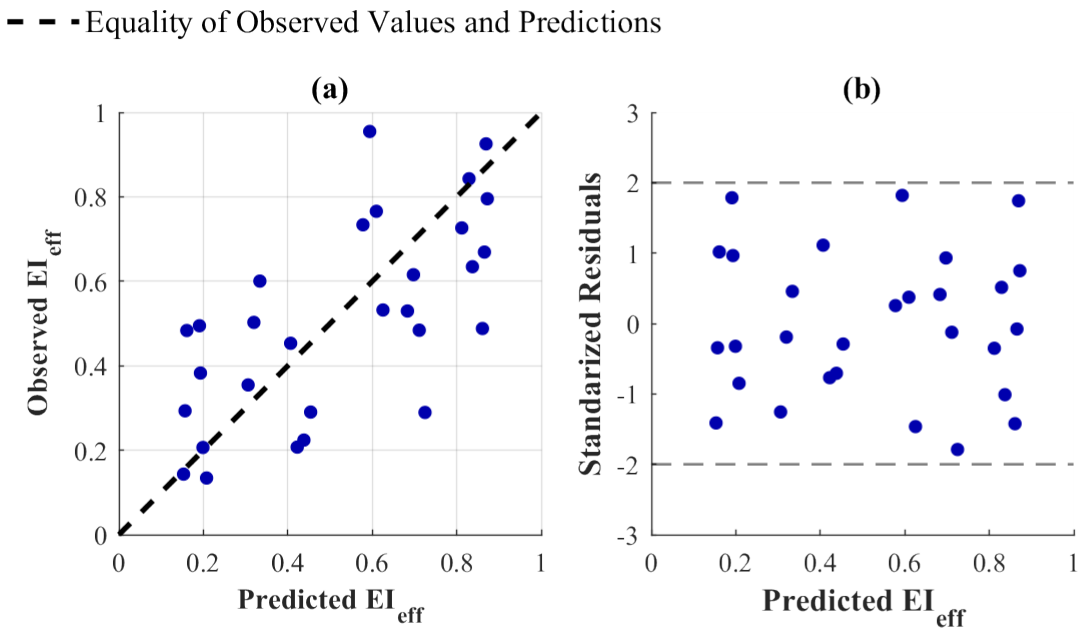

Figure 6.14 Regression model validation of Equation (6.8): (a) 45-degree line plot; (b) standardized residuals plot.

The ranges of the variable seen in Equation (6.8) are:

- $0.0205 \leq u_i/u_{\max} \leq 0.9306$

6.4.3 EBW slabs

The predictors used for the EBW slabs in the coupled direction are the same as those used in the cantilevered direction, presented earlier in Section 6.3.3. The scatter of the 120 flexural effective stiffness data points for all the EBW slabs in the coupled direction is shown in Figure 6.15. The $u_i/u_{\max}$ variable appears to be linearly related to the flexural effective stiffness.

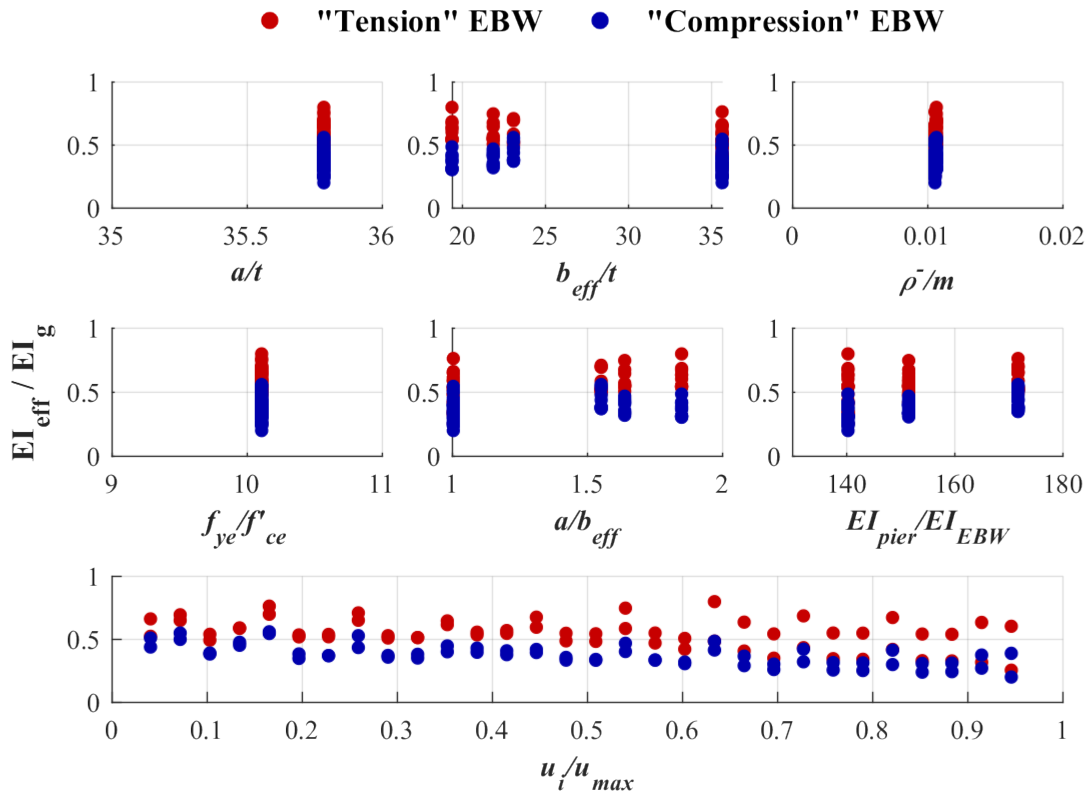

Figure 6.15 Scatter plot of the variables used to develop the flexural effective stiffness predictor equation for EBW slabs equation in the coupled direction.

Contrary to the EBW slabs in the cantilevered direction, in the coupled direction it was possible to propose a single equation for all the EBW slabs regardless of their connection type because the dispersion of $u_i/u_{\max}$ is less pronounced in the coupled direction than in the cantilevered, as observed by comparing Figure 6.5 and Figure 6.15. Equation (6.9) is the proposed equation for EBW slabs in the coupled direction.

$$\frac{EI_{eff}}{EI_g} = 0.209 + 0.012\frac{b_{eff}}{t} - 0.163\frac{u_i}{u_{\max}} \leq 1.0 \tag{6.9}$$

$$R^2 = 0.570 \qquad \text{RMSE} = 0.086$$

Equation (6.9) is conformed by two variables. b_{eff}/t characterizes the geometric properties of the EBW component and $u_i/u_{\max}$ accounts for the level of lateral displacement.

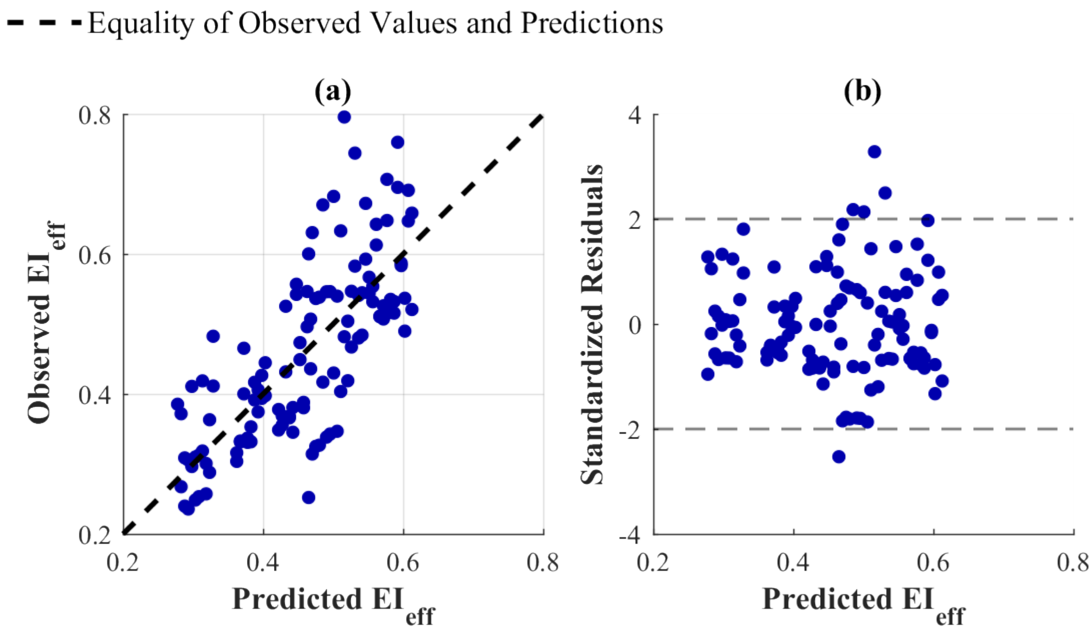

Figure 6.16 Regression model validation of Equation (6.9): (a) 45-degree line plot; (b) standardized residuals plot.

Based on the results presented in Figure 6.16, the proposed equation for EBW slabs in the coupled direction is satisfactory. Even though five residuals are beyond the two standard deviation limit, these outliers represent less than 5% of the database. The ranges of the variables expressed in Equation (6.9) are:

- $19.34 \leq b_{eff}/t \leq 35.61$
- $0.0409 \leq u_i/u_{\max} \leq 0.9462$

Chapter 7: Prediction Power of Proposed Equations

This chapter intends to evaluate the effectiveness of Equations (6.1) to (6.4), (6.6), (6.8), and (6.9) presented in Chapter 6, as tools to estimate the flexural effective stiffness modifiers for elements of the GFRS for use in the implementation of the General and Simplified Analysis procedures described in § 21.11.2.1 and § 21.11.2.2 of CSA A23.3-19 , respectively. To assess their prediction power, the seismic demands in GFRS components derived by means of a linear-elastic model that employs flexural effective stiffness modifiers as derived from the *Proposed Equations* will be compared against the observed demands in a detailed nonlinear analysis model, when both models are subjected to the same drift profile. Furthermore, the performance of the proposed flexural effective stiffness modifiers will be benchmarked against the recommendations found in CSA A23.3-19 for the SFRS members if applied to the GFRS components. This is described in Section 7.1.

Two buildings, hereinafter called *Building Model 1* and *2*, with the same SFRS, but distinct GFRS will be used in the assessment. The major differences are 1) the depth-to-width wallumn ratio was increased from 2.5 to 5.25 in average, 2) the effective width of EBW-to-wallumn slabs was increased by 21% in average. A more detailed description of the differences between both buildings is presented in Section 7.3. The first goal of this exercise is to ensure there is no significant loss of accuracy when using the generalized expressions. The second goal is to check the prediction power of the equations when a different GFRS is used. The flexural effective stiffness modifiers used in each *Building Model* 1 and *2* are summarized in Appendix C

7.1 CSA A23.3-19 Stiffness Modifiers

The General Analysis of CSA A23.3-19 in its requirements for the upper-bound effective stiffness for the GFRS components states: "Low estimates of average section properties such as those given in Clause 21.2.5.2 are used for the SFRS to make a safe estimate of the design displacements of the overall building. Higher estimates of section properties must be used for each structural members not considered part of the SFRS to make a safe estimate of the forces induced in these members by the design displacements of the SFRS" (pp. 204-205). The low estimates of § 21.2.5.2 are:

$$\frac{EI_{eff}}{EI_g} = \begin{cases} 0.5 + 0.6\dfrac{P}{A_g f'_c} \text{ for columns} \\ 0.2 \text{ for slabs} \end{cases} \tag{7.1}$$

Although the code is clear that the above equations are not meant to estimate the GFRS forces, the wording could be seen to imply that the resulting stiffness modifiers shown above serve as a lower bound factors for elements of the GFRS . For this reason, the results presented in this chapter also include the results obtained by adopting the expressions presented above, hereinafter referred to as *Code Equations*, in lieu of those derived in Chapter 6. To be consistent with the *Proposed Equations*, f'_c in Equation (7.1) was replaced by f'_{ce}.

7.2 Building Model 1

This first model is consistent with the archetype building used throughout this study. This building follows the typology described in Section 3.1 and displayed in Figure 3.1. The material and geometric properties of the GFRS could be retrieved from Table 3.1, Table 3.2, Table 3.4, Table

3.5, and Table 4.4. The main reason to assess this building is to check if the *Proposed Equations* return flexural effective stiffness modifiers that result in consistent linear-elastic demands compared to the nonlinear virtual twin (i.e., there is no loss of accuracy).

In their designs, structural engineers will group element types that will be defined for the largest demands. For instance, if all columns in the lowermost stories have the same cross section geometry, the largest demands will be used to detail the cross-section and define the necessary material properties. In the case study archetype building, the columns were divided into three groups, previously reported in Table 3.4 and Table 3.5. Column group A contains all columns from grade to level 11, column Group B contains all columns from level 11 to 21, and column group C contains all columns from level 21 to 31. These groups will be hereinafter referred to as the bottom, middle, and top groups for comparison purposes. While the same rationale was applied for EBW slabs, the resulting EBW-to-core slabs were identical through all levels, therefore, a single group applies to these components. To assess the prediction power of the *Proposed Equations* and the *Code Equations*, the maximum linear-elastic flexural demands of each component group are compared against the peak moment demands derived from the detailed nonlinear analysis model.

7.2.1 Cantilever Direction

7.2.1.1 Columns

Figure 7.1 shows the moment demands throughout the height of the building as predicted by the linear-elastic models with flexural effective stiffness modifiers from the *Proposed* and *Code Equations* as well as those from the nonlinear model for outrigger wallumns and non-outrigger square columns. The resulting demands using both the *Proposed* and the *Code* equations follow a similar pattern and peak values. Both the linear-elastic *Proposed* and *Code* demands overestimate the nonlinear moment demand at grade. Both sets of equations were unable to capture the nonlinear demands observed from levels 7 to 10 in all the column types. An explanation about this is found in Section 5.2.

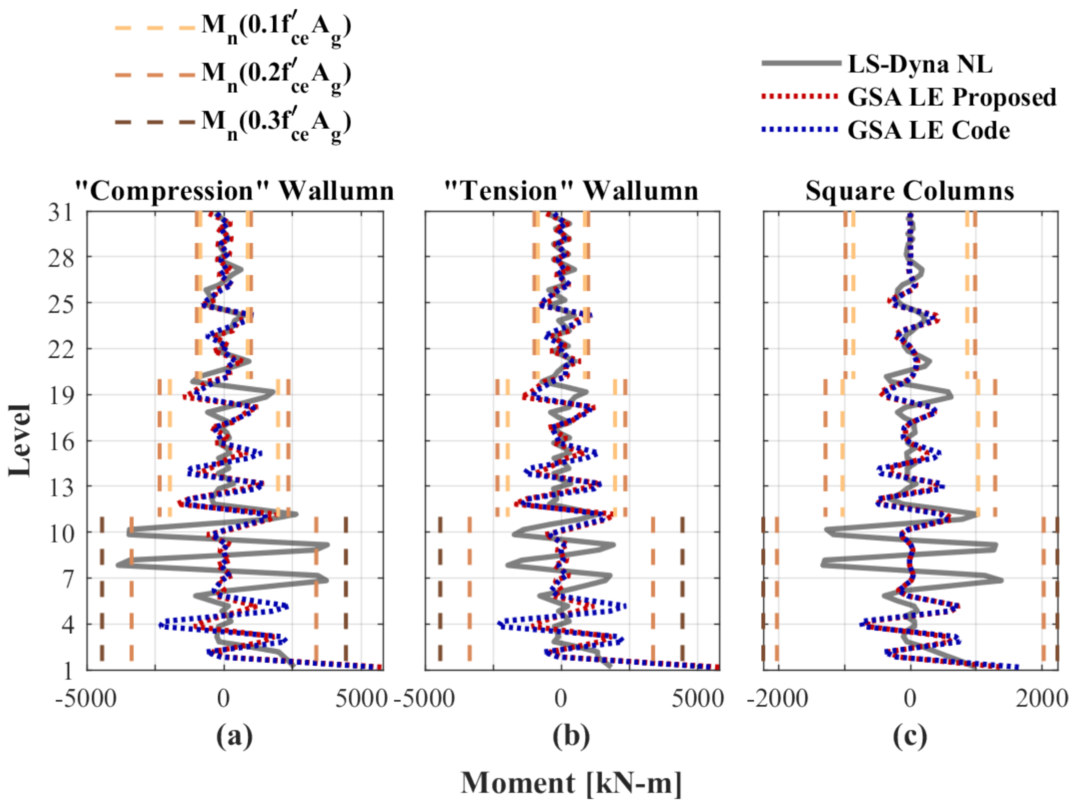

Figure 7.1 Linear-elastic *Building Model 1* demands with EI_{eff} values computed through the proposed prediction equations (red) and code equations (blue) vs nonlinear bending moment demands for columns in the cantilever direction; (a) “compression” wallumn; (b) “tension” wallumn; (c) square columns.

Figure 7.2 illustrates the peak linear-elastic bending moment demands to peak nonlinear bending moment demands ratio of outrigger wallumns and non-outrigger square columns. The *Proposed* and *Code Equations* captured the maximum observed nonlinear moment demand in most of the component groups. With the exception of the square columns in the middle storeys, both sets of equations provided safe estimates of demands (i.e., they overestimate the bending moments predicted by the nonlinear model). The linear-elastic moment demands of the middle storeys in plots (a) and (c) illustrate a better agreement between the linear-elastic and nonlinear demands when the *Proposed Equations* are used. Equation (6.2) underestimates the demands in the middle storeys of plot (c) by 21%, whereas the *Code Equation* falls short by 27%.

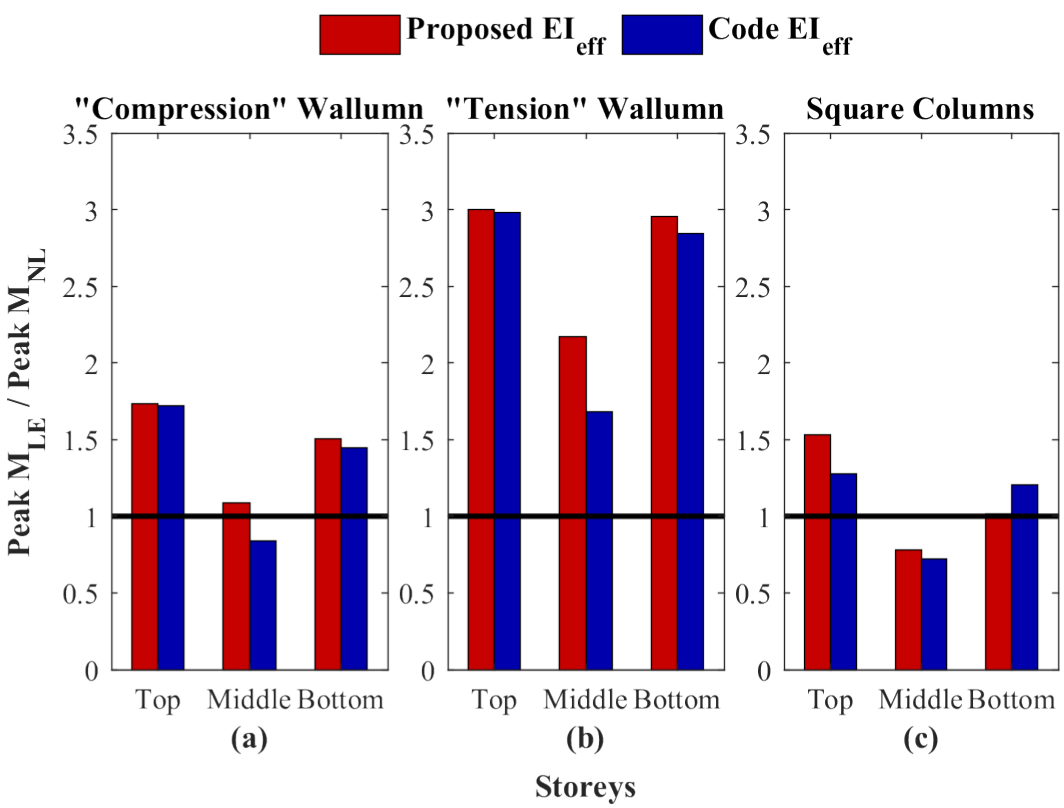

Figure 7.2 *Building Model 1* peak linear-elastic-to- peak nonlinear moment demands ratio for columns in the cantilever direction; (a) "compression" wallumn; (b) "tension" wallumn; (c) square columns.

7.2.1.2 EBW slabs

Figure 7.3 summarizes the linear-elastic and nonlinear bending moment demands for the EBW components. In contrast with the results presented in Section 7.2.1.1 for the columns, which showcased fairly consistent behaviour between the *Proposed* and *Code* equations, the EBW slabs demands indicate considerably better alignment between the *Proposed Equations* and the nonlinear model. The results in Figure 7.3 showcase how the *Code Equation* considerably underestimates the flexural demands in the slabs.

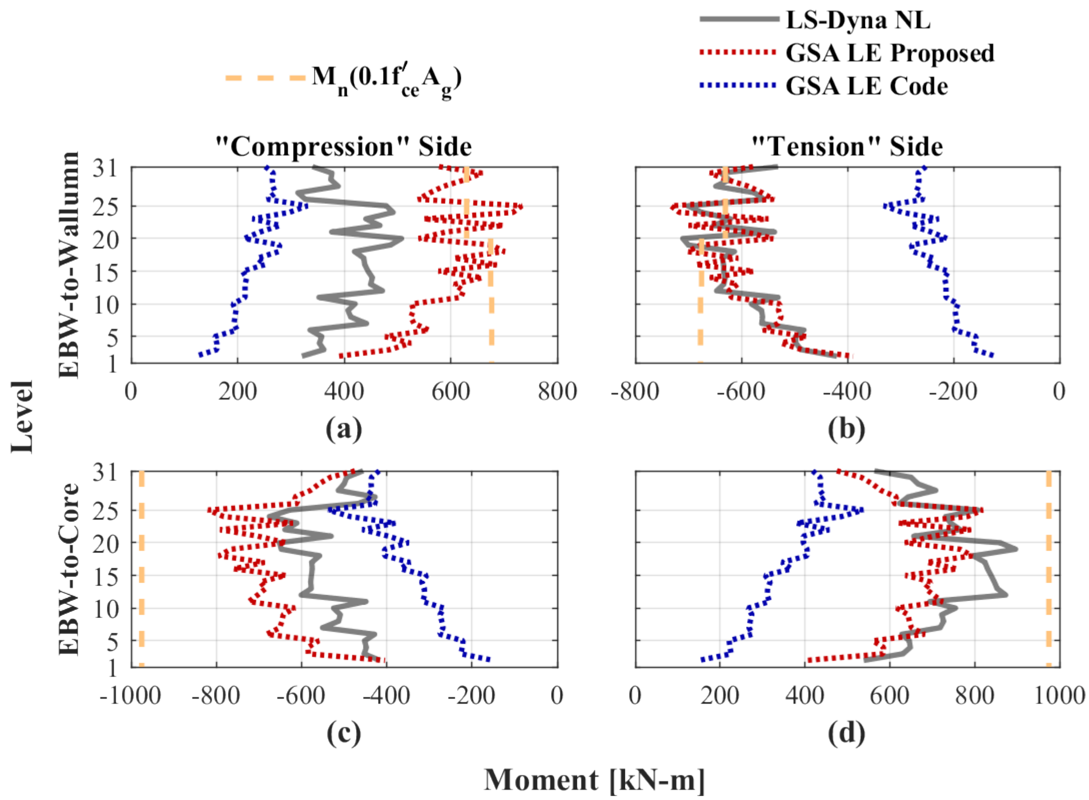

Figure 7.3 Linear-elastic *Building Model 1* demands with EI_{eff} values computed through the proposed prediction equations (red) and code equations (blue) vs nonlinear bending moment demands for EBW slabs in the cantilever direction; (a) EBW-to-wallumn "compression" side; (b) EBW-to-wallumn "tension" side; (c) EBW-to-core "compression" side; (d) EBW-to-core "tension" side.

Figure 7.4 provides the peak linear-elastic to peak nonlinear bending moment demand ratio for EBW components. As observed in the figure, the *Proposed Equations* for EBW slabs in the cantilevered direction are consistent with the observed nonlinear moment demands. By contrast, the 0.2 effective stiffness value of the *Code Equation* for all slabs provided a poor prediction. The *Code Equation* fell 21 to 63% short in all the storeys and connection types.

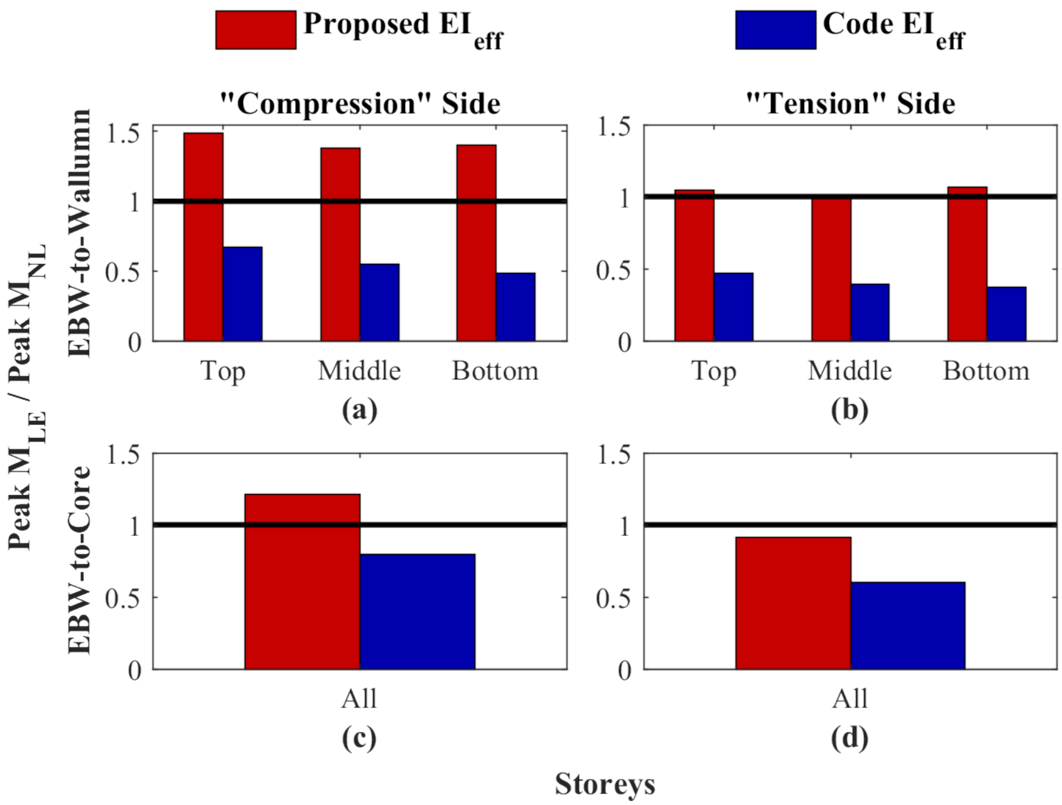

Figure 7.4 *Building Model 1* peak linear-elastic-to-peak nonlinear moment demands ratio for EBW slabs in the cantilever direction; (a) EBW-to-wallumn "compression" side; (b) EBW-to-wallumn "tension" side; (c) EBW-to-core "compression" side; (d) EBW-to-core "tension" side.

7.2.2 Coupled Direction

7.2.2.1 Columns

The *Code Equation* to compute the flexural effective stiffness modifier for columns returned moment demands that excessively overestimate the nonlinear value at grade level. The *Proposed Equations* (6.6) and (6.8) yield flexural effective stiffness factors that result in more consistent moment demands at grade, as seen in Figure 7.5. The *Proposed* and *Code Equations* seem to capture the proper moment demand shape and values at levels above grade.

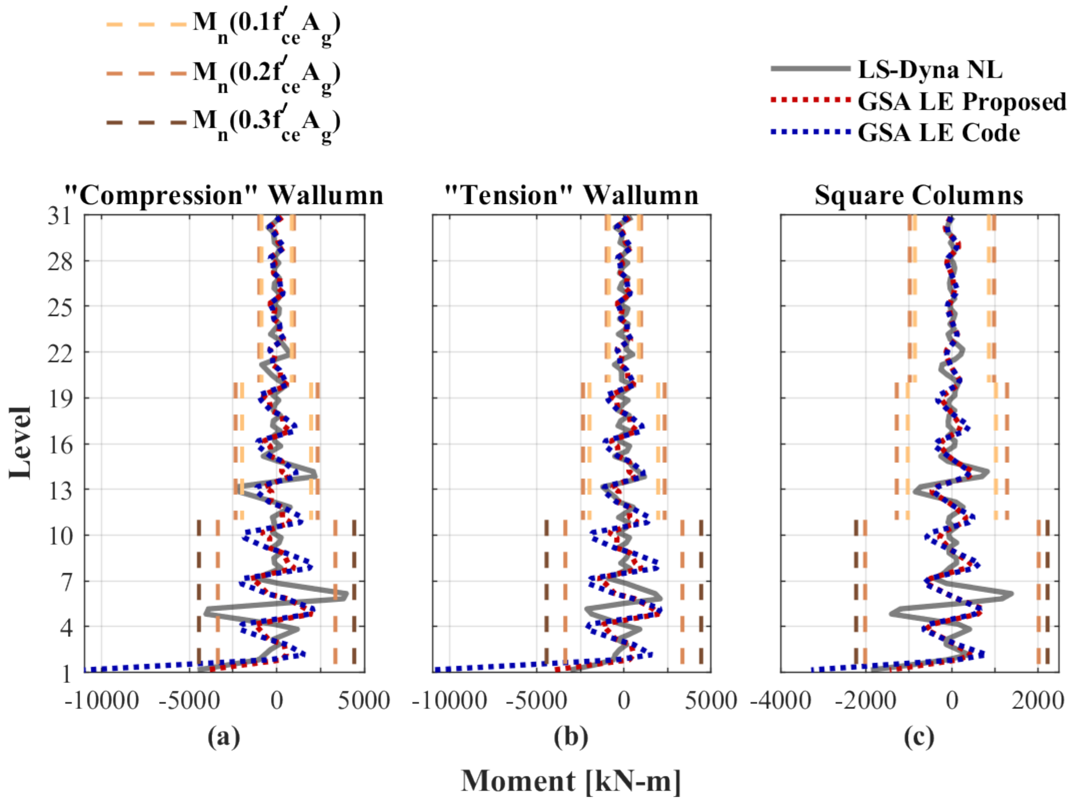

Figure 7.5 Linear-elastic *Building Model 1* demands with EI_{eff} values computed through the proposed prediction equations (red) and code equations (blue) vs nonlinear bending moment demands for columns in the coupled direction; (a) "compression" wallumn; (b) "tension" wallumn; (c) square columns.

Figure 7.6 shows that the *Code Equation* provided a more conservative, although unrealistic, estimate of demands for all column types at grade level. By contrast, the *Proposed Equations* for columns in the coupled direction were closer to the nonlinear demands than the *Code Equation* in the bottom storeys as seen in Figure 7.6(a) to 7.6(c). Both sets of equations slightly underestimated the demand at the top and middle storeys for the "compression" outrigger wallumn and non-outrigger square columns. When the *Proposed* and *Code Equations* fell short, they underestimate the demands by 26% and 21% in average, respectively.

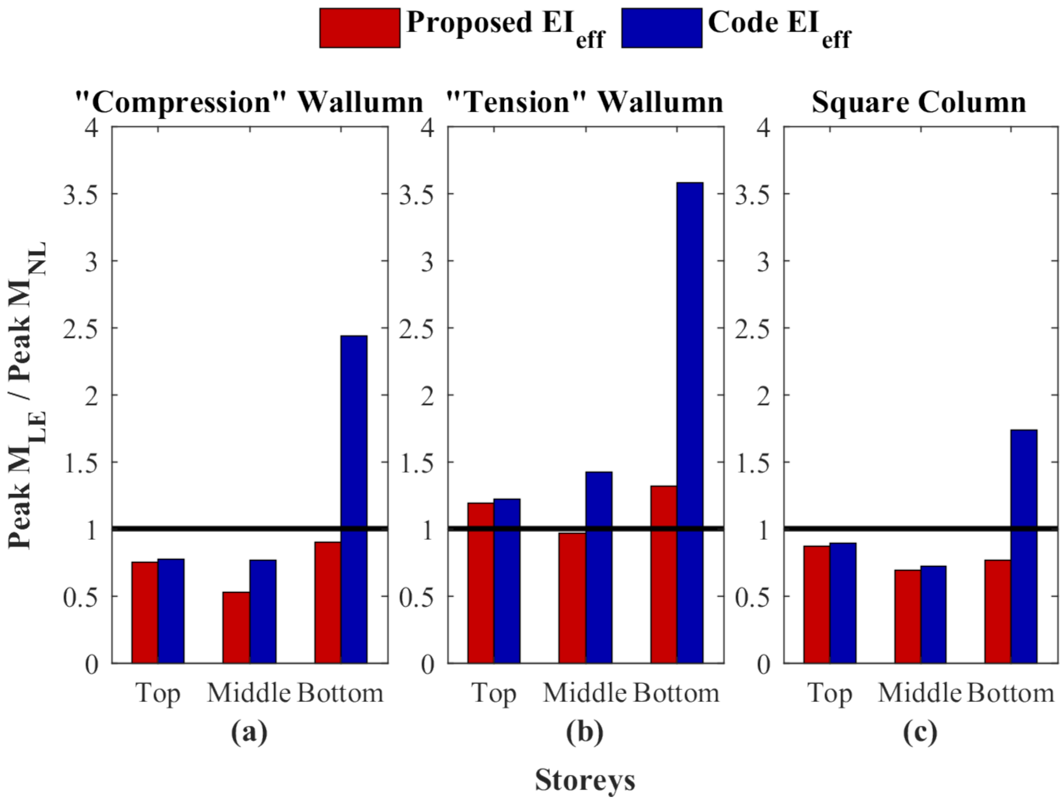

Figure 7.6 *Building Model 1* peak linear-elastic-to-peak nonlinear moment demands ratio for columns in the coupled direction; (a) "compression" wallumn; (b) "tension" wallumn; (c) square columns.

7.2.2.2 EBW slabs

For the EBW slabs in the coupled direction, except for the EBW-to-wallumn in the "tension" side, the EI_{eff} factors computed through the *Proposed Equation* (6.9) resulted in accurate estimates of linear-elastic demands, as shown in Figure 7.7. The *Code* value of 0.2 underestimated the moment demands observed in the nonlinear model.

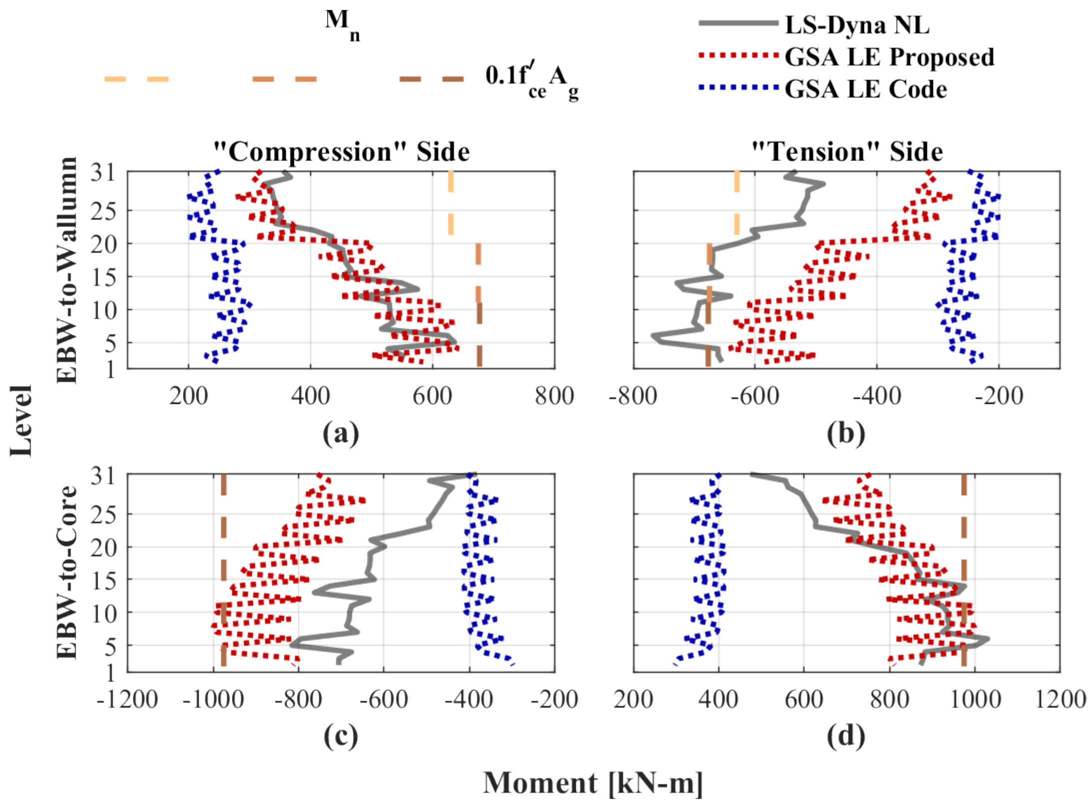

Figure 7.7 Linear-elastic *Building Model 1* demands with EI_{eff} values computed through the proposed prediction equations (red) and code equations (blue) vs nonlinear bending moment demands for EBW slabs in the coupled direction; (a) EBW-to-wallumn "compression" side; (b) EBW-to-wallumn "tension" side; (c) EBW-to-core "compression" side; (d) EBW-to-core "tension" side.

Figure 7.8 demonstrates that the *Proposed Equation* for EBW slabs in the coupled direction yielded more conservative estimates of moment demands in most of the cases. The *Proposed Equation* did not capture the maximum nonlinear moment demands for EBW-to-wallumn components in the "tension" side. Nevertheless, it returned better estimates than the *Code* equation. In all cases, the *Code* stiffness modifier of 0.2 miscalculated the moment demands, underestimating their values by 43 to 60%.

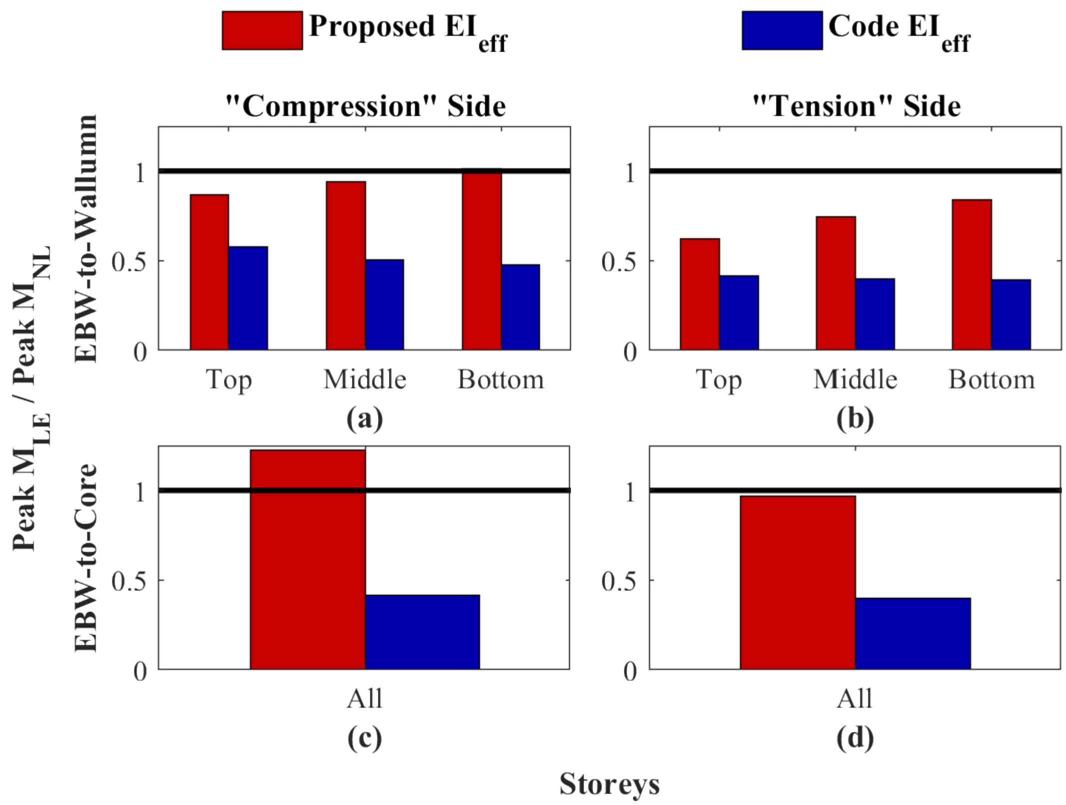

Figure 7.8 *Building Model 1* peak linear-elastic-to-peak nonlinear moment demands ratio for EBW slabs in the coupled direction; (a) EBW-to-wallumn "compression" side; (b) EBW-to-wallumn "tension" side; (c) EBW-to-core "compression" side; (d) EBW-to-core "tension" side.

7.3 Building Model 2

This building model adopts the same SFRS as the building assessed in Section 7.2, but introduces some modifications to the GFRS. The non-outrigger square columns layout is the same as in the building presented in Section 7.2, i.e., it follows Table 3.5. Nevertheless, the cross-section properties of outrigger wallumns and EBW-to-wallumn slabs were modified. Compared to *Building Model 1*, the depth-to-width wallumn ratio was increased from 2.5 to 5.25 on average. The effective width of EBW-to-wallumn slabs was increased by 21% in average because the wallumn depth increased, refer back to Section 2.5. The layout of EBW-to-core slabs remained the same. The revised geometric properties of *Building Model 2* are summarized in Table 7.1 and Table 7.2, where the original dimensions of *Building Model 1* are shown in parenthesis. A visual contrast between the two models is shown in Figure 7.9. It is clear that the *Building Model 1* outrigger wallumns are less elongated than those in *Building Model 2*. Moreover, the EBW-to-wallumn is smaller in *Building Model 1* compared to *Building Model 2*. The prediction power of the cantilevered direction Equations (6.1) to (6.4) are discussed in Section 7.3.1. The coupled direction Equations (6.6), (6.8), and (6.9) are evaluated in Section 7.3.2. The component groups and peak moment comparison follow the same rationale explained for *Building Model 1* in Section 7.2. The GFRS of *Building Model 2* is able to accommodate the design gravity demands described in Table 3.3.

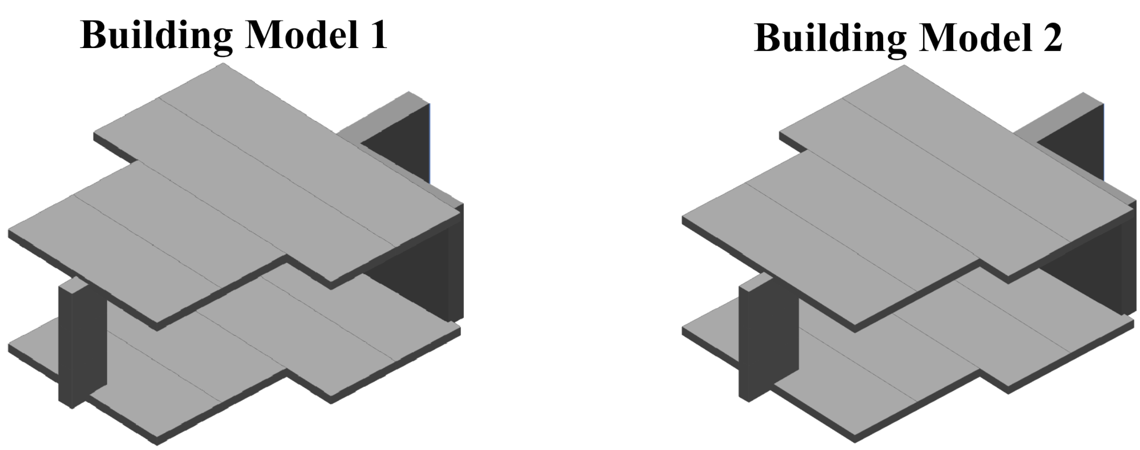

Figure 7.9 GFRS differences between *Building Model 1* and *2*.

Table 7.1 *Building Model 2* geometry and reinforcement layout summary for outrigger wallumns.

Level	**Depth (*D*) [mm]**	**Width (*b*) [mm]**	**Longitudinal Bar Size (ϕ_l)**	**10M Tie Spacing (*s*) [mm]**
21 to 31	(760) 1140	(305) 250	(10) 12-25M	300
11 to 21	(1015) 1520	(405) 305	(10) 12-30M	300
6 to 11	(1140) 1700	(460) 305	(10) 12-35M	300
1 to 6	(1140) 1700	(460) 305	(10) 12-35M	200

Table 7.2 *Building Model 2* geometry and reinforcement layout summary for EBW slabs.

Direction	**Level**	**Effective width (b_{eff}) [mm]**	**15M bars (hogging moment)**	**10M bars (sagging moment)**	**Connection type**
Cantilever	2 to 31	7000	40	14	EBW-to-core
Coupled	2 to 31	7300	32	14	
Cantilever	21 to 31	(4060) 4820	24	(8) 10	EBW-to-wallumn
	12 to 20	(4570) 5580	24	(10) 12	
	2 to 11	(4820) 5940	24	(10) 12	
Coupled	21 to 31	(3970) 4730	27	(8) 10	
	12 to 20	(4480) 5490	27	(10) 12	
	2 to 11	(4730) 5850	27	(10) 12	

7.3.1 Cantilever Direction

7.3.1.1 Columns

Consistent with the results of *Building Model 1*, Figure 7.10 shows that neither the *Proposed* nor the *Code Equations* were able to capture the peak demand between levels 7 and 11 in *Building Model 2*. A possible explanation about this observation is found in Section 5.2. At other levels, the *Proposed* and *Code Equations* predicted flexural effective stiffness modifiers that returned linear-elastic bending moment demands consistent with the observed nonlinear bending moments.

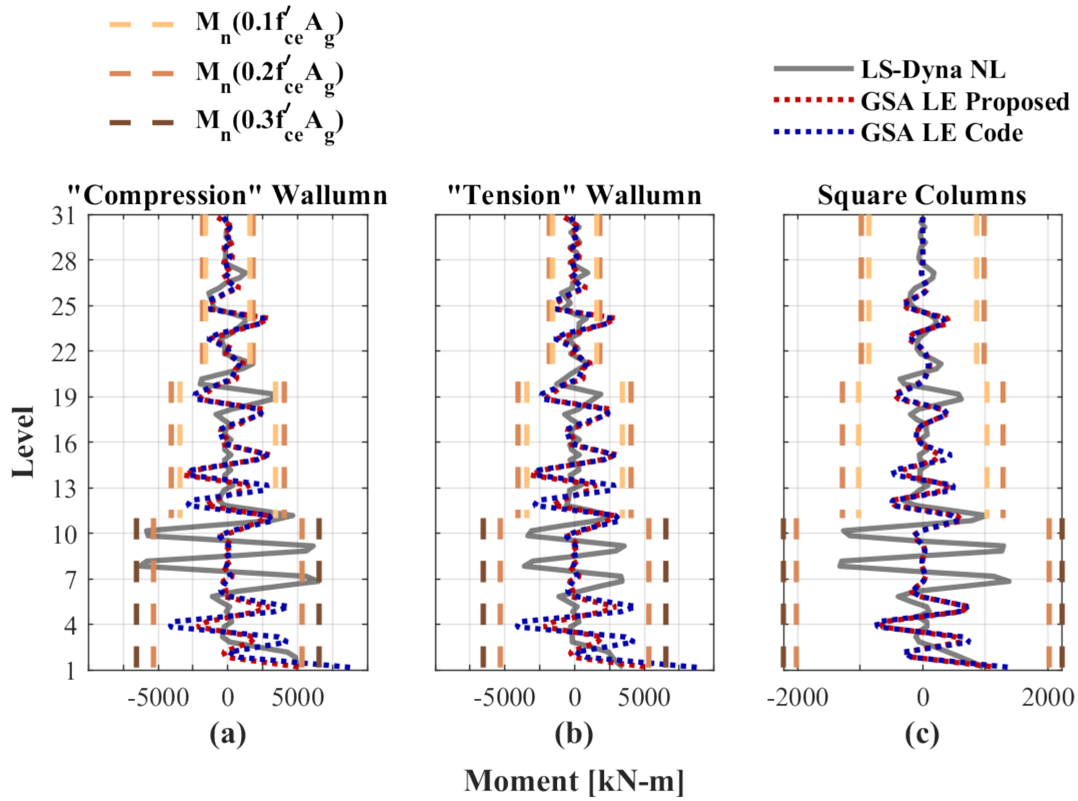

Figure 7.10 Linear-elastic *Building Model 2* demands with EI_{eff} values computed through the proposed prediction equations (red) and code equations (blue) vs nonlinear bending moment demands for columns in the cantilever direction; (a) "compression" wallumn; (b) "tension" wallumn; (c) square columns.

Figure 7.11 demonstrates that the *Proposed* and *Code Equations* estimate flexural effective stiffness values that in most of the cases return safe linear-elastic moment demands. When comparing the linear-elastic vs nonlinear peak moment demand, the *Proposed Equations* slightly underestimate the demands in the middle and bottom storeys at the "compression" outrigger wallumns and at the non-outrigger square column. *The Code Equation* results fell somewhat short at the middle and bottom storeys of the "compression" outrigger wallumns and at the middle storeys of the non-outrigger square columns. The *Proposed Equations* deficiency was 16% less in average when the peak linear-elastic-to-peak nonlinear moment demands ratios were below one. By contrast, the two occasions when the *Code Equations* returned peak linear-elastic-to-peak nonlinear moment demands ratios below one they were 5% and 29% short.

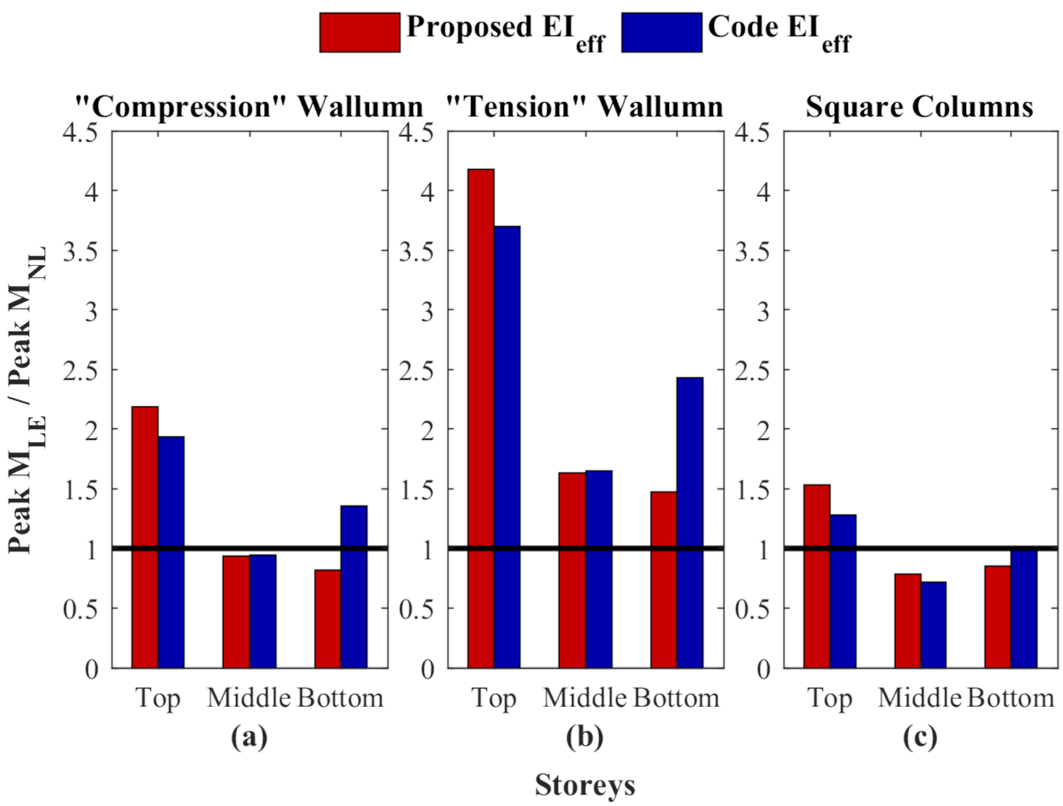

Figure 7.11 *Building Model 2* peak linear-elastic-to- peak nonlinear moment demands ratio for columns in the cantilever direction; (a) "compression" wallumn; (b) "tension" wallumn; (c) square columns.

7.3.1.2 EBW Slabs

In the *Building Model 2*, the linear-elastic EBW slabs in the cantilevered direction with flexural effective stiffness modifiers computed using the *Proposed Equations* yielded demands consistent with those of the nonlinear virtual twin, as shown in Figure 7.12. The *Code Equations* underestimated the moment demands in all EBW slabs.

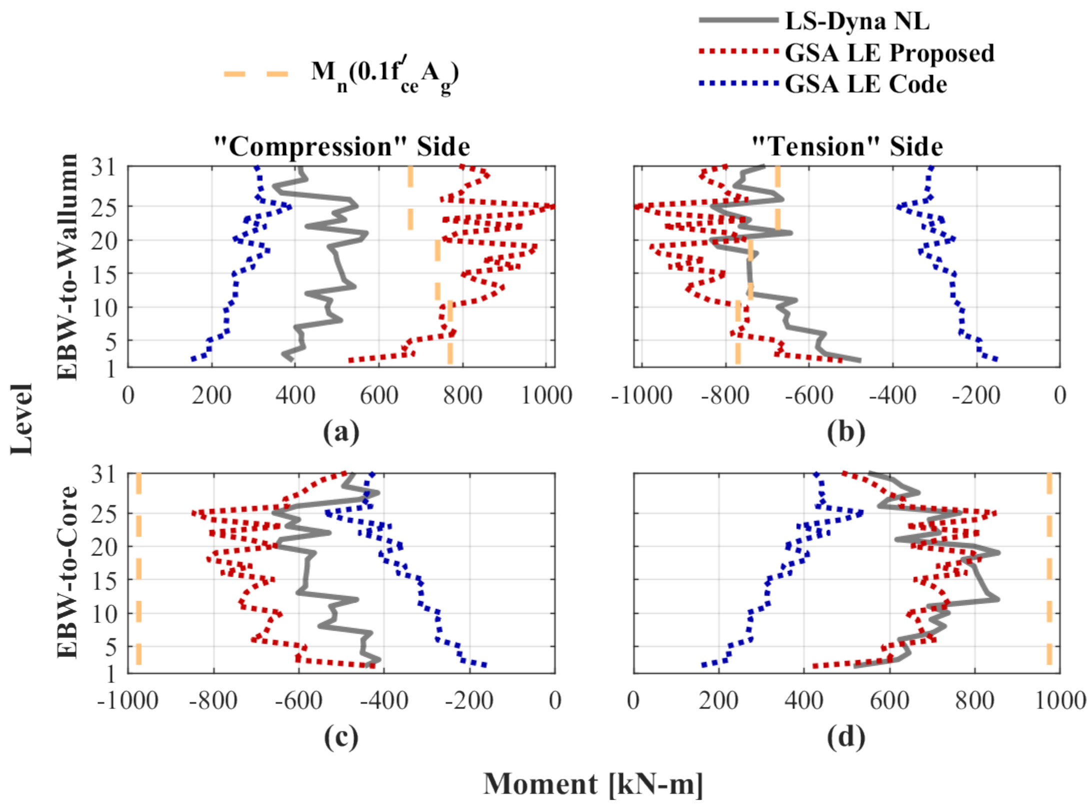

Figure 7.12 Linear-elastic *Building Model 2* demands with EI_{eff} values computed through the proposed prediction equations (red) and code equations (blue) vs nonlinear bending moment demands for EBW slabs in the cantilever direction; (a) EBW-to-wallumn "compression" side; (b) EBW-to-wallumn "tension" side; (c) EBW-to-core "compression" side; (d) EBW-to-core "tension" side.

Figure 7.13 demonstrates the good performance of the *Proposed Equations* by evaluating the peak linear-elastic-to-peak nonlinear moment demands. In all the cases, when using the flexural effective stiffness modifiers following the *Proposed Equations* the linear-elastic GFRS experiences similar demands compared to the nonlinear model. For the "compression" EBW-to-wallumn slab in the cantilevered direction, the linear-elastic demands are overestimated by 73% in average compared their nonlinear twin. By contrast, the *Code Equation* underestimates the demand in all linear-elastic EBW slabs by 18 to 62%.

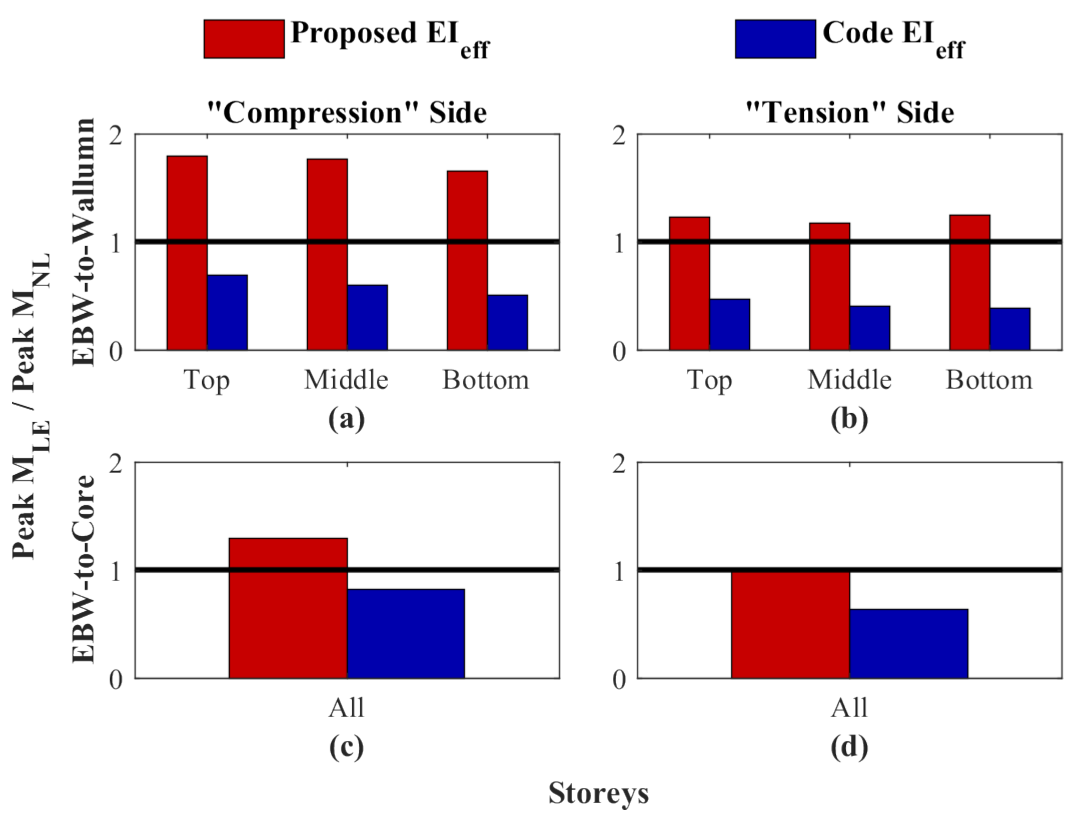

Figure 7.13 *Building Model 2* peak linear-elastic-to-peak nonlinear moment demands ratio for EBW slabs in the cantilever direction; (a) EBW-to-wallumn "compression" side; (b) EBW-to-wallumn "tension" side; (c) EBW-to-core "compression" side; (d) EBW-to-core "tension" side.

7.3.2 Coupled Direction

7.3.2.1 Columns

The *Proposed Equations* for columns in the coupled direction underestimated the bending moment at grade level. On the contrary, the *Code Equation* overestimated it, as seen in Figure 7.14. Except for levels 5 to 7, the *Proposed* and *Code Equations* predicted flexural effective stiffness modifiers that yielded the moment demand patterns consistent with the nonlinear virtual twin.

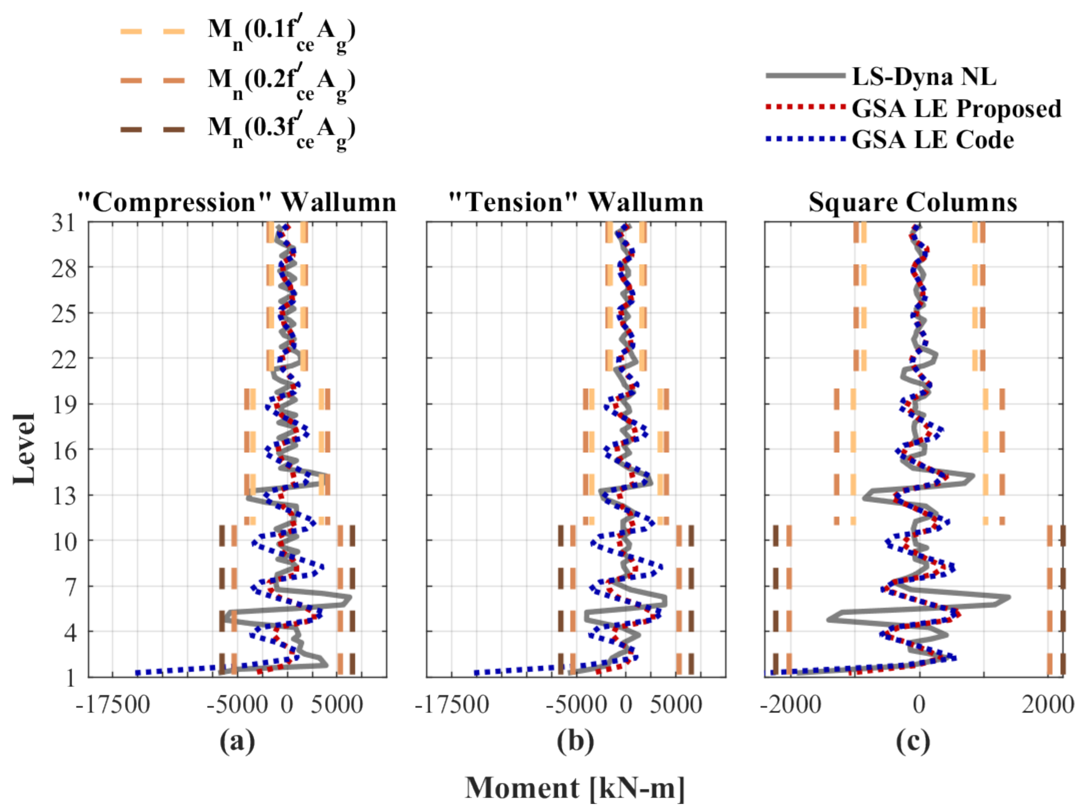

Figure 7.14 Linear-elastic *Building Model 2* demands with EI_{eff} values computed through the proposed prediction equations (red) and code equations (blue) vs nonlinear bending moment demands for columns in the coupled direction; (a) "compression" wallumn; (b) "tension" wallumn; (c) square columns.

Figure 7.15 summarizes peak linear-elastic-to-peak nonlinear ratio for columns in the coupled direction. The *Proposed Equations* failed to predict flexural effective stiffness modifiers that meet the nonlinear bending moment demand in 8 out 9 component groups. On average, they fell short by 27%. The *Code Equations* estimated effective stiffness modifiers that resulted in more consistent linear-elastic demands compared to the nonlinear model. The *Code Equations* underestimated the nonlinear demand in 3 out 9 component groups. These component groups were deficient by 15% on average.

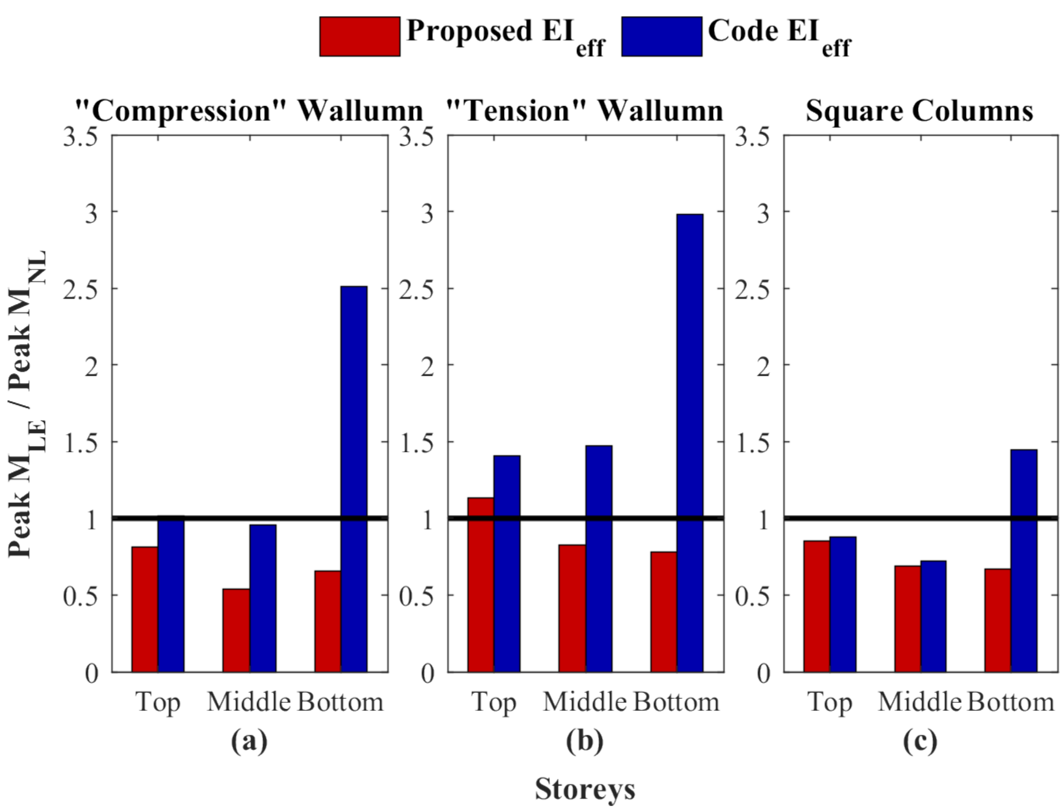

Figure 7.15 *Building Model 2* peak linear-elastic-to- peak nonlinear moment demands ratio for columns in the coupled direction; (a) “compression” wallumn; (b) “tension” wallumn; (c) square columns.

7.3.2.2 EBW slabs

Except for the upper "tension" EBW-to-wallumn slabs, the *Proposed Equations* returned appropriate flexural stiffness modifiers that yielded linear-elastic bending moments consistent with the nonlinear model, as seen in Figure 7.16. For all the EBW slabs in the "compression" side, the linear-elastic demands were overestimated, see plots (a) and (c) of Figure 7.16. The *Code* effective stiffness recommendation of 0.2 underestimated the demands in all the EBW slabs in the coupled direction.

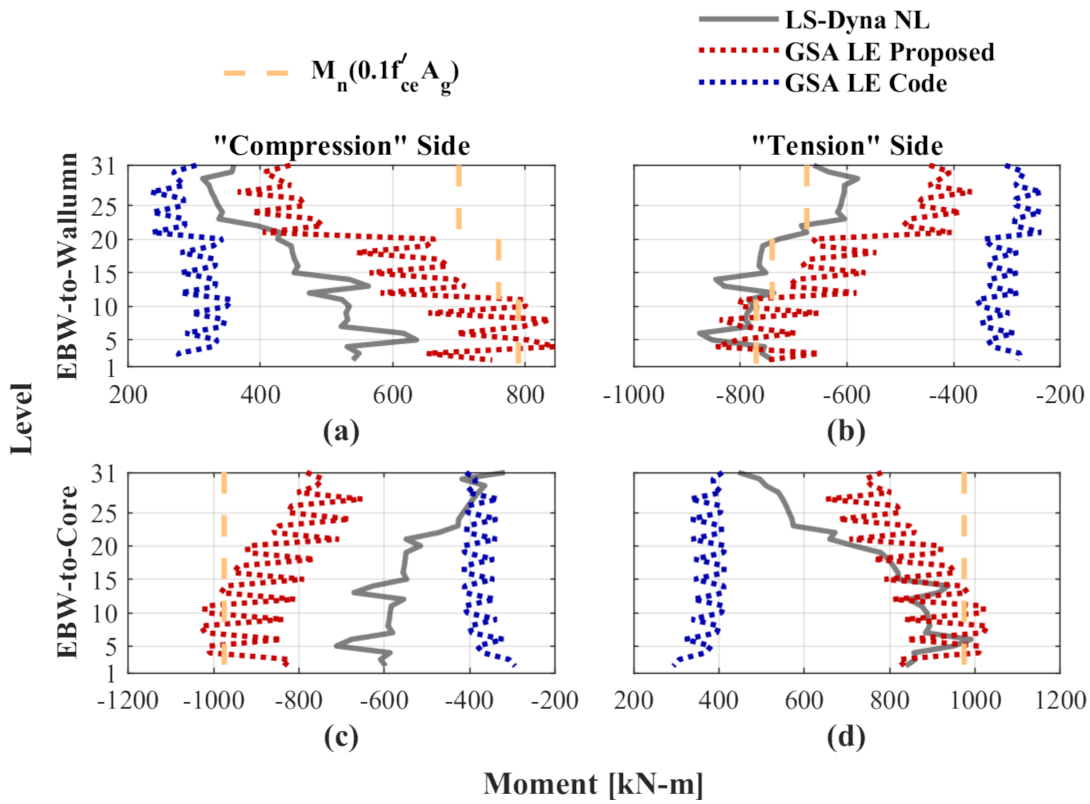

Figure 7.16 Linear-elastic *Building Model 2* demands with EI_{eff} values computed through the proposed prediction equations (red) and code equations (blue) vs nonlinear bending moment demands for EBW slabs in the coupled direction; (a) EBW-to-wallumn "compression" side; (b) EBW-to-wallumn "tension" side; (c) EBW-to-core "compression" side; (d) EBW-to-core "tension" side.

Figure 7.17 shows that the *Proposed Equations* predicted flexural effective stiffness modifiers that returned linear-elastic moment demands that are consistent with the peak nonlinear bending moment. The *Proposed Equations* for EBW slabs in the coupled direction only underestimated the demands in the EBW-to-wallumn "tension" side by 16% on average, as seen in plot (b) of Figure 7.17. By contrast, the *Code Equation* underestimated all the EBW slabs bending moment demands by 29 to 59%.

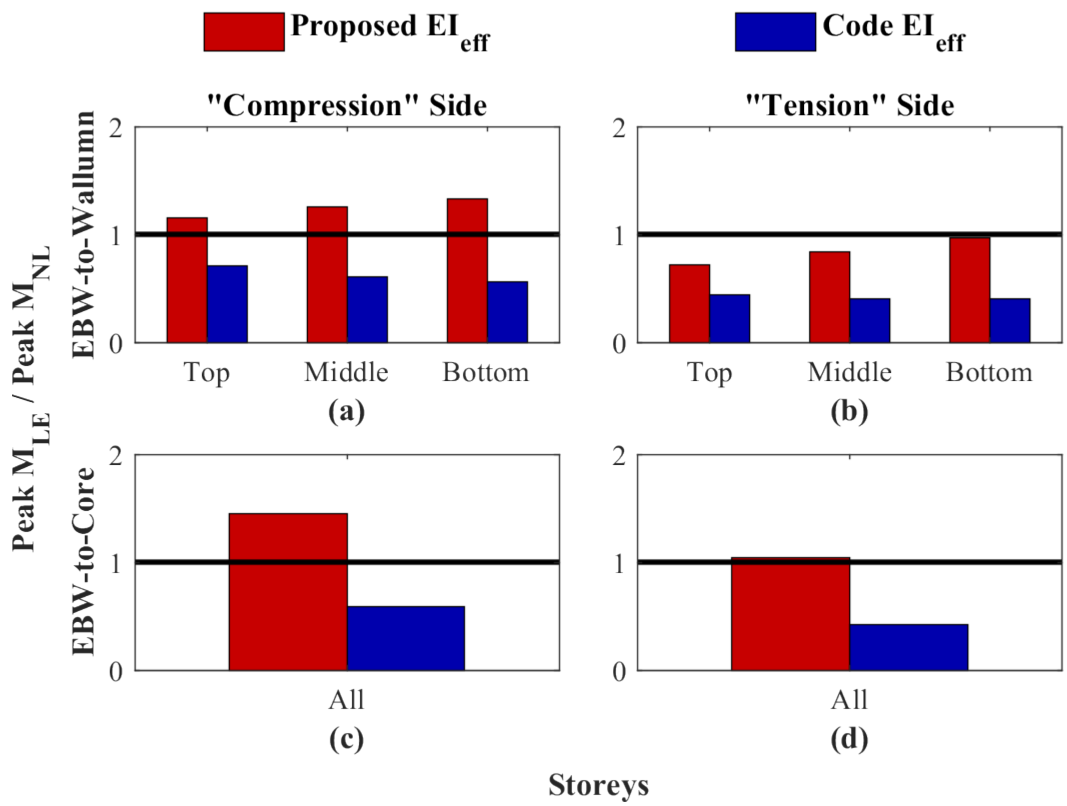

Figure 7.17 *Building Model 2* peak linear-elastic-to-peak nonlinear moment demands ratio for EBW slabs in the coupled direction; (a) EBW-to-wallumn "compression" side; (b) EBW-to-wallumn "tension" side; (c) EBW-to-core "compression" side; (d) EBW-to-core "tension" side.

7.4 GFRS Code Compliance Design

Elements of the GFRS, i.e., columns, wallumns and EBW slabs, need to satisfy the limits introduced in CSA A23.3-19 clauses § 21.11.3.3.3 and 21.11.3.3.4. These limits are given as the ratio of the induced bending moment, M_f, from the General of Simplified analysis (i.e., the drift envelope introduced in Section 2.3.1) over the factored moment resistance, M_r. The GFRS columns employed in *Building Model 1* and *2* were designed exclusively as other columns tied as compression members, refer to the last row of Table 7.3. The EBW components were designed to withstand gravity load demands only with no additional requirements, (i.e., first row of Table 7.4). Figures 7.18 through 7.25 show the ratio of the maximum absolute induced bending moment demand to factored capacity, $|M_f|/M_r$, for the component group of each gravity-frame structural element.

The maximum induced bending moment limits for gravity-columns were computed following the CSA A23.3-19 clause § 21.11.3.3.3 as shown in Table 7.3. This section intends to define the maximum seismic bending moment demand that gravity-columns can experience as a function of their axial load ratio and ductility. For intermediate values of axial compression, interpolation should be used. The maximum induced bending moment limits for the EBW components according to their seismic bending moment demands and ductility detailing are shown in Table 7.4.

With the information presented in these figures, it is possible to determine if the gravity-frame members require to comply with additional detailing requirements.

Table 7.3 Maximum induced bending moment for columns according to CSA A23.3-19 § 21.11.3.3.3

Type of Column	Axial Compression	
	$P_s \leq 0.2A_g f'_c$	$P_s > 0.4A_g f'_c$
Ductile columns satisfying clauses § 21.3.2.2, § 21.3.2.5, § 21.3.2.6, and § 21.3.2.7	$5M_r$	$3M_r$
Moderately ductile columns satisfying § 21.4.2.2, § 21.4.4, except § 21.4.4.2, and § § 21.4.5	$3M_r$	$2M_r$
Tied columns satisfying § 7.6.5 and the dimensional limitations of § 21.4.2.2	$2M_r$	$1.5M_r$
Other columns tied as compression members satisfying clause § 7.6.5 along their full length	$1.5M_r$	$1M_r$

Table 7.4 Induced bending moment limits for EBW slabs according to CSA A23.3-19 § 21.11.3.3.4

Induced Bending Moment	Beam Detailing Requirements
$< 1M_r$	No additional requirements
$\geq 1M_{r;}$ but $< 2M_r$	Limited ductility, § 21.11.3.4.2
$\geq 2M_{r;}$ but $< 3M_r$	Moderately ductile, § 21.11.3.4.3
$\geq 3M_{r;}$ but $< 5M_r$	Ductile, § 21.11.3.4.4

7.4.1 Building Model 1

7.4.1.1 Cantilever Direction

7.4.1.1.1 Columns

In Figure 7.18 plots (a) and (b), the absolute induced bending moment demand to factored capacity ratios for outrigger wallumns are 1.66, 1.38, and 2.68 for the top, middle, and bottom component groups, respectively. According to their axial load ratio and clause § 21.11.3.3.3, the maximum induced bending moment that these structural elements can experience as a function of their factored resistance is $1.5M_r$, $1.36M_r$, and $1.28M_r$ for the top, middle, and bottom component groups, respectively. Because of this, it is recommended that the top and middle components should be redesigned as tied columns (i.e., third row of Table 7.3). The bottom components should be redesigned as moderately ductile columns, refer back to the second row of Table 7.3.

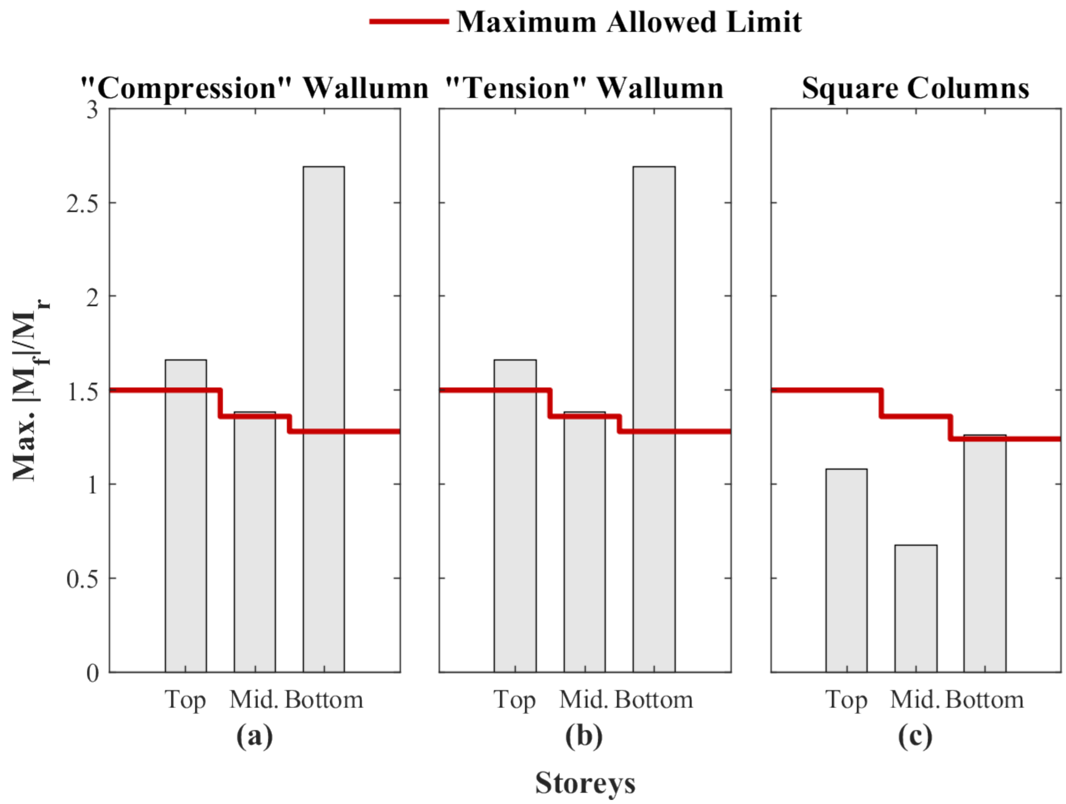

Figure 7.18 *Building Model 1* maximum induced bending moment to factored capacity ratio for columns in the cantilever direction; (a) “compression” wallumn; (b) “tension” wallumn; (c) square columns.

The absolute induced bending moment demand to factored capacity ratio for non-outrigger square columns for the top, bottom, and bottom component groups are 1.06, 0.67, and 1.25, respectively; as seen Figure 7.18 plot (c). According to their axial load ratio and clause § 21.11.3.3.3, the maximum allowed induced bending moment limits are 1.5M_r, 1.36M_r, and 1.24M_r for top, middle, and bottom storeys, respectively. Only the bottom component group exceeds its maximum allowed limit. Thus, this component group should be redesigned as a tied column following the clauses shown in the third row of Table 7.3.

7.4.1.1.2 EBW Slabs

Figure 7.19 plots (a) and (b) show the maximum $|M_f|/M_r$ ratios for EBW-to-wallumns slabs equal to 2.44, 2.33, and 2.06 for top, middle, and bottom component groups, respectively. The induced bending moment demand is larger than $2M_r$ and smaller than $3M_r$ in all group storeys. As a result, the EBW-to-wallumns slabs in the cantilever direction should be detailed as moderately ductile gravity-beams, refer to the third row of Table 7.4.

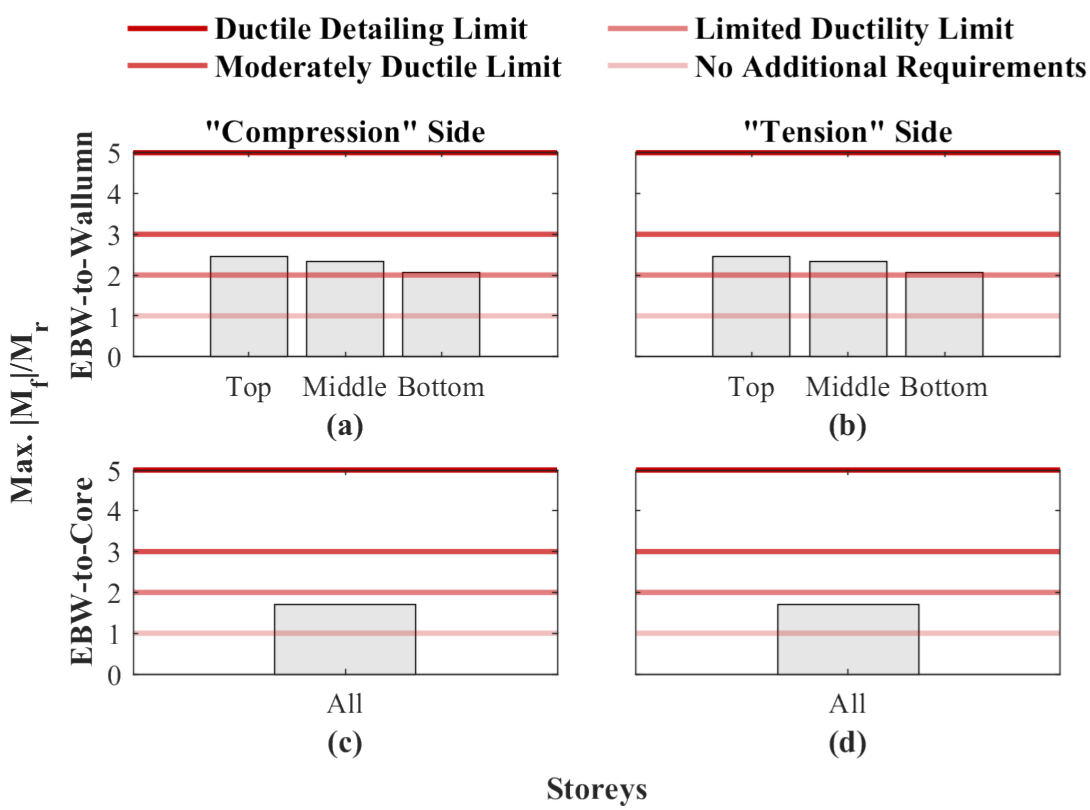

Figure 7.19 *Building Model 1* maximum induced bending moment to factored capacity ratio for EBW slabs in the cantilever direction; (a) EBW-to-wallumn “compression” side; (b) EBW-to-wallumn “tension” side; (c) EBW-to-core “compression” side; (d) EBW-to-core “tension” side.

Plots (c) and (d) of Figure 7.19 show that the EBW-to-core slabs in the cantilever ratio present an induced bending moment equal to $1.7M_r$. Since $1.0 < |M_f|/M_r < 2.0$ These EBW slabs should be designed as limited ductility beams, refer back to the second row of Table 7.4.

7.4.1.2 Coupled Direction

7.4.1.2.1 Columns

Building Model 1 outrigger wallumns in the coupled direction experience induced bending moments equal to $0.73M_r$, $0.52M_r$, and $1.88M_r$ for the top, middle, and bottom component groups, respectively; as seen in plots (a) and (b) of Figure 7.20. According to their axial load ratio and clause § 21.11.3.3.3, the maximum allowed induced bending moment limits are $1.5M_r$, $1.5M_r$, and $1.2M_r$ for top, middle, and bottom storeys, respectively. The seismic demands in the bottom outrigger wallumns are larger than the upper-bound limit bending resistance, therefore, they should be redesigned as tied columns, refer back to the third row of Table 7.3.

Figure 7.20 plot (c) shows the induced bending moment to bending resistance for non-outrigger square columns. These values are $0.54M_r$, $0.57M_r$, and $1.30M_r$ for top, middle, and bottom storeys, respectively. According to their axial load ratio and clause § 21.11.3.3.3, their maximum allowed induced bending moment limits are $1.5M_r$, $1.5M_r$, and $1.25M_r$ for top, middle, and bottom storeys, respectively. The seismic demands in the bottom outrigger wallumns are larger than the upper-bound limit bending resistance, therefore, their redesign as tied columns is required, refer back to the third row of Table 7.3.

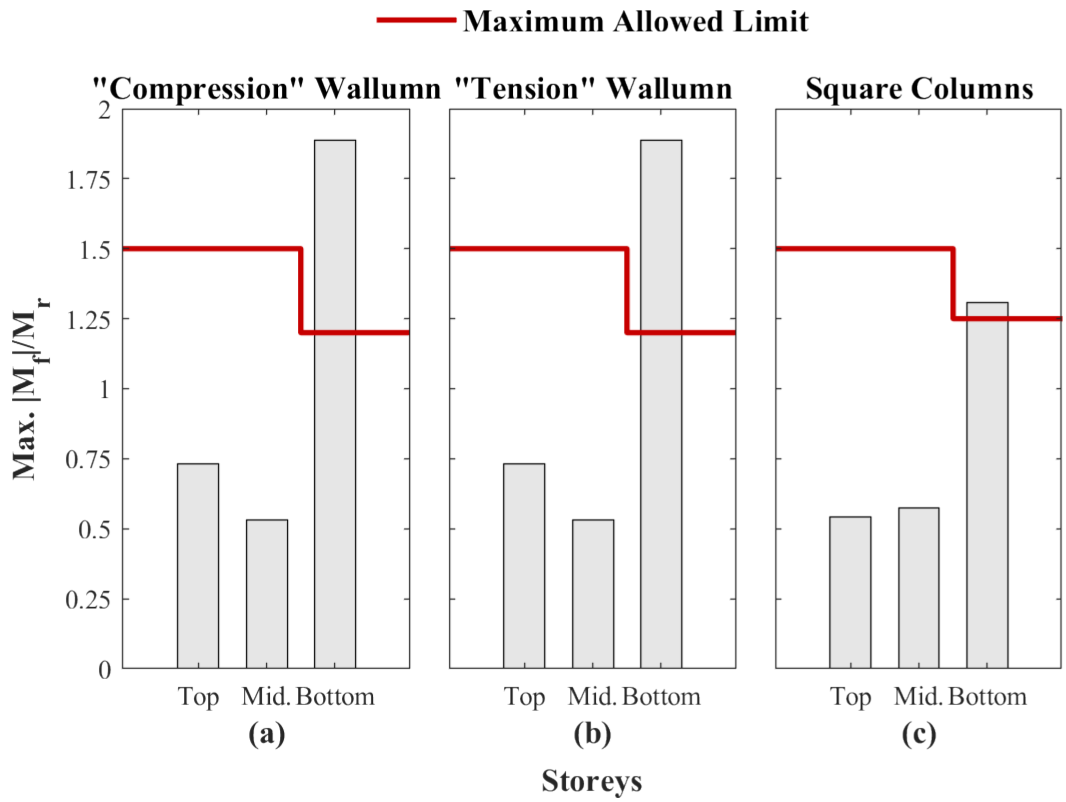

Figure 7.20 *Building Model 1* maximum induced bending moment to factored capacity ratio for columns in the coupled direction; (a) “compression” wallumn; (b) “tension” wallumn; (c) square columns.

7.4.1.2.2 EBW Slabs

Plots (a) and (b) demonstrate that the $|M_f|/M_r$ ratios for EBW-to-wallumns slabs are equal to 1.14, 1.64, and 1.94 for top, middle, and bottom component groups, respectively. The induced bending moment demand is larger than $1M_r$ and smaller than $2M_r$. Thus, the EBW-to-wallumns slabs in the coupled direction should be detailed as limited ductile gravity-beams, refer back to the second row of Table 7.4.

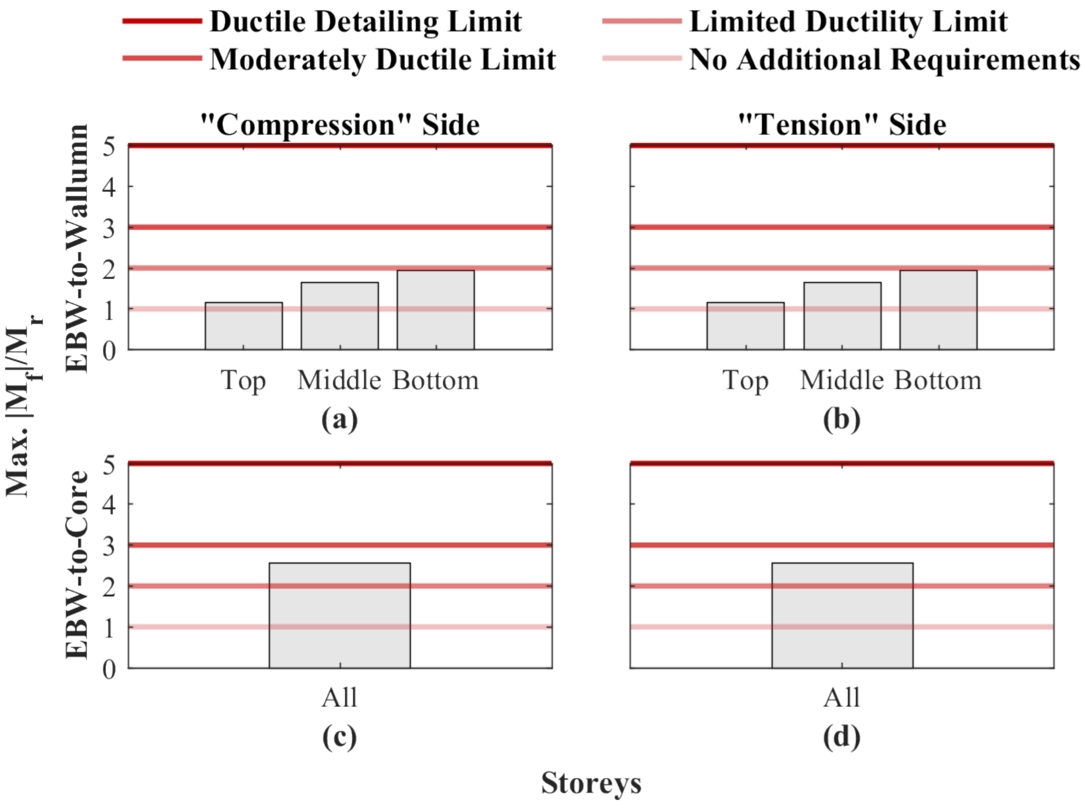

Figure 7.21 *Building Model 1* maximum induced bending moment to factored capacity ratio for EBW slabs in the coupled direction; (a) EBW-to-wallumn "compression" side; (b) EBW-to-wallumn "tension" side; (c) EBW-to-core "compression" side; (d) EBW-to-core "tension" side.

On the contrary, the EBW-to-core slabs for *Building Model 1* in the coupled direction present induced bending moments 2.56 times larger than their factored resistance. Thus, these GFRS elements need to be detailed as moderately ductile gravity-beams, refer back to the third row of Table 7.4.

7.4.2 Building Model 2

7.4.2.1 Cantilever Direction

7.4.2.1.1 Columns

In the *Building Model 2*, the outrigger wallumns in the cantilever direction present an induced bending moment demand equal to $2.42M_r$, $1.27M_r$, and $1.70M_r$ for top, middle, and bottom storeys, respectively; as seen in Figure 7.22 plots (a) and (b). According to their axial load ratio and clause § 21.11.3.3.3, the maximum allowed induced bending moment limits are $1.5M_r$, $1.45M_r$, and $1.2M_r$ for top, middle, and bottom storeys, respectively. Except for the middle component group, all outrigger wallumns in the cantilever direction need to be redesigned. The top components should be detailed as moderately ductile columns, refer back to the second row of Table 7.3. The bottom outrigger wallumn components should be redesigned as tied columns, refer back to the third row of Table 7.3.

Figure 7.22 plot (c) shows the induced bending moment to bending resistance for non-outrigger square columns. These values are $1.08M_r$, $0.67M_r$, and $1.06M_r$ for top, middle, and bottom storeys, respectively. According to their axial load ratio and clause § 21.11.3.3.3, the maximum allowed induced bending moment limits are $1.5M_r$, $1.38M_r$, and $1.25M_r$ for top, middle, and bottom storeys, respectively. The seismic demands are less than the upper-bound limit bending resistance, therefore, no redesign is required.

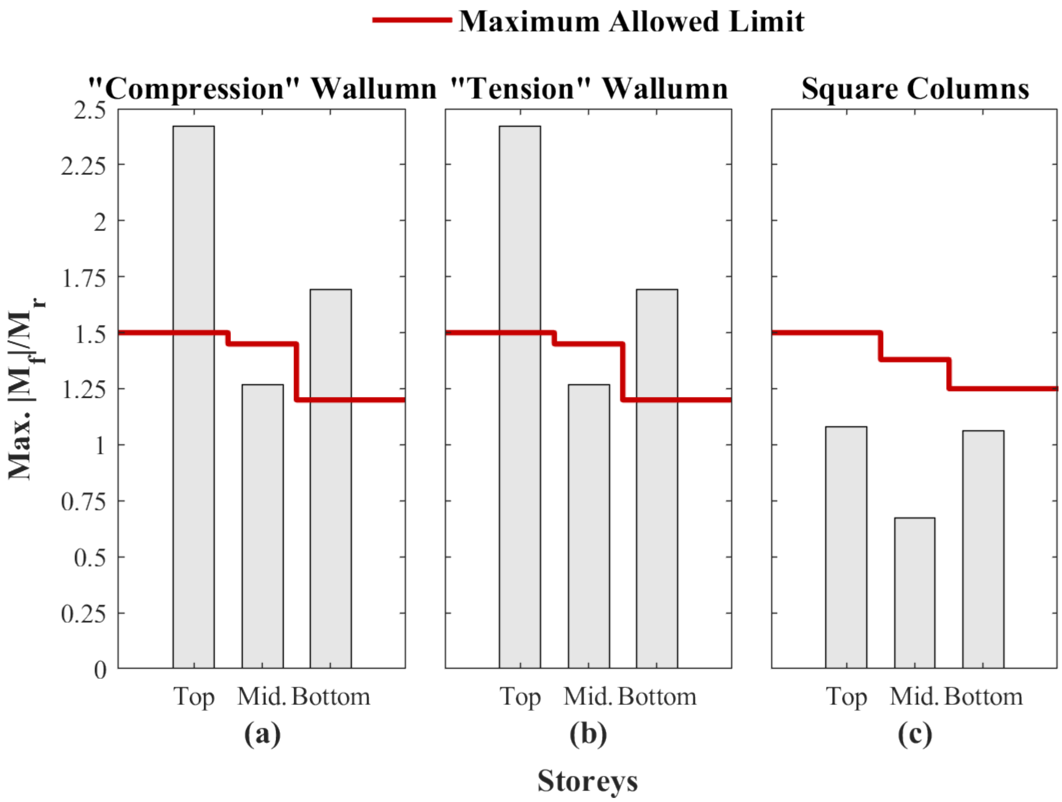

Figure 7.22 *Building Model 2* maximum induced bending moment to factored capacity ratio for columns in the cantilever direction; (a) “compression” wallumn; (b) “tension” wallumn; (c) square columns.

7.4.2.1.2 EBW Slabs

In Figure 7.23 plots (a) and (b), the EBW-to-wallumn slabs induced bending moment demands are equal to 3.4M_r, 3.26M_r, and 2.8M_r for top, middle, and bottom storeys, respectively. Thus, the top and middle EBW-to-wallumn slabs in the cantilever direction will need to be detailed as ductile EBW gravity slabs, refer back to the fourth row of Table 7.4. The bottom EBW-to-wallumn slabs should be redesigned as moderately ductile gravity, refer back to the third row of Table 7.4.

The EBW-to-core slabs induced bending moment ratio is equal to 1.77M_r for all the levels, as seen in Figure 7.24 plots (c) and (d). With this amount of inelastic flexural deformation, the EBW-to-core slabs should be detailed as limited ductility, refer back to the second row of Table 7.4.

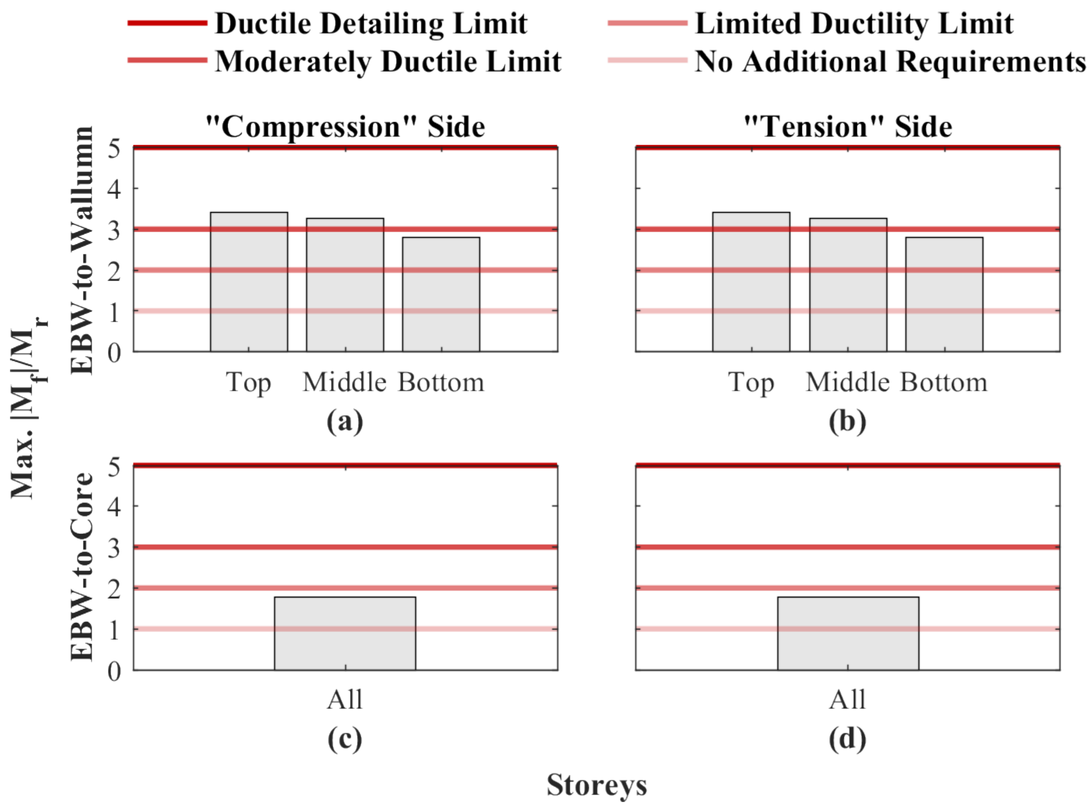

Figure 7.23 *Building Model 2* maximum induced bending moment to factored capacity ratio for EBW slabs in the cantilever direction; (a) EBW-to-wallumn "compression" side; (b) EBW-to-wallumn "tension" side; (c) EBW-to-core "compression" side; (d) EBW-to-core "tension" side.

7.4.2.2 Coupled Direction

7.4.2.2.1 Columns

In Figure 7.24 plots (a) and (b) the outrigger wallumns in the coupled direction experience an induced bending moment demand equal to $0.73M_r$, $0.54M_r$, and $1.26M_r$ for top, middle, and bottom storeys, respectively. According to their axial load ratio and clause § 21.11.3.3.3, the maximum allowed induced bending moment limits are $1.5M_r$, $1.5M_r$, and $1.13M_r$ for top, middle, and bottom storeys, respectively. Thus, only the bottom outrigger wallumns in the coupled direction need to be redesigned as tied columns, refer back to the third row of Table 7.3.

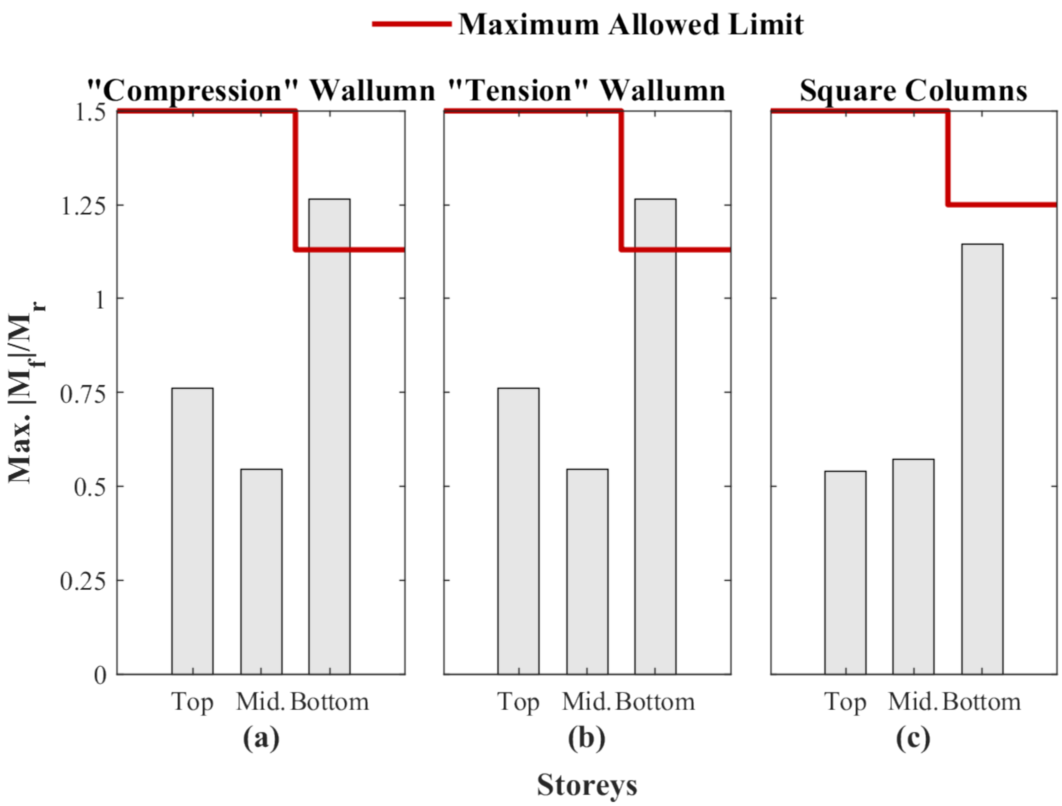

Figure 7.24 *Building Model 2* maximum induced bending moment to factored capacity ratio for columns in the coupled direction; (a) "compression" wallumn; (b) "tension" wallumn; (c) square columns

Figure 7.24 plot (c) shows the induced bending moment to bending resistance for square columns. These values are $0.54M_r$, $0.57M_r$, and $1.20M_r$ for top, middle, and bottom storeys, respectively. According to their axial load ratio and clause § 21.11.3.3.3, the maximum allowed induced bending moment limits are $1.5M_r$, $1.5M_r$, and $1.25M_r$ for top, middle, and bottom storeys, respectively. The seismic demands are less than the upper-bound limit bending resistance, therefore, no redesign is required.

7.4.2.2.2 EBW Slabs

In Figure 7.25 plots (a) and (b) the EBW-to-wallumn slabs induced bending moment demands are equal to $1.49M_r$, $2.15M_r$, and $2.56M_r$ for top, middle, and bottom storeys, respectively. Thus, the top EBW-to-wallumn slabs in the coupled direction will need to be detailed as limited ductility EBW gravity slabs, refer back to the second row of Table 7.4. The middle and bottom EBW-to-wallumn slabs should be redesigned as moderately ductile gravity slabs, refer back to the third row of Table 7.4.

The EBW-to-core slabs induced bending moment ratio is equal to $2.64M_r$ for all the levels, see Figure 7.25 plots (c) and (d). With this amount of inelastic flexural deformation, the EBW-to-core slabs should be detailed as moderately ductile elements, refer back to the third row of Table 7.4.

.

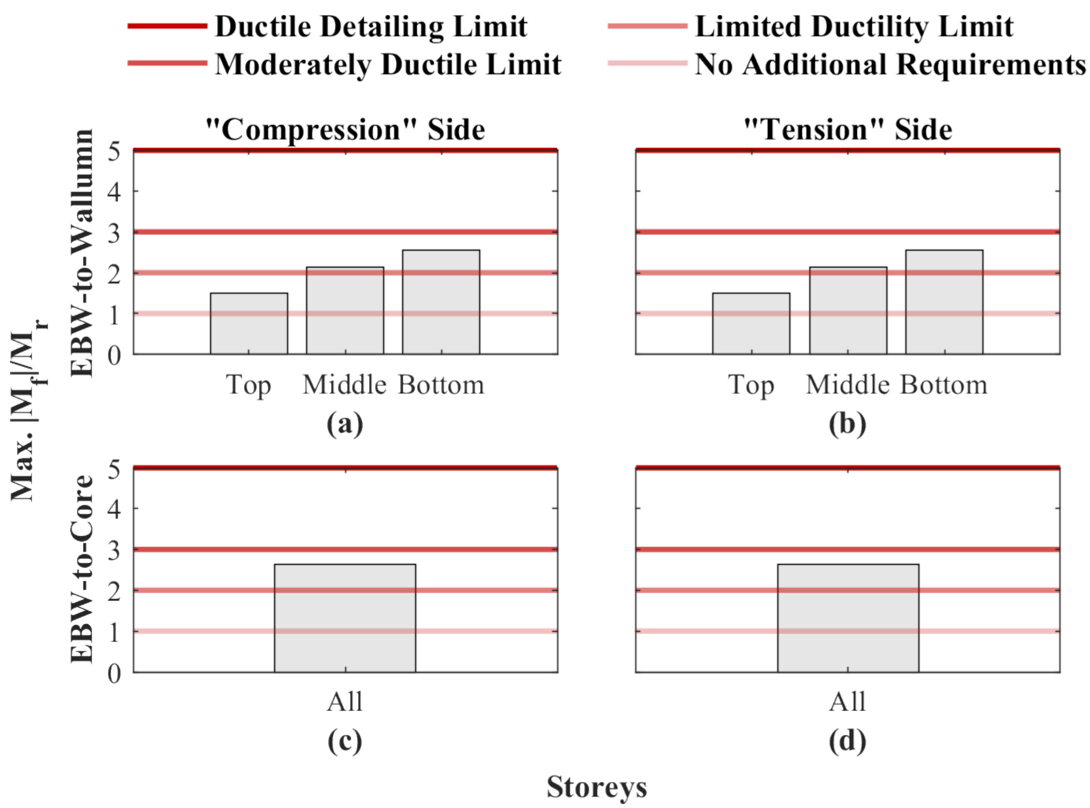

Figure 7.25 *Building Model 2* maximum induced bending moment to factored capacity ratio for EBW slabs in the coupled direction; (a) EBW-to-wallumn "compression" side; (b) EBW-to-wallumn "tension" side; (c) EBW-to-core "compression" side; (d) EBW-to-core "tension" side

With the exception of the bottom square columns in *Building Model 1*, it was found that the non-outrigger square columns do not need to be redesigned. In *Building Model 1* and *2* the bottom outrigger wallumns in the coupled direction needed to be redesigned as tied columns. For both *Building Model 1* and *2*, the outrigger wallumns in the cantilevered direction had to be redesigned in at least two of the group components. Additionally, at least one group component needs to be detailed as a moderately ductile column. Last, all EBW components need to have any sort of additional ductile detailing. As described earlier in Section 2.2, it is not uncommon in the US practice to detail all the GFRS components as ductile elements. The Simplified Analysis of CSA

A23.3-19 clause 21.11.2.2 shows that ductile detailing is required at some gravity-frame locations, but not everywhere. Thus, the CSA A23.3-19 approach might result in cost savings if the structural designer is strategic about the amount of seismic detailing that goes into each GFRS component.

Chapter 8: Summary of Contributions, Conclusions, Limitations, and Recommendations for Future Work

This thesis aimed to develop flexural effective stiffness modifiers for the GFRS components of RCSW buildings to estimate their seismic demands following the General or Simplified Analysis procedures of CSA A23.3-19. This analysis was carried out after completing the gravity design of the GFRS to assess if the columns, wallumns and slabs that do not belong to the SFRS system have adequate strength and ductility to accommodate lateral earthquake demands. Generalized equations were proposed to estimate the flexural effective stiffness modifiers of these elements for use in the General or Simplified Analysis procedure described in clauses § 21.11.2.1 and § 21.11.2.2 of CSA.A23.3-19, respectively.

8.1 Summary of Contributions

This is the first time a study aimed at to provide estimates on the flexural effective stiffness factors for elements of the GFRS in RCSW buildings for implementation in the General or Simplified Analysis procedure described in clauses § 21.11.2.1 and § 21.11.2.2 of CSA.A23.3-19, respectively. Other methods (Beauchamp et al., 2017; Choinière et al., 2019) have been proposed to estimate seismic demands in the GFRS via alternate means. However, they do not support the implementation of the CSA A23.3-19 General or Simplified Analysis clause, i.e., no values are provided to account for concrete cracking in the GFRS. This study spearheads the quantification of flexural effective stiffness modifiers in the gravity-frame system, making it possible to satisfy all the requirements of the General and Simplified Analysis requirements to check if the GFRS can accommodate lateral demands. This allows structural engineers to implement this check in their designs following a linear-elastic analysis of the entire structure (SFRS and GFRS).

In general, the *Proposed* prediction equations deliver appropriate effective flexural stiffness modifiers reducing the uncertainty around realistic stiffness values of GFRS members. The *Proposed Equations* provide a new tool to approximate the level of cracking in RC gravity frames, which makes a complete code-prescribed building analysis possible. With this, the Structural Engineer of Record will be able to document the code compliance of the full building system, as opposed to carry out isolated member checks.

8.2 Conclusions

Regardless of the GFRS cross-section, the *Proposed Equations* for gravity-frame columns and EBW slabs in the cantilever direction provided flexural effective stiffness factors for use in linear-elastic analysis that returned consistent bending moment demands compared to their nonlinear virtual twin. The *Proposed Equation* for EBW slabs in the coupled direction also provided safe estimates of the seismic moment demands. By contrast, the *Code Equation* is as good or better than the *Proposed Equation* for columns in the coupled direction by providing more realistic estimates of linear-elastic moment demands.

The *Code Equation* for columns in the cantilevered direction yielded similar demands to the *Proposed Equations*. Both sets of equations were in good agreement with the nonlinear values and provided accurate estimates of moment demands with flexural effective stiffness modifiers in the [50-69%] and [10-100%] range, respectively.

The *Proposed Equations* for the EBW slabs in the cantilevered direction returned flexural effective stiffness modifiers that result in consistent linear-elastic demands compared to their nonlinear counterpart with stiffness modifiers in the 22 to 90% range. On average, the peak linear-elastic to nonlinear moment demand ratio was about 1.3. The *Code Equation*, which results in a flexural effective stiffness value of 20%, returned moment demands 21 to 62% smaller in all the gravity-frame EBW slabs. Therefore, the current simplifying assumption, which is common in design practice, that assigns an out-plane flexural stiffness value between 10%-25% could lead to non-conservative estimates of seismic demands.

For the columns in the coupled direction, the *Code Equation,* which assigns a flexural effective stiffness modifier of 50 to 69% provided safer bending moment estimates for all column types. At the bottom storeys, the *Proposed Equations* predicted flexural effective stiffness modifiers that resulted in linear-elastic moment demands values closer to the nonlinear demands than the *Code Equation*. However, the *Proposed Equations* failed to meet the maximum observed nonlinear demand. Both sets of equations slightly underestimated the demand at the top and middle storeys for the "compression" outrigger wallumn and non-outrigger square columns. When the *Proposed* and *Code Equations* fell short, on average they underestimated the demands by 25% and 19%, respectively.

As well as with the EBW slabs in the cantilevered direction, the *Proposed Equations* for slabs in the coupled direction provided appropriate flexural effective stiffness estimates that yielded accurate linear-elastic demands with stiffness modifiers in the 28 to 62% range. By contrast, the peak linear-elastic to nonlinear moment demand ratios associated with the *Code Equation* fell short by 29 to 60%.

The analysis results suggested that the EBW slabs cracked less than is typically assumed in design practice. This was caused by the axial elongation effect, which induced compressive forces in these indeterminate elements once they cracked, resulting in less out-of-plane flexibility.

The Simplified Analysis drift profiles exert a double or single curvature in the column elements depending on their position along the building's height. The cantilevered drift profile develops the largest column moment demands around 1/3 of the building's height. The coupled drift profile causes the largest moment column demands at grade and in the lower storeys.

8.3 Limitations and Recommendations for Future Work

The flexural effective stiffness modifiers recommendations are based in a single SFRS and GFRS design. As a result, the *Proposed Equations* may not return appropriate flexural effective stiffness modifiers for other building configurations. The intent of developing the flexural effective stiffness prediction equations, is to expand the applicability of this study to other buildings in future studies. Even though the *Proposed Equations* provided appropriate flexural stiffness when the GFRS was modified in *Building Model 2*, further refinements of these equations can de made. Different sizes of columns and slabs should be evaluated to increase the range of validity of the regression models. The effect of distance from the outrigger wallumns to the core still needs to be assessed, and multiple building configurations with different RCSW cross-section dimensions need to be explored.

The *Proposed Equations* were obtained without considering the foundation movement effect in the drift profile. Depending on the foundation type, soil, and structural system, this effect could significantly increase the drift applied to the gravity frames. To improve the estimation of the flexural stiffness modifiers, soil-structure interaction effects should be considered.

Transfer slabs are commonly used in RCSW buildings in Western Canada to provide commercial spaces at the ground level. The *Proposed Equations* are not meant for this type of building configuration. A different analysis, which considers this structural feature, should be developed to obtain the stiffness factors for transfer slabs.

In this study only the flexural effective stiffness modifier was assessed, i.e., it only provides guidance on the moment demands at the GFRS components. To obtain the seismic shear demands in the gravity frame, accurate shear stiffness factors are required. If the GFRS fails, a ductile failure mode is desired. For this reason, the estimation of realistic moment demands is critical to provide the right seismic detailing for the GFRS component according to CSA A23.3-19 clauses § 21.11.3.3.3 and 21.11.3.3.4. Because brittle shear failures should be avoided, the shear stiffness assumed in the analysis of gravity frame members was 100%.

The axial load ratio of EBW observed in the analysis ($0.1A_gf'_c$ to $0.2A_gf'_c$), which was caused by the axial elongation of these components is consistent with other experimental (Zerbe & Durrani, 1989) and analytical (Kim et al., 2004) studies. However, further studies need to be carried out to assess the impact of the axial load observed in the EBWs and in their flexural stiffness as they are higher than what is assumed in design practice.

References

Abrams, D. P., & Sozen, M. A. (1979). *Experimental Study of Frame Wall Interaction in Reinforced Concrete Structures Subjected to Strong Earthquake Motions.* Urbana, IL: University of Illinois at Urban-Champaign.

ACI (American Concrete Institute). (2019). *Building code requirements for structural concrete.* ACI 318-19, Farmington Hills, MI: ACI.

Adebar, P., Bazargani, P., Mutrie, J., & Mitchell, D. (2010). Safety of gravity-load columns in shear wall buildings designed to Canadian standard CSA A23. 3. *Canadian Journal of Civil Engineering, 37*(11), 1451-1461. doi:10.1139/L10-075

Adebar, P., DeVall, R., & Mutrie, J. G. (2014). Design of Gravity-load Resisting Frames for Seismic Displacement Demands. *Proceedings of the 10th National Conference in Earthquake Engineering*.

Anderson, D. R., Sweeney, D. J., & Williams, T. A. (2010). *Statistics for business and economics.* Mason, OH: South-Wester .

Arup. (2021). *Structural analysis and design software - GSA suite.* London, UK: Arup.

Bazargani, P. (2014). *Seismic demands on gravity-load columns of reinforced concrete shear wall buildings.* (Doctoral Dissertation). The University of British Columbia. doi:10.14288/1.0167436

Beauchamp, J., Paultre, P., & Léger, P. (2017). A simple method for determining seismic demands on gravity load frames. *Canadian Journal of Civil Engineering, 44*(8), 661-673. doi:10.1139/cjce-2016-0034

Benzoni, G., Ohtaki, T., Priestley, M. J., & Seible, F. (1996). *Seismic Performance of Circular Reinforced Concrete Columns under Varying Axial Load.* SSRP 96/04, La Jolla, CA: University of California-San Diego.

Chatterjee, S., & Hadi, A. S. (2006). *Regression Analysis by Example* (4th ed.). Hoboken, NJ: John Wiley & Sons.

Choinière, M., Paultre, P., & Leger, P. (2019). Influence of soil-structure interaction on seismic demands in shear wall building gravity load frames. *Engineering Structures*, 109259. doi:10.1016/j.engstruct.2019.05.100

Collins, M. P., & Mitchell, D. (1987). *Prestressed concrete basics.* Ottawa, ON: Canadian Prestressed Concrete Institute.

CSA (Canadian Standards Association). (2009). *Carbon steel bars for concrete reinforcement.* CSA G30.18-09. Toronto, ON: CSA.

CSA (Canadian Standards Association). (2014). *Design of concrete structures.* A23.3-14. Toronto, ON: CSA.

CSA (Canadian Standards Association). (2019). *Design of concrete structures.* A23.3-19, Toronto, ON: CSA.

Devore, J. L. (2011). *Probability and Statistics for Engineering and the Sciences* (8th ed.). Boston, MA: Cengage Learning.

Eksir Monfared, A. (2020). *Georgia sedimentary basin effects on the response of modern tall RC shear wall buildings to M9 Cascadia subduction zone earthquakes.* (Master's thesis). The University of British Columbia. doi:10.14288/1.0392918

Eksir Monfared, A., Molina Hutt, C., Kakoty, P., Kourekpaz, P., & Centeno, J. (2021). Effects of the Georgia Sedimentary Basin on the Response of Modern Tall RC Shear-Wall

Buildings to M9 Cascadia Subduction Zone Earthquakes. *Journal of Structural Engineering, 147*(8), 05021003. doi:10.1061/(ASCE)ST.1943-541X.0003067

Elwood, K. J. (2013). Performance of concrete buildings in the 22 February 2011 Christchurch earthquake and implications for Canadian codes. *Canadian Journal of Civil Engineering, 40*(3), 759-776. doi:10.1139/cjce-2011-0564

Elwood, K. J., & Eberhard, M. O. (2009). Effective stiffness of reinforced concrete columns. *ACI Structural Journal, 106*(4), 476-484. doi:10.14359/56613

Fenwick, R. C., & Megget, L. M. (1993). Elongation and load deflection characteristics of reinforced concrete members containing plastic hinges. *Bulletin of the New Zealand Society for Earthquake Engineering, 26*(1), 28-41. doi:10.5459/bnzsee.26.1.28-41

Hibbeler, R. C. (2011). *Mechanics of materials* (8th ed.). Boston: Prentice Hall.

Hughes, T. J., & Liu, W. K. (1981a). Nonlinear finite element analysis of shells: Part I. Three-dimensional shells. *Computer methods in applied mechanics and engineering, 26*(3), 331-362. doi:10.1016/0045-7825(81)90121-3

Hughes, T. J., & Liu, W. K. (1981b). Nonlinear finite element analysis of shells-part II. two-dimensional shells. *Computer Methods in Applied Mechanics and Engineering, 27*(2), 167-181. doi:10.1016/0045-7825(81)90148-1

Hwang, S. J., & Moehle, J. P. (2000). Models for Laterally Loaded Slab-Column Frames. *ACI Structural Journal, 97*(2), 345-352. doi:10.14359/866

Hyland. (2012). *CTV Building Collapse Investigation.* Auckland, N.Z.

Karthik, M. M., & Mander, J. B. (2011). Stress-block parameters for unconfined and confined concrete based on a unified stress-strain model. *Journal of Structural Engineering, 137*(2), 270-273. doi:10.1061/(ASCE)ST.1943-541X.0000294

Kim, J., Stanton, J., & MacRae, G. (2004). Effect of Beam Growth on Reinforced Concrete Frames. *Journal of Structural Engineering, 130*(9), 1333-1342. doi:10.1061/(ASCE)0733-9445(2004)130:9(1333)

Kono, S., Bechtoula, H., Sakashita, M., Tanaka, H., Watanabe, F., & Eberhard, M. O. (2006). Damage assessment of reinforced concrete columns under high axial loading. *ACI Special Publication, 237*, 165-176.

Lignos, D. G., & Krawinkler, H. (2011). Deterioration modeling of steel components in support of collapse prediction of steel moment frames under earthquake loading. *Journal of Structural Engineering, 137*(11), 1291-1302. doi:10.1061/(ASCE)ST.1943-541X.000037

Los Angeles Tall Buildings Structural Design Council (LATBSDC). (2020). *An alternative procedure for seismic analysis and design of tall buildings.* LA, CA: Los Angeles Tall Buildings Structural Design Council .

LSTC. (2020). *General-purpose finite element program.* Livermore, CA: Livermore Software Technology Corp.

MacLeod, I. A. (1971). *Shear Wall-frame Interaction: A Design Aid.* (SP011 .O1 D). Skokie, IL: Portland Cement Association.

Mander, J. B., Priestley, M. J., & Park, R. (1988). Theoretical stress-strain model for confined concrete. *Journal of structural engineering, 114*(8), 1804-1826. doi:10.1061/(ASCE)0733-9445(1988)114:8(1804)

Marafi, N. A., Makdisi, A. J., Eberhard, M. O., & Berman, J. (2020). Impacts of an M9 Cascadia subduction zone earthquake and Seattle basin on performance of RC core wall buildings. *Journal of Structural Engineering, 146*(2). doi:10.1061/(ASCE)ST.1943-541X.0002490

Massicotte, B., Elwi, A. E., & MacGregor, J. G. (1990). Tension-stiffening model for planar reinforced concrete members. *Journal of Structural Engineering, 116*(11), 3039-3058. doi:10.1061/(ASCE)0733-9445(1990)116:11(3039)

MATLAB. (2021). *version 9.11.0. (R2021b).* Natick, MA: The MathWorks Inc.

Metro Vancouver. (2018). *Metro Vancouver Growth Projections – A Backgrounder.* Vancouver, BC: Metro Vancouver. Retrieved from http://www.metrovancouver.org/services/regional-planning/data-statistics/projecting-growth/Pages/default.aspx

Ministry for Culture and Heritage. (2021, February 22). CTV building collapse. New Zealand. Retrieved from https://nzhistory.govt.nz/media/photo/ctv-building-collapse

Mitchell, D., DeVall, R. H., Saatcioglu, M., Simpson , R., Tinawi, R., & Tremblay, R. (1995). Damage to concrete structures due to the 1994 Northridge earthquake. *Canadian Journal of Civil Engineering, 22*(2), 361-377. doi:10.1139/l95-047

NRC (National Research Council Canada). (2015). *National Building Code of Canada. NBC 2015.* Ottawa, ON.

Paulay, T. (2001). A Re-definition of the Stiffness of Reinforced. *Structural Engineering International, 11*(1), 36-41. doi:10.2749/101686601780324287

Paulay, T., & Priestley, M. J. (1992). *Seismic Design of Reinforced and Masonry Buildinigs.* New York, NY: John Wiley and Sons.

Paultre, P., Légeron, F., & Mongeau, D. (2001). Influence of concrete strength and transverse reinforcement yield strength on behavior of high-strength concrete columns. *ACI Structural Journal, 98*(4), 490-501. doi:10.14359/10292

PEER (Pacific Earthquake Engineering Research Center). (2017). *Guidelines for performance-based seismic design of tall buildings.* Berkeley, CA: Pacific Earthquake Engineering Research Center. Retrieved from https://peer.berkeley.edu/research/building-systems/tall-buildings-initiative

Priestley, M. J. (1998). Brief comments on elastic flexibility of reinforced concrete frames and significance to seismic design. *Bulletin of the New Zealand Society for Earthquake Engineering, 31*(4), 246-259. doi:10.5459/bnzsee.31.4.246-259

Priestley, M. J. (2003). *Myths and fallacies in earthquake engineering, revisited: The ninth mallet Milne lecture.* Pavia, Italy: IUSS press.

Saatcioglu, M., & Ozcebe, G. (1989). Response of reinforced concrete columns to simulated seismic loading. *ACI Structural Journal, 86*(1), 3-12. doi:10.14359/2607

Sadeghian, P., & Fam, A. (2015). Improved design-oriented confinement models for FRP-wrapped concrete cylinders based on statistical analyses. *Engineering Structures, 87*, 162-182. doi:10.1016/j.engstruct.2015.01.024

Sakata, H., Hayashi, S., Wada, A., & Kokusho, S. (1987). AN EXPERIMENTAL STUDY ON ELASTIC AND PLASTIC BEHAVIORS OF REINFORCED CONCRETE BEAM IN CONSIDERATION AXIAL RESTRICTION EFFECT OF DEFORMATION. *Journal of Structural and Construction Engineering (Transactions of AIJ), 380*(0), 45-55. doi:10.3130/aijsx.380.0_45

Spacone, E., Filippou, F. C., & Taucer, F. F. (1996). Fibre beam–column model for non-linear analysis of R/C frames: part II. Applications. *Earthquake engineering & structural dynamics, 25*(7), 727-742. doi:10.1002/(SICI)1096-9845(199607)25:7<727::AID-EQE577>3.0.CO;2-O

Watson, S., Zahn, A. F., & Park, R. (1994). Confining reinforcement for concrete columns. *Journal of Structural Engineering, 120*(6), 1798-1824. doi:10.1061/(ASCE)0733-9445(1994)120:6(1798)

Zerbe, H. E., & Durrani, A. J. (1989). Seismic Response of Connections in Two-Bay R/C Frame Subassemblies. *Journal of Structural Engineering, 115*(11), 2829-2844. doi:10.1061/(ASCE)0733-9445(1989)115:11(2829)

Appendices

Appendix A Drift Profile Effect on the Curvature of GFRS Columns

From Section 2.6.1, it was inferred that the Simplified Analysis displacement profiles for the cantilever and coupled walls is one of the reasons to observe either single or double curvature in the GFRS columns. To check this, the cantilever direction of the nonlinear building was first displaced following the cantilever drift profile seen in A.1. Later, the coupled direction of the same building was subjected to the cantilever drift profile. The normalized moment demand throughout the building's height was plotted.

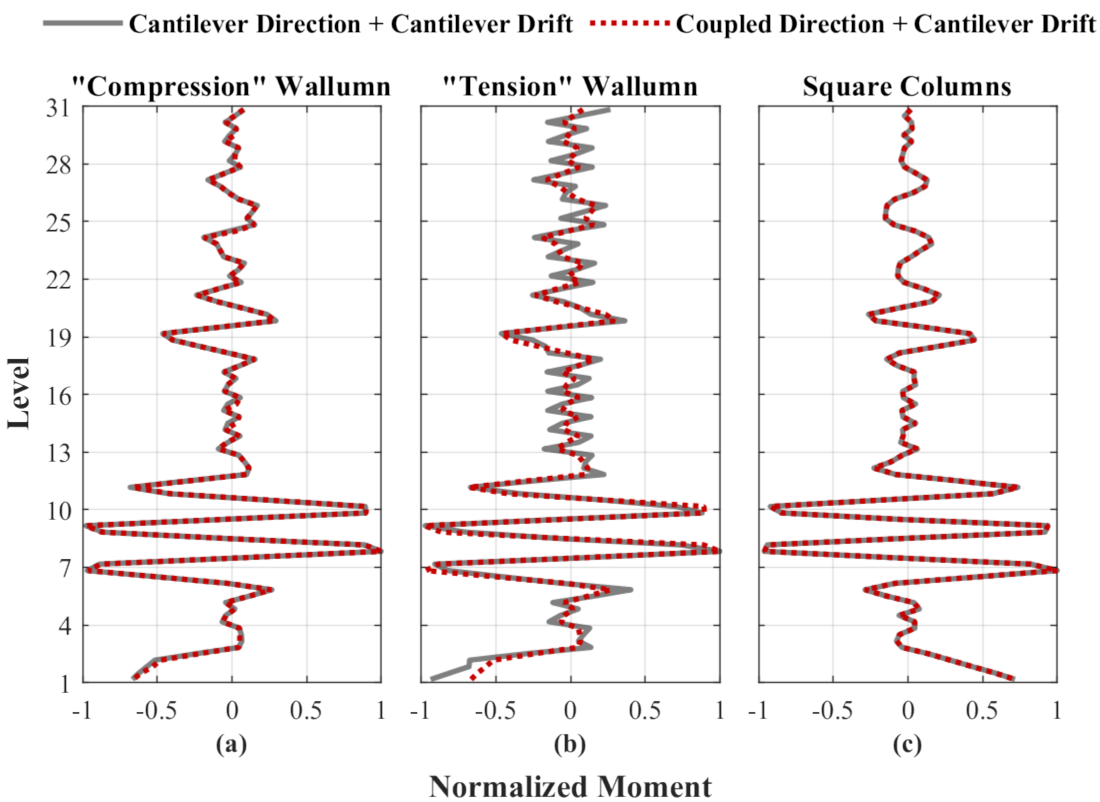

Figure A.1 Moment pattern caused by the cantilever drift profile applied to the cantilever and coupled directions

Figure A.1 demonstrates that the curvature imposed in the columns GFRS is independent on the building direction. The drift profile causes single curvature in the first 2 storeys, between the first and third level. Above this, the storeys experience either single or double curvature. For example, the sixth storey experiences single curvature whereas the thirteenth storey experiences double curvature.

The Simplified Analysis coupled drift profile was also applied to both building's directions to observe if it influences the columns' curvature, see Figure A.2.

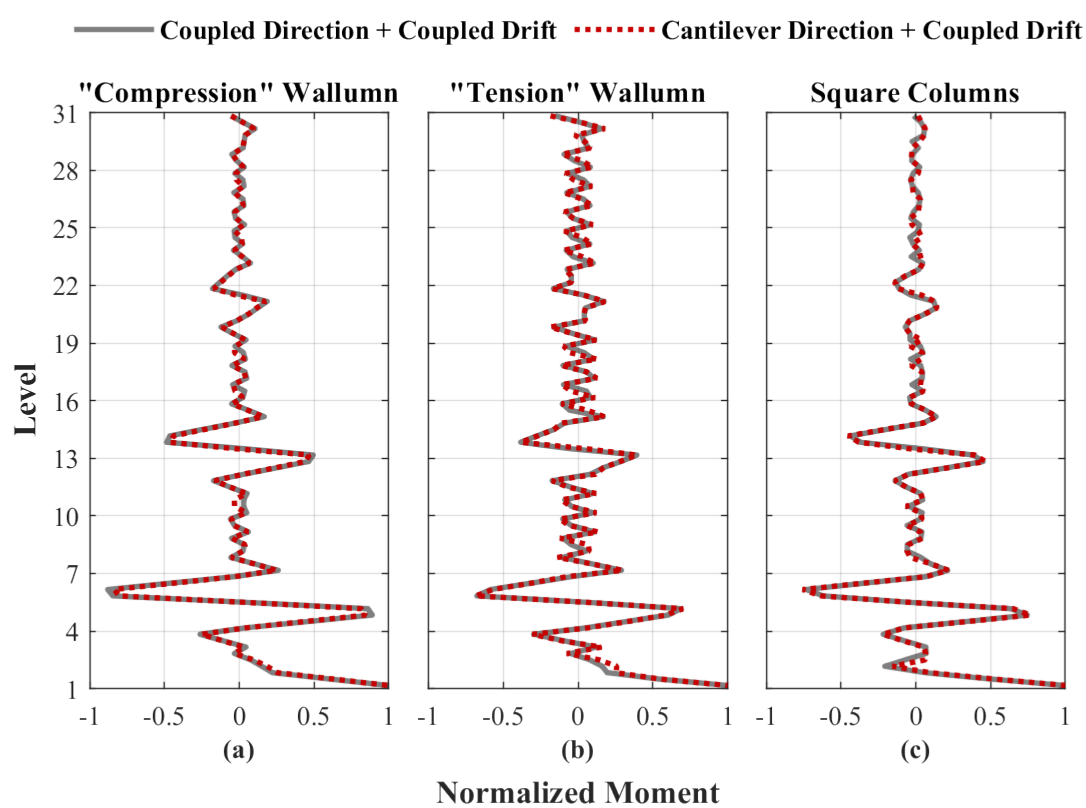

Figure A.2 Moment pattern caused by the coupled drift profile applied to the cantilever and coupled directions

As well as with the Simplified Analysis cantilever profile, Figure A.2 proves that the curvature of the GFRS columns is dependent on the coupled drift profile regardless the building's direction. The coupled drift profile enforces a single curvature in the first two storeys and double curvature at the third. Above this storey, the storey could experience either single or double curvature. It is also fundamental to understand that the single or double curvature observed in the vertical elements depend not only on the drift profile, but also on other factors as discussed in Section 2.6.

Last, it is important to note that each drift profile enforces a specific moment shape pattern throughout the building's height regardless of the column type, axial load, and position within the floorplan. The cantilever drift profile exerts the largest moment demands around a quarter of the building's height, between levels 6 and 12. The coupled drift profile results in having the largest moment demands at grade and in the first third of the building's height.

Appendix B Nonlinear Rotation in GFRS Elements

In this appendix, the maximum observed rotation of GFRS elements during the pushover analysis is reported for *Building Model 1* and *2*. The rotation was computed as $(d/2)\cdot k$, where $d/2$ is the assumed plastic hinge length and k is the curvature.

B.1 *Building Model 1* GFRS Nonlinear Rotations

Cantilever Direction

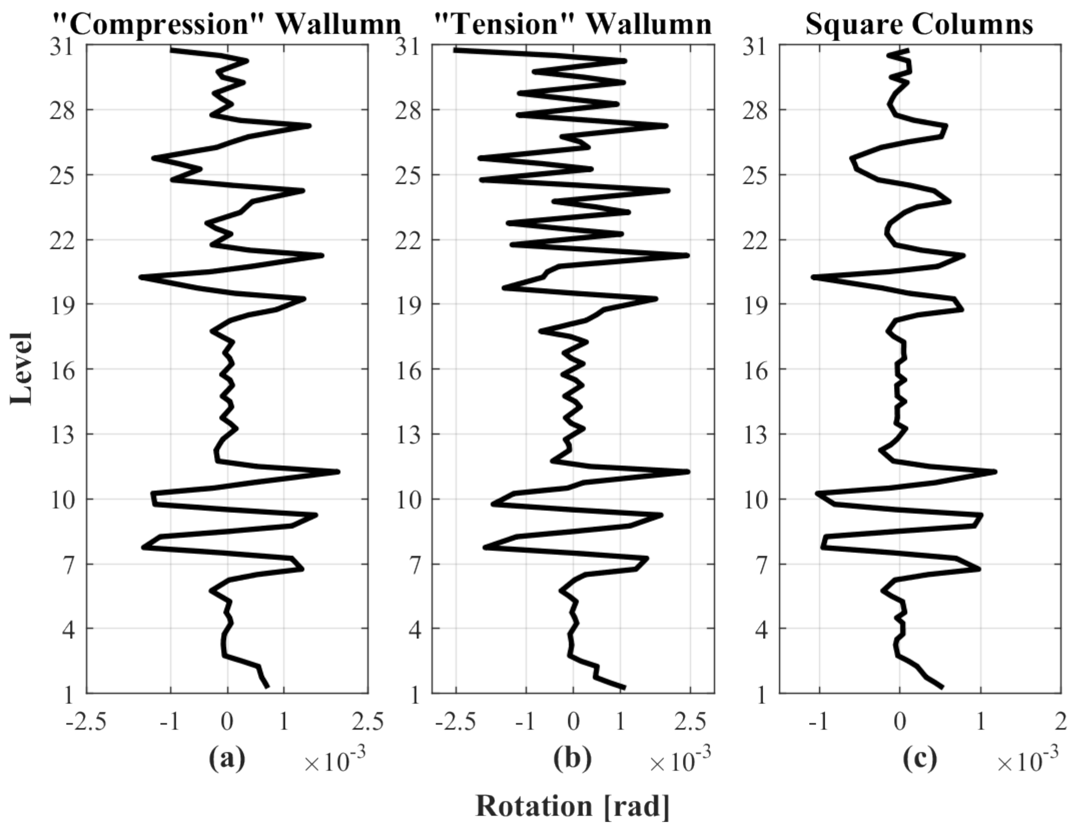

Figure B.1 *Building Model 1* maximum nonlinear rotations for columns in the cantilever direction; (a) compression outrigger wallumn; (b) tension outrigger wallumn; (c) non-outrigger square columns

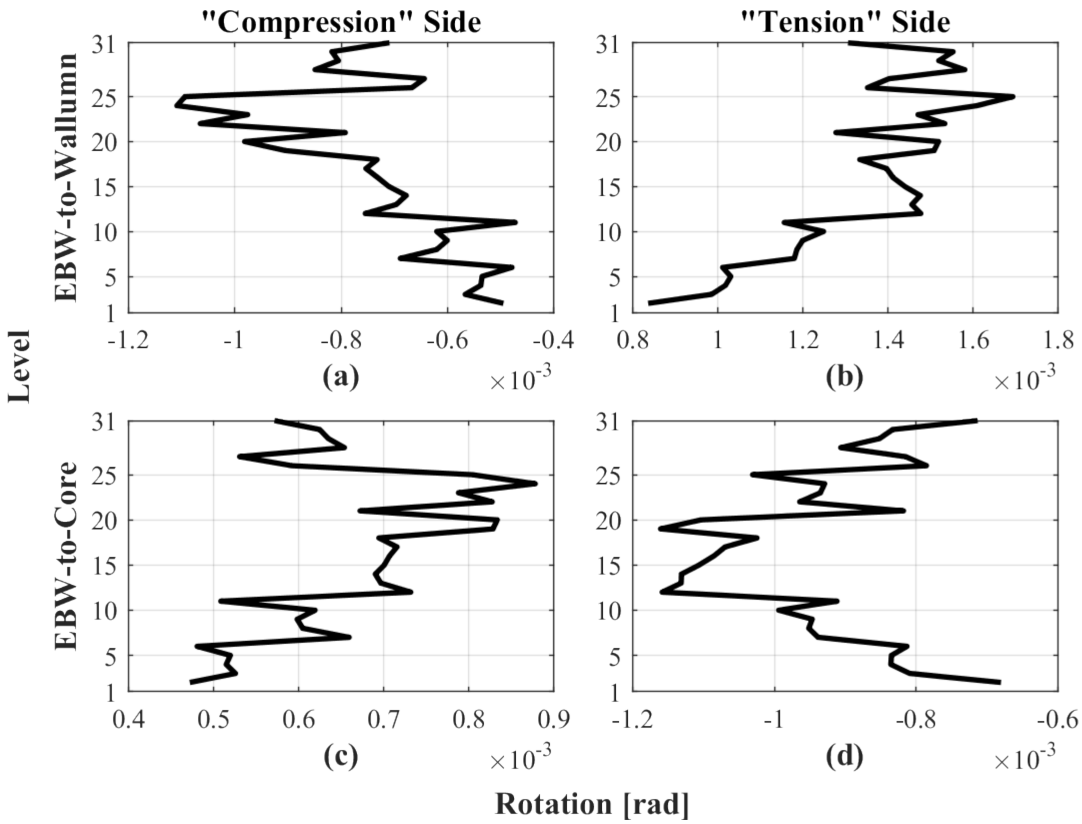

Figure B.2 *Building Model 1* maximum nonlinear rotations for EBW slabs in the cantilever direction; (a) EBW-to-wallumn “compression” side; (b) EBW-to-wallumn “tension” side; (c) EBW-to-core “compression” side; (d) EBW-to-core “tension” side

Coupled Direction

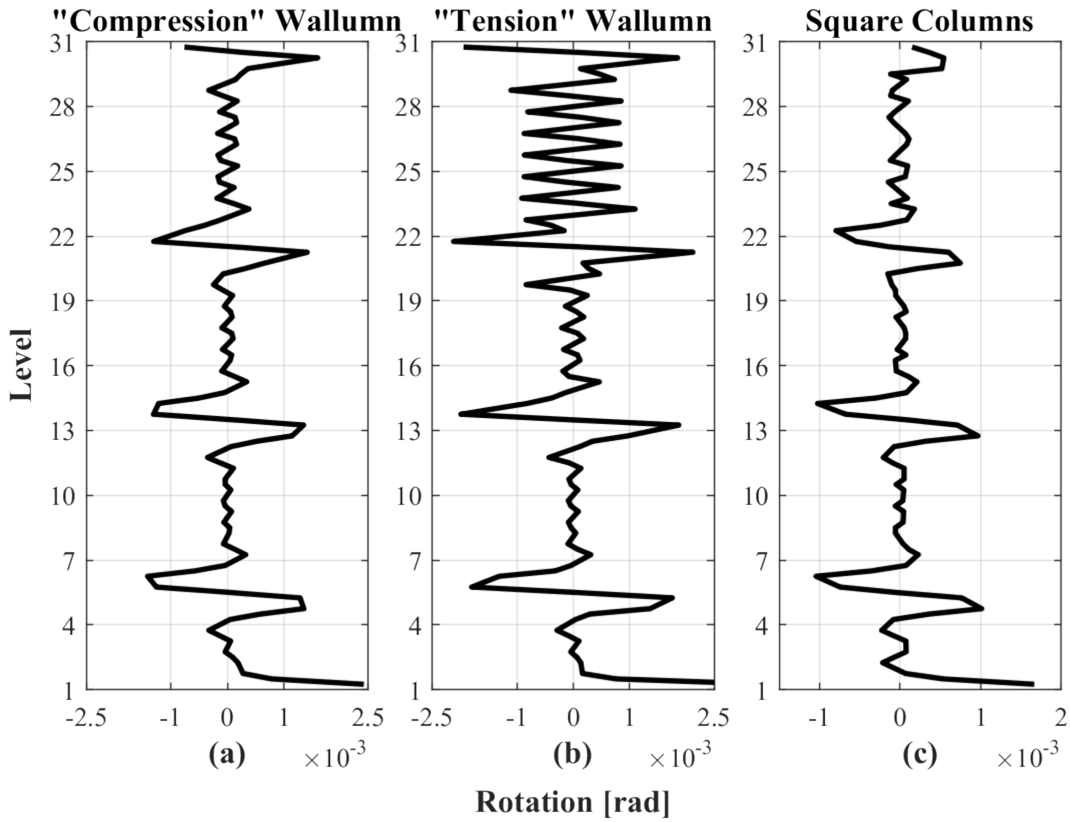

Figure B.3 *Building Model 1* maximum nonlinear rotations for columns in the coupled direction; (a) compression outrigger wallumn; (b) tension outrigger wallumn; (c) non-outrigger square columns

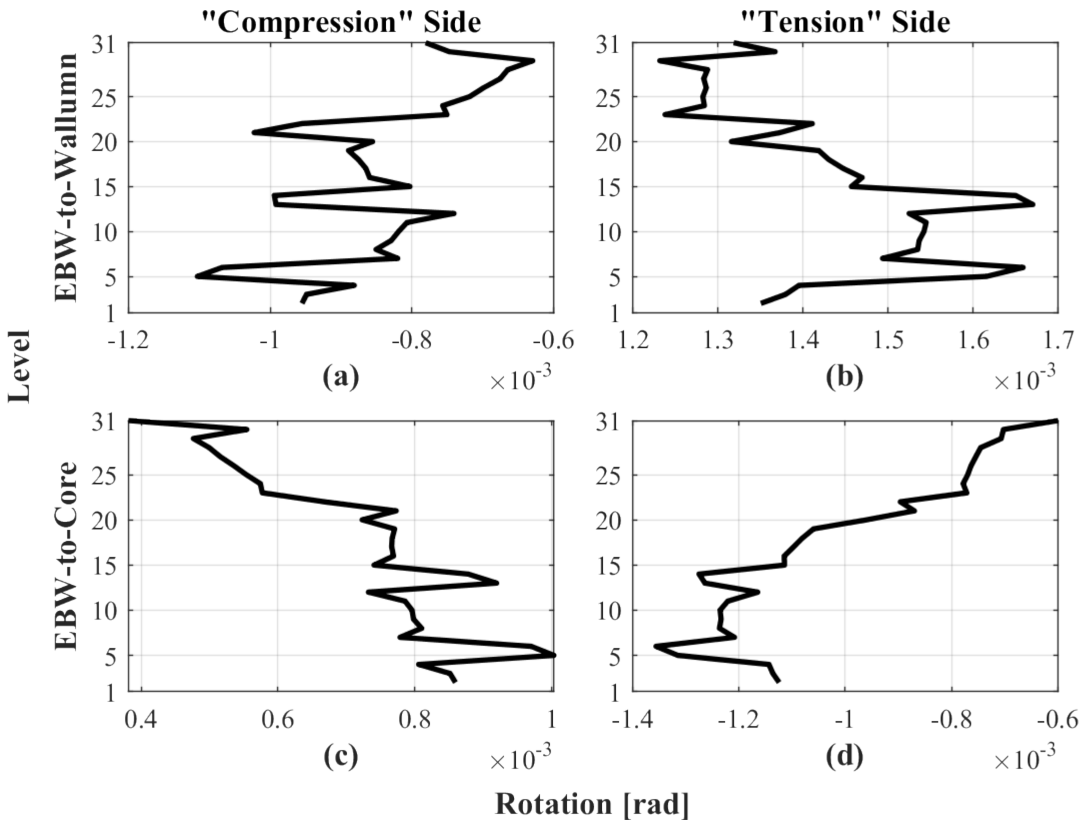

Figure B.4 *Building Model 1* maximum nonlinear rotations for EBW slabs in the coupled direction; (a) EBW-to-wallumn "compression" side; (b) EBW-to-wallumn "tension" side; (c) EBW-to-core "compression" side; (d) EBW-to-core "tension" side

B.2 *Building Model 2* GFRS Nonlinear Rotations

Cantilever Direction

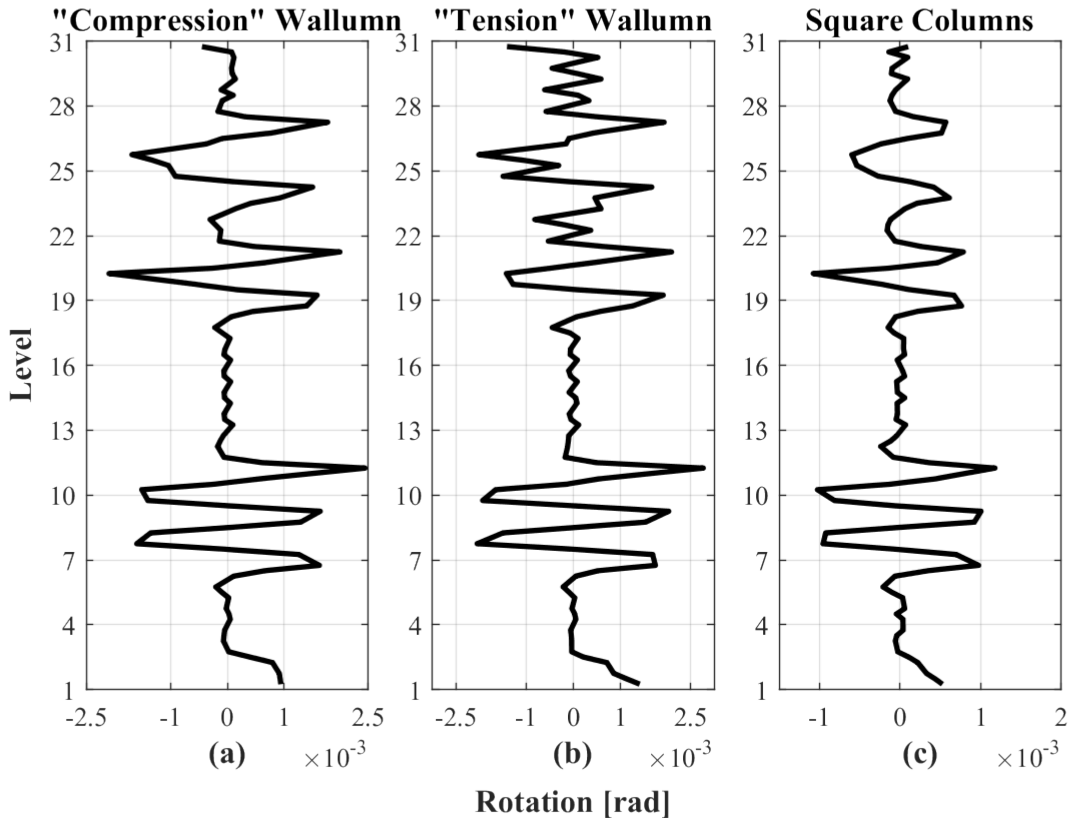

Figure B.5 *Building Model 2* maximum nonlinear rotations for columns in the cantilever direction; (a) compression outrigger wallumn; (b) tension outrigger wallumn; (c) non-outrigger square columns

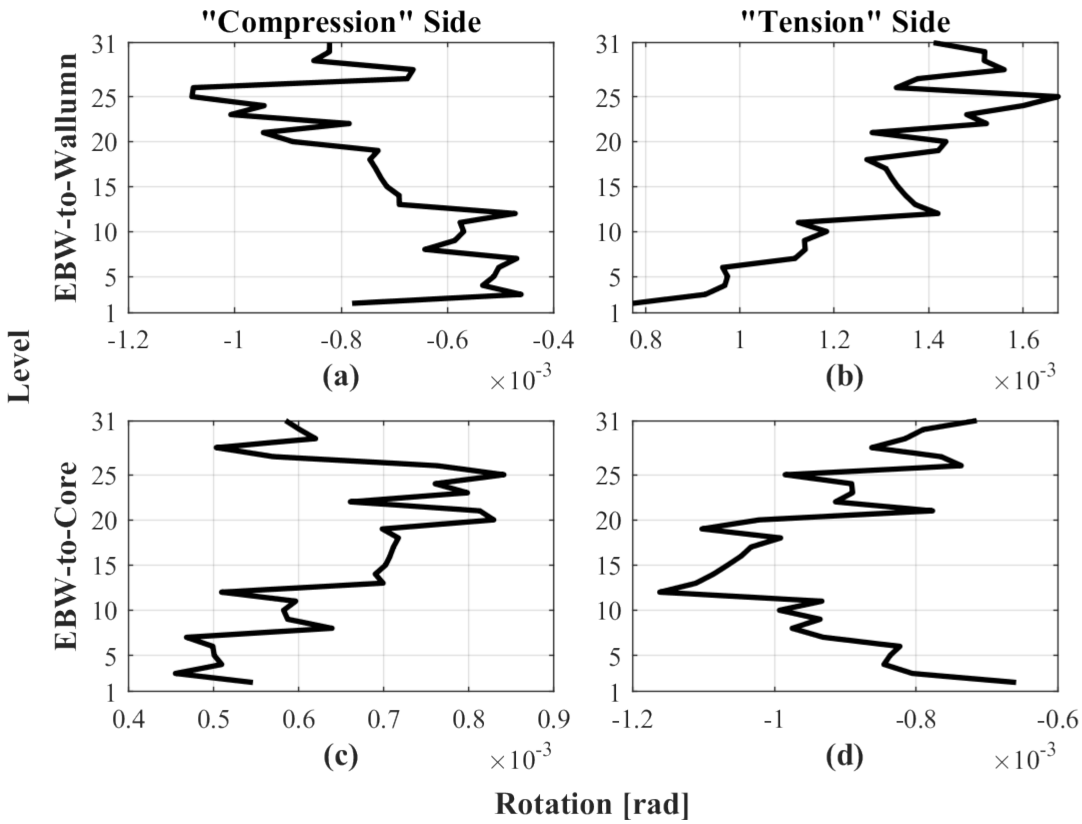

Figure B.6 Building *Model 2* maximum nonlinear rotations for EBW slabs in the cantilever direction; (a) EBW-to-wallumn “compression” side; (b) EBW-to-wallumn “tension” side; (c) EBW-to-core “compression” side; (d) EBW-to-core “tension” side

Coupled Direction

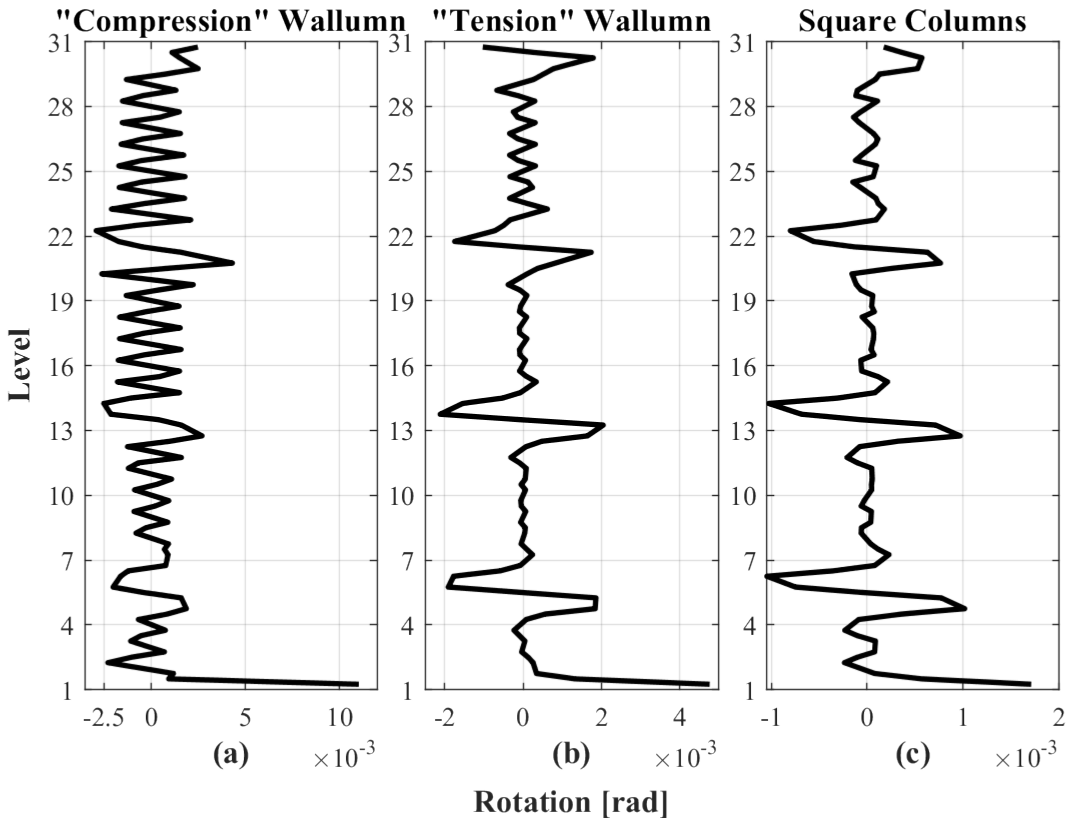

Figure B.7 B*uilding Model 2* maximum nonlinear rotations for columns in the coupled direction; (a) compression outrigger wallumn; (b) tension outrigger wallumn; (c) non-outrigger square columns

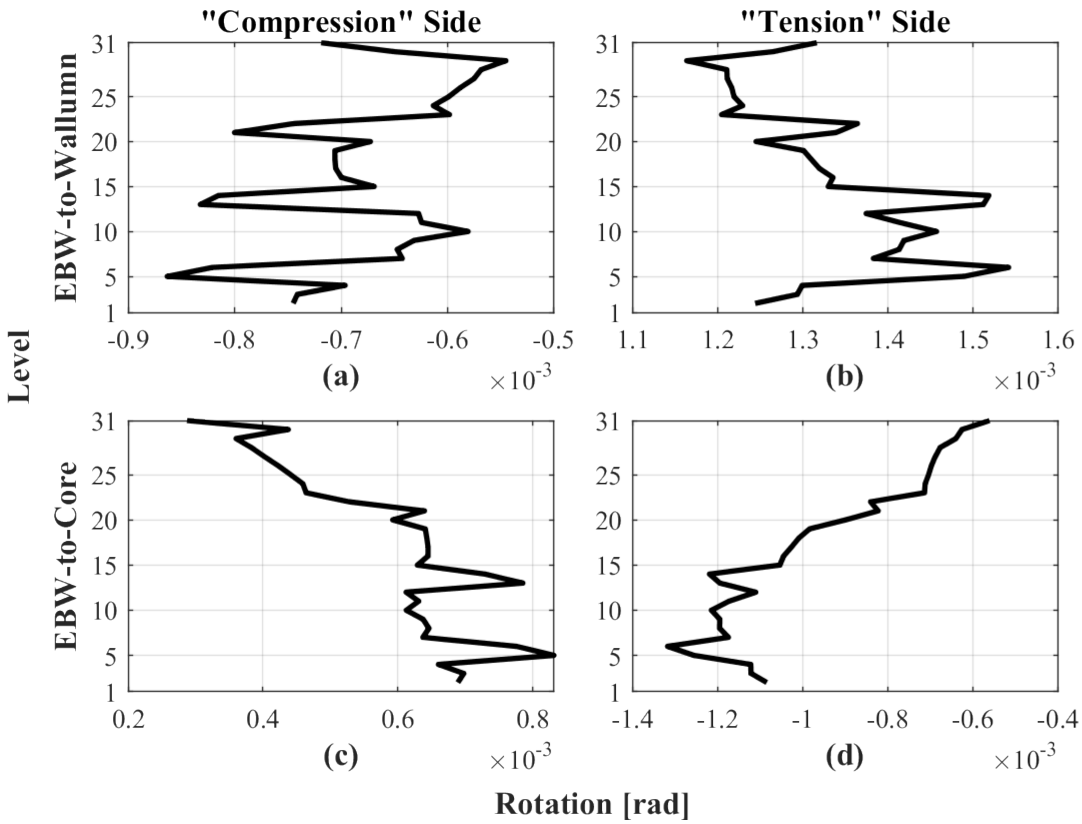

Figure B.8 *Building Model 2* maximum nonlinear rotations for EBW slabs in the coupled direction; (a) EBW-to-wallumn "compression" side; (b) EBW-to-wallumn "tension" side; (c) EBW-to-core "compression" side; (d) EBW-to-core "tension" side

Appendix C Flexural Stiffness Modifiers Computed for *Building Model 1* and *2*

In this appendix, the flexural stiffness modifiers of the GFRS components computed using the *Proposed Equations* are presented for *Building Model 1* and *2*.

Building Model 1

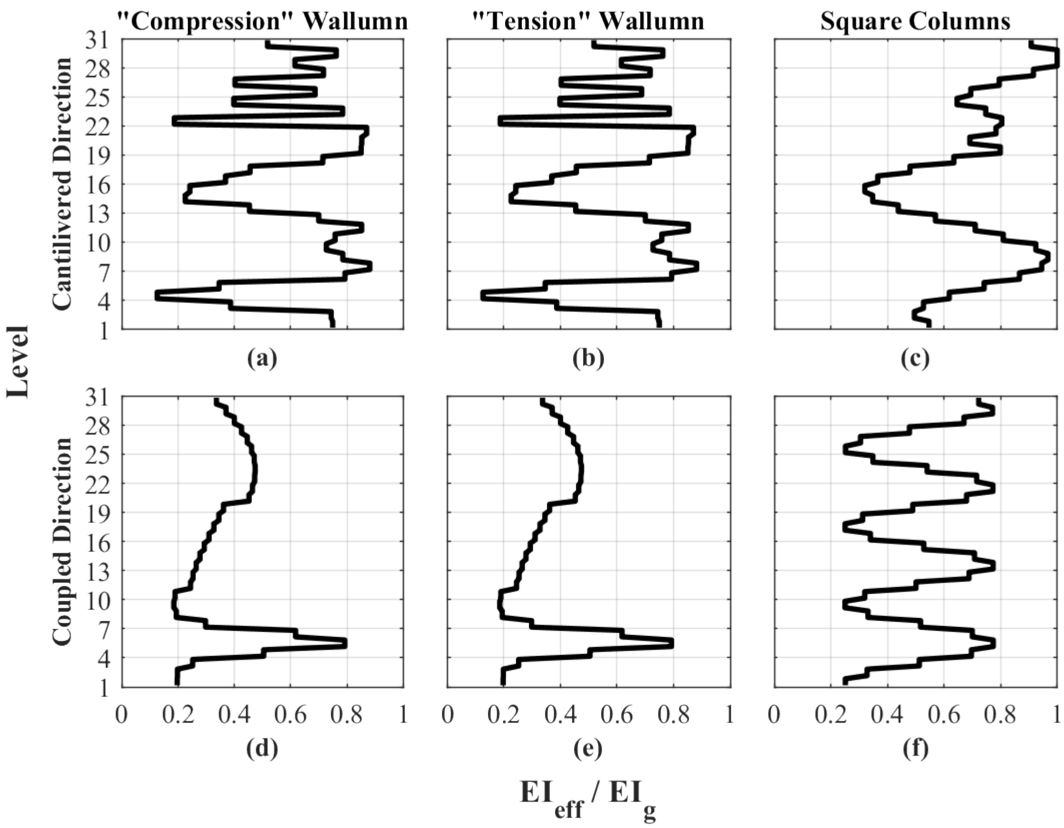

Figure C.1 *Building Model 1* flexural stiffness modifiers for columns in the cantilevered direction, plots (a) to (c) and coupled direction, plots (d) to (f).

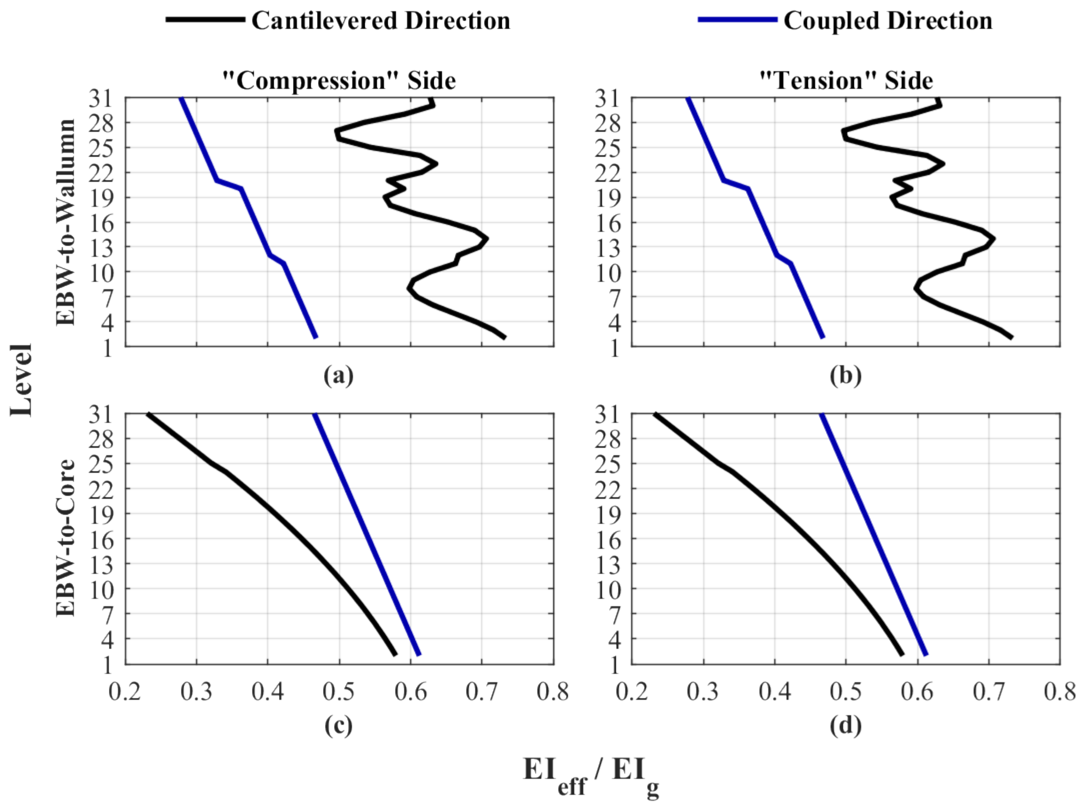

Figure C.2 *Building Model 1* flexural stiffness modifiers for EBW slabs in the cantilevered direction and coupled direction; (a) EBW-to-wallumn "compression" side; (b) EBW-to-wallumn "tension" side; (c) EBW-to-core "compression" side; (d) EBW-to-core "tension" side.

Building Model 2

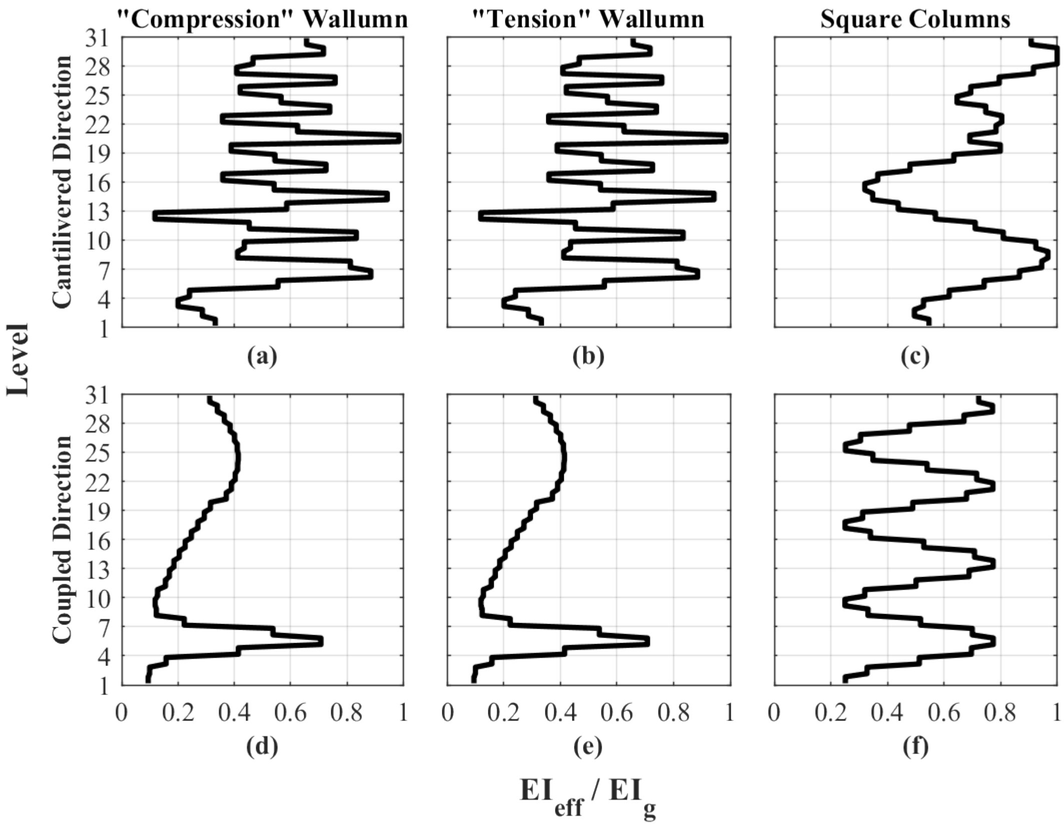

Figure C.3 *Building Model 2* flexural stiffness modifiers for columns in the cantilevered direction, plots (a) to (c) and coupled direction, plots (d) to (f).

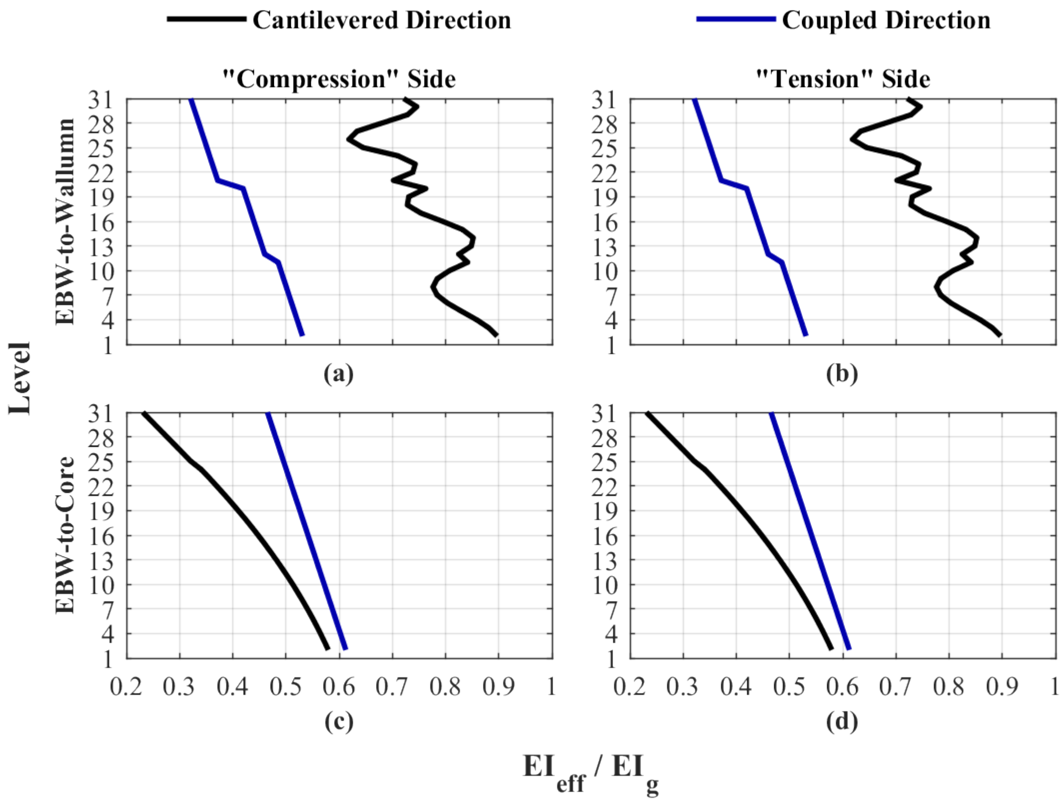

Figure C.4 *Building Model 2* flexural stiffness modifiers for EBW slabs in the cantilevered direction and coupled direction; (a) EBW-to-wallumn "compression" side; (b) EBW-to-wallumn "tension" side; (c) EBW-to-core "compression" side; (d) EBW-to-core "tension" side.